TAMPEREEN TEKNILLINEN YLIOPISTO
TAMPERE UNIVERSITY OF TECHNOLOGY

NIKO NIEMELÄ
COMPUTATIONAL FLUID DYNAMICS MODELING OF PULVERIZED BIOMASS COMBUSTION USING OPTIMIZED REACTIVITY PARAMETERS

Master of Science Thesis

ABSTRACT

In this work, optimized apparent reactivity parameters are used for combustion modeling of two biomass fuels. The main goal is to examine how the existing solid fuel models in the commercial Computational Fluid Dynamics (CFD) software ANSYS Fluent function for pulverized biomass, as they have been originally developed for coal simulations. The models assume that the particles are spherical and isothermal, and the devolatilization and char combustion stages happen consecutively.

A CFD model of the Drop-Tube Reactor (DTR) test device, that was used for the reactivity studies of the fuels, is constructed. The functioning of the optimized reactivity parameters is verified by the model. The results show that the apparent reactivity parameters can describe the biomass mass loss in low oxygen levels, regardless of the model assumptions. However, in an oxygen level of 21 vol-% the assumption of consecutive combustion stages does not hold. The simulations demonstrate how CFD modeling can provide useful information required for accurate biomass reactivity parameters.

The verified reactivity parameters are further tested in a CFD model of 50 kW pulverized fuel test reactor. The model is validated by comparing lignite combustion results with previously conducted measurements. After this, a biomass simulation is conducted using the optimized reactivity parameters. The biomass simulation captures multiple realistic phenomena, such as lower burnout efficiency compared to lignite. The results further indicate that the spherical and isothermal assumptions can describe the biomass mass loss in combustion modeling, if the apparent reactivity parameters are carefully optimized based on experimental and CFD simulation data.

TIIVISTELMÄ

Tässä työssä mallinnetaan kahden biomassan palamisprosessia optimoitujen reaktiivisuusparametrien avulla. Tavoitteena on selvittää kuinka olemassa olevat kiinteiden polttoaineiden mallit kaupallisessa virtauslaskentaohjelmistossa ANSYS Fluentissa toimivat biomassan pölypolton mallinnuksessa, sillä mallit on alunperin kehitetty hiilelle. Malleissa oletetaan partikkelien olevan pallomaisia ja isotermisiä, sekä pyrolyysin ja koksin palamisen tapahtuvan peräkkäisinä vaiheina.

Polttoaineiden reaktiivisuustutkimuksiin käytetystä pudotusputkireaktorista tehdään numeerinen virtauslaskentamalli (CFD-malli) ja aikaisemmin määritettyjen reaktiivisuusparametrien toiminta varmistetaan mallin avulla. Tulokset osoittavat, että biomassapartikkelien palaminen voidaan kuvata globaaleilla reaktiivisuusparametreilla alhaisissa happitasoissa, huolimatta tehdyistä oletuksista. Oletus peräkkäisistä palamisvaiheista ei kuitenkaan toimi 21 tilavuusprosentin happitasossa. Reaktorin mallinnus osoittaa, että CFD-laskenta voi tarjota hyödyllistä tietoa tarkkojen reaktiivisuusparametrien määritystä varten.

Reaktiivisuusparametrien toimivuutta tutkitaan 50 kW:n pölypolttoreaktorin CFD-mallinnuksen avulla. Mallin toimivuus varmistetaan vertaamalla ruskohiilelle tehdyn simulaation tuloksia kokeellisiin mittauksiin. Tämän jälkeen mallia käytetään biomassan palamisen simulointiin optimoituja reaktiivisuusparametreja hyödyntäen. Biomassasimulaation tulokset onnistuvat esittämään oikein useita järkeviä ilmiöitä, kuten matalamman palamishyötysuhteen ruskohiileen verrattuna. Diplomityön tulosten valossa biomassapartikkelit voidaan olettaa pallomaisiksi ja isotermisiksi, jos globaalit reaktiivisuusparametrit on määritetty tarkasti mittaus- ja mallinnusdataan perustuen.

PREFACE

This thesis was carried out at Tampere University of Technology (TUT) in the Department of Chemistry and Bioengineering. The work was part of the Sustainable Bioenergy Solutions for Tomorrow (BEST) research program coordinated by CLIC Innovation, with funding from the Finnish Funding Agency for Innovation, Tekes. The industrial partner, Valmet Technologies Oy, provided guidance, financial support, and the biomass fuels for this study. A three month research exchange was carried out at Technical University of Dresden (TUD) in the Chair for Combustion, Heat and Mass Transfer. The support of all collaboration partners is gratefully acknowledged.

I would like to express my gratitude to my supervisor, Prof. Antti Oksanen, for providing me the possibility to work on this thesis project. I have had a chance to work independently and to learn valuable skills for the future career. The second supervisor, D.Sc. Aino Leppänen, has provided invaluable help during the thesis project. I want to thank her for all the important comments regarding the thesis and all the effort she has made for me. I want to express my gratitude to Teemu Saarinen, Henrik Tolvanen and all other colleagues at the Power Plant and Combustion Technology research group at Tampere University of Technology.

The meetings at Valmet Technologies Oy have been an important part of this thesis project. I want to express my gratitude to Tero Joronen, Matti Ylitalo, Asko Rantee, Jouni Valtatie, Jukka Mäkinen, Matti Rautanen and all other persons who have taken part in the meetings.

A grateful acknowledgment belongs to Prof. Michael Beckmann and D.Sc. Sebastian Grahl at Dresden University of Technology for providing me the opportunity to work at their chair and to model the research reactor at their university. The research exchange was an invaluable part of the project. Furthermore, I want to thank all the colleagues at TUD who made my stay unforgettable.

The support of all the people at the Guild of Environmental and Energy Technology (YKI), and of my friends Laura Salo, Sampsa Martikainen and Niko Tissari cannot be sufficiently emphasized. Thank you for all the moments we have experienced together during the studies. Finally, the love and support of my parents, sisters and brothers and all family members receives the greatest expression of gratitude.

Tampere, March 21, 2016

Niko Niemelä

TABLE OF CONTENTS

LIST OF FIGURES

LIST OF TABLES

LIST OF ABBREVIATIONS AND SYMBOLS

B1a, B1b, B1c	Biomass fuel 1 size group a/b/c
B2a, B2b, B2c	Biomass fuel 2 size group a/b/c
BFB	Bubbling Fluidized Bed
CFB	Circulating Fluidized Bed
CFD	Computational Fluid Dynamics
COMET	Coupled Ordinates Method
daf	Dry Ash-Free
DNS	Direct Numerical Simulation
DO	Discrete Ordinates model
DRW	Discrete Random Walk model
DTRM	Discrete Transfer Radiation Model
DTR	Drop-Tube Reactor
EDC	Eddy Dissipation Concept
EDM	Eddy Dissipation Model
FBC	Fluidized Bed Combustion
FC	Fixed Carbon
FDM	Finite Difference Method
FEM	Finite Element Method
FVM	Finite Volume Method
HHV	Higher Heating Value
LES	Large Eddy Simulation
MSW	Municipal Solid Waste
PDF	Probability Density Function
PFC	Pulverized Fuel Combustion
RANS	Reynolds-Averaged Navier-Stokes equations
RSM	Reynolds-Stress Model
RTE	Radiative Transfer Equation
URANS	Unsteady Reynolds-Averaged Navier-Stokes equations
VM	Volatile Matter
WSGGM	Weighted Sum of Grey Gases Method
Φ	Scattering phase function [1/sr]
α	Temperature exponent in Arrhenius law [*various*]

α_p	Volume fraction of particles in a fluid [-]
β	Extinction coefficient [1/m]
δ_{ij}	Kronecker delta [-]
ε	Turbulent kinetic energy dissipation rate [J/(kg s)]
ε_p	Particle emissivity [-]
κ	Absorption coefficient [1/m]
μ	Dynamic viscosity of a fluid [kg/(m s)]
μ_t	Turbulent viscosity [kg/(m s)]
ρ	Density [kg/m^3]
ρ_p	Particle density [kg/m^3]
σ	Stefan-Boltzmann constant (5.67) [W/(m^2 K^4)]
σ_s	Scattering coefficient [$1/m$]
τ_{ij}	Viscous stress tensor of a fluid [kg/(m s^2)]
$\dot{\omega}_k$	Reaction rate of species k [kg/(m^3 s)]

A	Surface area [m^2]
A_p	Surface area of a particle [m^2]
A_{sph}	Surface area of a sphere-equivalent particle [m^2]
AR	Aspect ratio of a cylinder [-]
Bi	Biot number [-]
C_1	Model constant in Kinetics/Diffusion-Limited Rate model [-]
C_2	Model constant in Kinetics/Diffusion-Limited Rate model [-]
C_D	Drag coefficient [-]
D_0	Diffusion rate coefficient in Kinetics/Diffusion-Limited Rate model [-]
$D_{i,m}$	Bulk diffusion coefficient [m^2/s]
E_a	Activation energy [J/mol]
G	Incident radiation [W/m^2]
H_{reac}	Heat release from char burnout reaction [J/kg]
I	Radiant intensity [W/(m^2 sr)]
I_b	Black body intensity [W/(m^2 sr)]
Nu	Nusselt number [-]
Pr	Prandtl number [-]
$\dot{Q}$	Heat source term in energy equation [J/m^3]
$\mathfrak{R}_1$	Low temperature reaction rate in Kobayashi devolatilization model [1/s]
$\mathfrak{R}_2$	High temperature reaction rate in Kobayashi devolatilization model [1/s]
R_u	Universal gas constant (8.314) [J/(mol K)]

Re	Reynolds number [-]
Re_{sph}	Sphere-equivalent particle Reynolds number [-]
S_b	Stoichiometric mass of oxidant per mass of char [-]
Sc_{kt}	Turbulent Schmidt number of species k [-]
SF	Shape factor [-]
SF_c	Shape factor of a cylinder [-]
T	Temperature [K]
T_{bp}	Boiling point temperature for Discrete Phase Model [K]
T_{dev}	Devolatilization temperature for Discrete Phase Model [K]
T_p	Temperature of a particle [K]
T_{vap}	Vaporization temperature for Discrete Phase Model [K]
T_∞	Fluid temperature in particle surroundings [K]
$V_{k,i}$	Diffusion velocity of species k in i-direction [m/s]
Y_k	Mass fraction of species k [-]
c_p	Specific heat capacity [J/(kg K)]
d_c	Characteristic particle diameter [m]
d_c	Diameter of a cylinder [m]
$d_{p,0}$	Initial diameter of a particle [m]
d_p	Particle diameter [m]
d_{sph}	Sphere-equivalent particle diameter [m]
e_t	Total specific energy [J/kg]
f	Time-dependent variable f [*various*]
$\overline{f}$	Time-averaged value of variable f [*various*]
f'	Fluctuating component of variable f in Reynolds-averaging [*various*]
$\tilde{f}$	Favre-averaged value of variable f (mass-weighted average) [*various*]
f''	Fluctuating component of variable f in Favre-averaging [*various*]
f_{comb}	Initial mass fraction of char in a particle [-]
f_h	Fraction of char burnout heat release a particle absorbs [-]
$f_{k,j}$	Volume force acting on species k in i-direction [N/m^3]
$f_{v,0}$	Initial mass fraction of volatiles in a particle [-]
$f_{w,0}$	Initial mass fraction of water in a particle [-]
h	Convective heat transfer coefficient [W/(m^2 K)]
h_{fg}	Latent heat [J/kg]
h_s	Specific sensible enthalpy [J/kg]
h_t	Total specific enthalpy [J/kg]

k	Turbulent kinetic energy [J/kg]
k	Thermal conductivity [W/(m K)]
k_c	Mass-transfer coefficient [m/s]
$m_{p,0}$	Initial mass of a particle [kg]
m_p	Particle mass [kg]
p	Pressure [Pa]
p_{ox}	Partial pressure of oxygen in particle surroundings [Pa]
q_i	Energy flux in energy equation [J/m^2]
$\vec{r}$	Position vector [m]
$\vec{s}$	Direction vector [m]
t	Time [s]
$\vec{u}$	Gas phase velocity vector [m/s]
u_i	Velocity component in i-direction [m/s]
$\vec{u_p}$	Particle velocity vector [m/s]
x_i	Coordinate axis in i-direction [m]
$\vec{x_p}$	Particle position vector [m]

1. INTRODUCTION

1.1 Motivation

The main motivation for biomass combustion is its carbon neutrality and renewability. Biomass combustion releases carbon dioxide emissions, but as a new plant grows, it absorbs the carbon dioxide back from the atmosphere. In contrast, the carbon dioxide the fossil fuels have absorbed millions of years ago is irreversibly released into the atmosphere in combustion. For this reason, biomass fuels are considered carbon neutral. The harvesting, transporting and processing of biomass fuels causes indirect emissions, but if a life cycle analysis comparing the CO_2 emissions of biomass and fossil fuels is considered, biomass is a clear winner [1]. In addition to carbon neutrality, the renewability of biomass makes its use appealing.

When biomass is considered for energy production, the most important factor is to ensure its sustainability. A substantial rise in biomass usage can lead to decreasing farmland and forest biodiversity and increasing use of soil and water resources. However, significant amounts of biomass can technically be available to support ambitious renewable energy targets, even if strict environmental constraints are applied [2]. According to Report No 7/2006 of European Environment Agency [2], the environmentally-compatible primary biomass potential in Europe is around 295 MtOE (tonnes of oil equivalent) in 2030, which represents 15-16% of the projected energy consumption of the EU-25 in 2030. Furthermore, biomass plays an important role in the future energy scenarios aiming to keep global mean temperature rise below 2°C, such as the RCP2.6 scenario presented in reference [3].

In addition to previous factors, combustion technologies will play an important role in the reliability of the future energy systems. As the wind and solar power increases, combustion technologies will become ever more important as back-up power, when no wind or sun is available. For this purpose, biomass fuels will become increasingly valuable if the use of fossil fuels is to be decreased.

1.2 Scope of the Thesis

This thesis is part of a larger study, which aims to determine the reactivity and fuel handling properties of two biomass fuels (biomass fuel 1 and biomass fuel 2), and to produce reactivity parameters for Computational Fluid Dynamics (CFD) models that can be used for pulverized biomass combustion modeling. The study was conducted using both experimental and numerical methods. The experimental tests were used for evaluating the reactivity and combustion properties of the fuels, and the results were then used in numerical reactivity parameter optimization. The produced reactivity parameters were used in CFD modeling of the two biomass fuels, in order to evaluate the capabilities of the existing combustion models for pulverized biomass modeling. Thus, the whole study consisted of two main parts:

1. Experimental tests with a Drop-Tube Reactor (DTR) and numerical reactivity parameter optimization with MATLAB [4],
2. Reactivity parameter verification with a CFD model of the DTR, and parameter testing in a larger scale pulverized fuel test reactor of 50 kW$_{th}$.

The first part of the study was conducted by B.Sc. Teemu Saarinen during his Master of Science thesis work [5]. The second part represents the work of this thesis. Fig. 1.1 demonstrates the connection between the two theses.
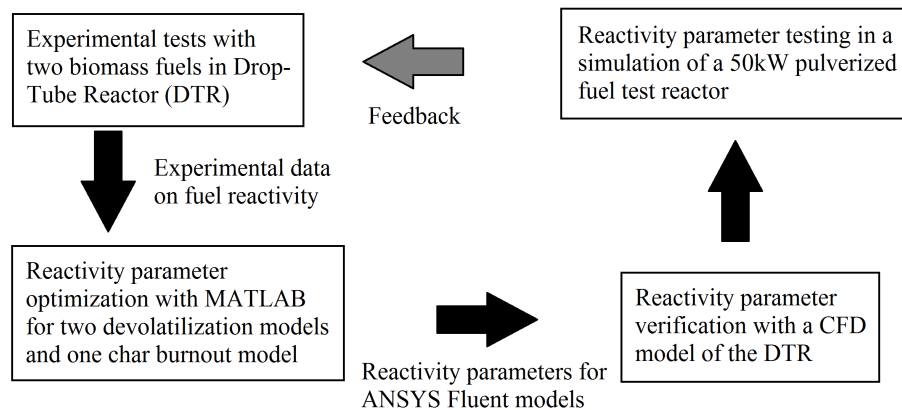
Figure 1.1 *A schematic figure of the procedure for determining the biomass reactivity parameters. The left part of the figure represents the M.Sc. thesis work of Teemu Saarinen [5], and the right part the present work.*

In the work of Teemu Saarinen (the left part of Fig. 1.1), the devolatilization and char combustion reactivities of the two biomass fuels were determined experimentally with the DTR, located at the Tampere University of Technology (TUT). The experimental data

was used for optimizing the apparent devolatilization and char combustion model reactivity parameters with the optimization tools in MATLAB R2015a [4]. The devolatilization stage of the particle combustion was modeled with two different submodels: the Single Kinetic Rate Model and the Two Competing Rates (Kobayashi) Model. The char combustion stage was modeled with the Kinetics/Diffusion-Limited Rate Model. All three models are default models available in the commercial CFD software ANSYS Fluent [6], which was used in the CFD modeling work of this thesis.

The first goal of this thesis was to construct a CFD model of the DTR test facility and to model the combustion process of the two biomass fuels inside the reactor. The DTR modeling was conducted for three main purposes:

1. Obtaining information on the flow and temperature fields, and particle motion inside the DTR
2. Giving feedback for the reactivity parameter optimization procedure
3. Verifying the MATLAB-based fuel reactivity parameters determined by Teemu Saarinen in his M.Sc. thesis [5].

The second goal of this thesis was to use the optimized reactivity parameters in a larger scale application. For this purpose, a CFD model of a 50kW_{th} pulverized fuel test facility, located at the Dresden University of Technology, was constructed. The model of the test reactor was used for testing the devolatilization and char combustion models and the reactivity parameters optimized for them. Finally, the information obtained from the CFD simulations was used for analyzing the capabilities of the available models for pulverized biomass combustion, and future recommendations for the model development were made.

The thesis consists of eight chapters. After this introduction chapter, two theory chapters follow. In Chapter 2, the theoretical background of solid biomass combustion is presented. The chapter presents the definition of a biomass fuel in Section 2.1 and introduces the main physical and chemical combustion properties of biomass in Section 2.2. The chapter continues with Section 2.3, which presents the main combustion stages of a solid fuel particle: the drying, devolatilization and char burnout. Finally, the chapter ends with Section 2.4, which introduces the main technologies for biomass combustion.

The second theory chapter of the thesis, Chapter 3, concentrates on theory of Computational Fluid Dynamics (CFD), and in particular to the theory of numerical combustion modeling. The different sections present the main equations and submodels that are needed for a complete combustion simulation.

After the theory part, Chapter 4 presents the experimental methods used in the biomass reactivity studies. The chapter presents the experimental test facilities in Section 4.1, introduces the measurements that were conducted for the two biomass fuels in Section 4.2, and describes the experimental test arrangements in Section 4.3.

The following chapter, Chapter 5, describes how the two biomass fuels were treated in the numerical modeling and how the reactivity parameters were optimized for the devolatilization and char burnout models. Thus, Chapters 4 and 5 form a description of the work that was done by Teemu Saarinen in his M.Sc. thesis work.

The next two chapters, Chapters 6 and 7, present the main work of this thesis. Chapter 6 introduces the CFD model of the DTR and presents the results for the two biomass fuels, that were obtained with the optimized reactivity parameters.

Chapter 7 presents the CFD model of the 50kW_{th} reactor and the simulation results that were obtained for lignite and biomass fuel 1 combustion. The lignite simulation was used for validating the CFD model and biomass fuel 1 combustion was then simulated in order to test the optimized reactivity parameters. Finally, Chapter 8 presents the main conclusions that were drawn during the work.

2. THEORETICAL BACKGROUND OF BIOMASS COMBUSTION

Biomass fuels (or biofuels) are widely used and manufactured in many industries such as in energy, transportation and chemical industries. Biofuels include gaseous, liquid and solid fuels, which can be produced by many different technologies including gasification for gaseous fuels, pyrolysis for liquid fuels and torrefaction for solid fuels. On the other hand, if the biomass quality is sufficient, it can also be directly utilized to produce electricity and heat by combustion.

This thesis focuses on the viewpoint of the energy industry, namely on the combustion of solid biofuels in heat and electricity generation. Solid biofuels can be combusted in many types of boilers, such as in grate furnaces, fluidized bed boilers, or pulverized fuel (PF) boilers. Different combustion techniques are suitable for different ranges of fuel power and the focus will be on the large industrial scale (>5 MW) boilers, which are used in industrial heat and electricity generation. These include mainly the fluidized bed boilers and the pulverized fuel boilers, which can effectively burn many types of biofuels.

The term biomass includes a variety of different organic materials. For this reason, an exact definition of a solid biofuel is introduced. This is done in Section 2.1, where the main sources of solid biomass are identified and the most commonly traded biofuels are introduced. The chemical and physical combustion properties of these fuels are then introduced in Section 2.2. Finally in Section 2.4, the main technologies for biomass combustion are reviewed.

2.1 Definition of a Biomass Fuel

Any organic material derived from plants or animals can be referred as biomass. Plant based biomass is formed through photosynthesis, and the chemical energy stored in the plants is then consumed by humans and animals. Animal and human wastes are usually

included in the definition of biomass. The renewable energy sources (RES) directive 2009/28/EC of the European Parliament gives the following definition for biomass [7]:

"Biomass means the biodegradable fraction of products, waste and residues from biological origin from agriculture (including vegetal and animal substances), forestry and related industries including fisheries and aquaculture, as well as the biodegradable fraction of industrial and municipal waste."

As can be seen from the definition above, biomass contains a variety of different organic materials. Naturally, a wide range of solid, gaseous and liquid biofuels can be produced from biomass.

Different biomass materials can be categorized in many ways, for example by their origin or by the biochemical structure. Biofuels produced from different biomass sources have different fuel properties and for this reason many European and international standards are currently under development. The international (ISO) standards for solid biofuels will be presented here, as they provide a clear classification for solid biofuels.

The international standard series, ISO 17225 [8], define the fuel quality classes and specifications for solid biofuels produced from raw and processed materials. Raw and processed materials include woody, herbaceous (annual plants), fruit and aquatic biomass, and biodegradable waste. Chemically treated biomass, such as wood including paint or glue, has its own special requirements. More details of what is included in the subgroups such as woody or herbaceous biomass, can be found in the ISO 17225 series. The European EN 14961 standard series provides similar definitions.

The aim of the ISO 17225 series is to provide unambiguous and clear classification principles for solid biofuels. The series concern the solid biomass materials originating from the following sectors:

1. Forestry and Arboriculture
2. Agriculture and Horticulture
3. Aquaculture.

These sectors can be identified as the main sources for solid biofuels.

Furthermore, the ISO 17225 series recognize the following main traded forms of solid biofuels:

1. Graded wood pellets
2. Graded wood briquettes
3. Graded wood chips
4. Graded firewood
5. Graded non-woody pellets
6. Graded non-woody briquettes
7. Graded thermally treated and densified biomass fuels.

In the product standards of ISO 17225, *graded* means that the solid biofuel is used either in commercial or industrial applications, which require that the fuels have a specified quality. The fuel quality is a vital factor in industrial energy production and for this reason the biofuel power plants are often utilizing some of these traded forms of biofuels. However, biomass is frequently used locally near the biomass source without processing it into one of the traded forms.

In previous paragraphs, different biomass materials were classified as woody, herbaceous, fruit, aquatic biomass or biodegradable waste. Another categorization divides the biomass into two wider groups, namely into

1. Virgin Biomass, and
2. Waste Biomass.

Virgin biomass can be further subcategorized into lignocellulosic biomass and carbohydrate (starch). A major part of virgin biomass is lignocellulosic, as it contains the non-digestible fibrous part of the plants including wood, plants and their leaves. Carbohydrate or starch includes all the crops and vegetables, which are digestible by humans. [1, p. 50] This categorization is important not only because the biochemical structure affects the combustion properties of biomass, but also because crops and vegetables are used as a human food. Naturally, land use and food supplies are two important environmental and economical factors when considering the use of biomass in energy production. Because lignocellulosic biomass is not easily digestible by humans, it is preferable to use it in the energy production compared to carbohydrate based biomass. However, starch biomass is widely used in the production of conventional biofuels, such as bioethanol.

The second group of the categorization above, waste biomass, includes all the solid and liquid wastes. It is secondary biomass, since it is derived from the primary biomass during the different stages of the production cycle or use. Waste biomass includes the municipal solid waste (MSW), sewage, animal and human wastes and agricultural wastes. The

municipal solid waste is an important source of biomass, as it includes combustible waste such as food scraps, lawn clippings and paper. Non-renewable contents like plastics and metals are not considered as biomass. The combustible part of the municipal solid waste is often termed as Refuse Derived Fuel (RDF). [1, p. 52] Other examples of waste biomass that can be used for solid fuel combustion include the sewage sludge from waste water treatment and the sawdust from wood processing plants.

Recently, there has been a growing interest towards cultivation of dedicated plants solely for energy production. This biomass is usually referred as *energy crops* and it is mostly lignocellulosic. The advantage of the energy crops is that they have a short growing period, provide a high-energy yield per unit land area and require much less energy and fertilizers for the cultivation, compared to traditional farming [1, p. 51]. Many energy crops, such as willow and poplar, are potential sources for solid biomass combustion.

2.2 Chemical and Physical Combustion Properties of Biomass

2.2.1 Chemical Properties

Biomass, in general, consists of various organic materials such as carbohydrates, fats and proteins. It often contains small amounts of minerals, such as sodium, phosphorus, calcium and iron. Plant based biomass can be divided into three main components, namely, into extractives, cell wall (fibers) and ash. Extractives are proteins, oils, starch, sugars and other substances which can all be separated from the plant with solvents and recovered by evaporation of the solution. [1, p. 54] Cell wall is the major component of biomass, which consists of three main polymers: cellulose, hemicellulose and lignin. These lignocellulosic components constitute of about 95% of the dry weight of plants [9, p. 20]. Finally, the ash contains all the inorganic components that are included in the plants.

From the combustion point of view, the lignocellulosic components of biomass are of the highest interest. The lignocellulosic biomass consist of the three major cell wall components: cellulose, hemicellulose and lignin. Cellulose is a long-chain, crystalline structured, strong polymer represented by the generic formula $(C_6H_{10}O_5)_n$. Its amount in plants varies in dry basis from 33 w-% in most plants, 40–44 w-% in wood to 90 w-% in cotton. [1, pp. 56-58] Cellulose is not water soluble, but it is water-absorbing [9, p. 20].

Hemicellulose is an amorphous, randomly structured, relatively weak polymer. It has a branched chain structure, represented by the generic formula $(C_5H_8O_4)_n$. The compo-

sition and structure of hemicellulose varies significantly among different plants. In dry basis, hemicellulose constitutes approximately 20–30 w-% of most wood. [1, p. 58] Because of its molecular structure, hemicellulose absorbs water easily but relinquishes it slowly [9, p. 21].

Lignin is a complex, three-dimensional, branched polymer which holds the biomass fibers together. The dominant monomeric units in the polymers are benzene rings. The amount of lignin varies highly in different biomass materials. Typical hardwoods and softwoods contain lignin approximately 18-25 w-% and 25-35 w-% in dry basis, respectively. [1, pp. 58-60] Woody biomass has typically much higher lignin content compared to herbaceous biomass. The lignin content also varies in different parts of a single plant. [9, p. 21]

The ratio of lignocellulosic components is an important factor when considering the combustion properties of a biomass. The heating value of a biomass varies with the lignin content, as lignin has the highest heat of combustion out of the three lignocellulosic constituents. The heat of combustion for cellulose and lignin are approximately 18 MJ/kg and 26 MJ/kg, respectively. Therefore, as the softwoods have usually a higher lignin content, they have a higher heating value compared to hardwoods. The extractives have even higher heating values than lignin, but their mass fraction in biomass is usually very low. [10, p. 78]

Another way to understand the heating value of solid fuels is to examine the atomic ratios of oxygen to carbon O/C and hydrogen to carbon H/C. The higher heating value (HHV) of a fuel correlates well with the oxygen to carbon O/C ratio, so that when the O/C ratio increases, the HHV decreases. As biomass has the highest oxygen content of all the hydrocarbon fuels, the heating values are significantly lower compared to the fossil fuels. In combustion, the oxygen consumes part of the hydrogen in biomass and produces water, which affects decreasingly to the heating value. [1, p. 61]

In general, the opposite trend with the heating value holds for the hydrogen to carbon ratio. The effective heating value of the fuel decreases with decreasing H/C ratio [10, p. 302]. A useful diagram known as the *van Krevelen diagram*, presented in Fig. 2.1, plots the atomic ratios of H/C against O/C on a dry ash-free basis (daf).

The van Krevelen diagram shows that biomass has higher H/C and O/C ratios than fossil fuels. The high H/C ratio would indicate a high heating value for biomass, but the high oxygen content in the organic molecules significantly reduces the heat of combustion [10, p. 302]. The van Krevelen diagram is also useful in the sense that it demonstrates how the

heating value depends on the the geological age of the fuel. The oldest fuels locate at the origin of the diagram and the age of the fuel decreases when moving towards biomass.
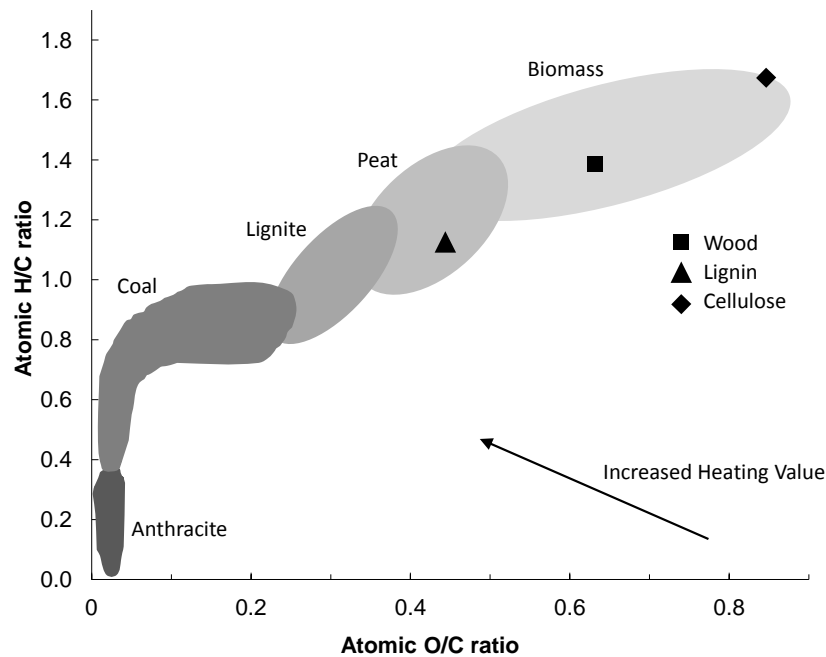
Figure 2.1 *The van Krevelen diagram plots the atomic ratios of H/C against O/C. The ratios can be used for comparing the heating value and the age of different fuels. Figure by Henrik Tolvanen.*

2.2.2 Expressing Chemical Compositions

The chemical composition of a biomass, and other solid fuels, is usually expressed with two types of compositions. These compositions are called the *ultimate* and the *proximate analysis*. In ultimate analysis, the fuel is characterized in terms of the basic elements, moisture and inorganic constituents. Thus, a typical ultimate analysis is of the form

$$C + H + O + N + S + ASH + M = 100\ \%.$$

In the equation above, the amounts of carbon (C), hydrogen (H), oxygen (O), nitrogen (N), sulfur (S), inorganic constituents (ASH) and moisture (M) are expressed in mass percentages. However, some fuels may not include all of these elements. The water content is expressed separately as the moisture (M), and it does not include the hydrogen (H) and oxygen (O) contained in the organic components of the fuel.

As discussed before, biomass has high content of oxygen compared to fossil fuels, which results in a relatively low heating value. In addition, the moisture content in biomass is usually very high. Typical moisture contents vary between 25 and 60 mass percent, depending on the weather conditions and time of harvesting. The traded forms of biomass fuels, such as wood pellets, have usually a lower moisture content of less than 10 percent. The adverse effects of the high moisture content include a delayed ignition and lower adiabatic temperature. The high moisture content lowers down the heating value of the fuel as part of the available energy from combustion is used for the evaporation of the moisture. [12, p.129] Therefore, the biomass has to be properly dried before combustion.

The second way to express the composition of a biomass is the proximate analysis. In proximate analysis, the composition of the fuel is expressed in terms of its gross components and is typically of the form:

$$M + VM + FC + ASH = 100 \text{ %}.$$

In the equation above, the moisture (M), volatile matter (VM), fixed carbon (FC) and inorganic constituents (ASH) are expressed in mass percentages.

The volatile matter (VM) in a fuel includes the condensable and noncondensable vapors which are released when the fuel is heated. The vapors are formed when the chemical structure of the lignocellulosic polymers decomposes in the high temperature. The released volatile matter typically consists of various hydrocarbons, hydrogen, carbon monoxide and carbon dioxide [13]. The amount of released VM depends on the heating rate and final temperature of the fuel and is therefore not a fixed quantity [13, 1, 12]. Biomass fuels have typically a very high volatile content between 60% to 80% of the weight. The amount of volatiles provides information on the ignition and flame properties of the fuel. Fuels with a high volatile content are usually easy to ignite and burn quickly with a large and smoky flame when burned in a grate, whereas the fuels with low volatile content are likely to produce a short and clean flame burning more slowly and being more difficult to ignite [10, p. 297].

The ash content (ASH) in a fuel is the solid residue which is left after the fuel is completely burned. This inorganic residue usually consists of silica, aluminum, iron and calcium together with small amounts magnesium, titanium, sodium and potassium. In fact, ash does not represent the original inorganic matter of the fuel, as part of it may have oxidized during the combustion process. Biomass contains usually very low mass fractions of ash but if the ash contains alkali metals, such as potassium and chlorine, it

may lead to problems in combustion applications such as in fouling and corrosion of the heat transfer surfaces. [1, pp. 75]

Finally, the fixed carbon (FC) represents the solid char content that remains in the fuel after the volatile matter has been released. It is usually calculated as

$$FC = 1 - M - VM - ASH,$$

and thus, its amount depends on the amount of volatile matter released. Because the volatile release is dependent on the heating rate and final temperature of the particle, fixed carbon is not a fixed quantity. Nevertheless, when the FC is measured under standard conditions, it is a useful parameter for evaluating the properties of a fuel. [1, p. 77]

2.2.3 Thermophysical Properties

In addition to the chemical properties described in the previous paragraphs, also the thermophysical properties are important in the fuel characterization. The thermophysical properties describe the heat transfer and heat storage properties of a material. These include, among others, the density, specific heat capacity, thermal conductivity and radiative properties such as emissivity. These properties are important in understanding the combustion properties of a fuel, but most of them are difficult to measure, and they strongly depend on other variables such as the temperature or pressure. For example, the thermal conductivity of a woody biomass is different in the perpendicular and parallel directions to the fiber structure [1, p. 67]. The thermophysical properties can also vary between the different parts of the same plant. As an example, the specific heat capacity of a softwood bark can be higher than the specific heat of the hearth wood [1, p. 69].

Another example of the measurement difficulties for the thermophysical properties is the density. The density can be defined in multiple manners. For a granular matter like pulverized biomass, three definitions are in use, i.e. the *true density*, the *apparent density* and the *bulk density*. The true density is the mass of the solid material divided by the volume occupied by the solid. Thus, it does not include any pores filled by gas inside the particle. In contrast, the apparent density is based on the external volume of the biomass and it includes the internal pores inside the particle volume. Finally, the bulk density is based on the overall space occupied by a large amount of particles. Thus, it includes the internal pores of the particles but also the external space between the particles. From these three densities, the bulk density is the easiest to measure and many standards exist

for its determination. The measurement of the true density or apparent density needs more sophisticated methods. [1, pp. 64–66]

As a conclusion, the combustion properties of biomass vary widely between different fuels. The chemical characteristics, such as the ratio of the lignocellulosic components, vary between different biomasses, but also between the different parts of a same plant. The moisture content varies between the harvesting seasons and depends on the water absorption properties of the lignocellulosic components. Some of the biomass fuels may contain alkali metals and cause slagging and fouling problems in combustion applications. These varying properties make the combustion of biomass challenging. Nevertheless, biomass fuels share some common properties, such as the high volatile and moisture contents, and the generally lower ash content compared to coal. Because of the high O/C ratio, biomass fuels have lower heating values compared to fossil fuels.

2.3 Combustion Stages of a Single Biomass Particle

In solid fuel combustion, the fuel is usually crushed into a small particle size in order to enhance the combustion. The size of the particles depends on the combustion technology. In Fluidized Bed Combustion (FBC) the biomass particles are usually less than 10 mm in diameter, while in Pulverized Fuel Combustion (PFC) the maximum size is typically between 2 to 5 mm [14]. Compared to coal combustion, where the particle size in PFC is below 1 mm, biomass particles are significantly larger. Biomass cannot be effectively milled in such a fine powder due to high energy demand induced by the fibrous structure.

The size of the particles affects greatly on the particle combustion process. In general, two regimes in a single particle combustion can be identified. The thermal Biot number *Bi* defined as:

$$Bi = \frac{d_c h}{k},$$

where d_c is the particle characteristic length, h is the convective heat transfer coefficient and k is the particle thermal conductivity, divides these two combustion regimes. If $Bi << 1$, the particle is considered thermally thin and there are no temperature gradients inside the particle. On the other hand, if $Bi >> 1$, the particle is considered thermally thick and the temperature varies in different parts of the particle. [15]

The combustion process from the raw fuel particle to the remaining ash, can be divided in different stages. These stages are

1. Particle heat up and drying
2. Particle devolatilization (or pyrolysis)
3. Char burnout.

In general, if the particle is fine enough to be thermally thin, the combustion stages occur one after another. In case of large and thermally thick particles, the combustion stages can overlap [15, 16, 9].

In the first stage of particle combustion, the fuel particle starts to heat up mainly by convection from the hot combustion gases and by radiation from the flame and combustion chamber walls. As the particle temperature rises, the moisture inside the particle starts to evaporate. When the particle temperature continues to rise, the chemical structure of the fuel starts to decompose in the so-called devolatilization stage. During devolatilization, the particle releases gaseous components (CO, CO_2, H_2, CH_4, other hydrocarbons), tars and organic vapors to the surrounding gas which then burn in a visible flame. After the thermal decomposition, mainly solid carbon (char) and inorganic ash are left in the particle. This char then burns in heterogeneous surface reactions until only the ash is left in the particle. [9, pp. 31–32] A schematic picture of these steps can be seen in Fig. 2.2.
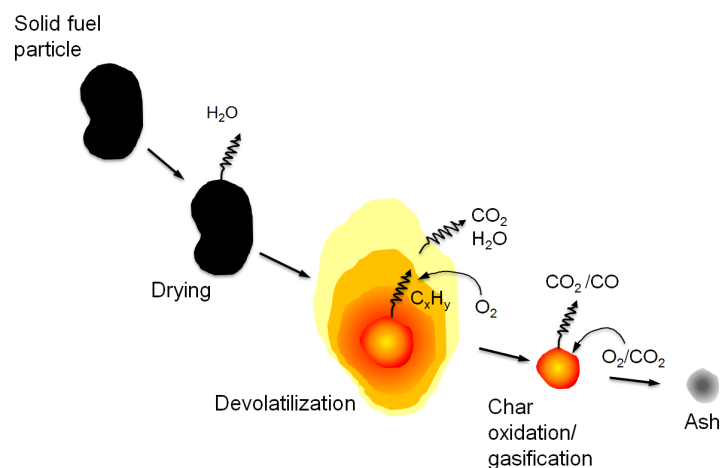
Figure 2.2 Combustion stages of a single solid fuel particle. Figure by Henrik Tolvanen.

In case of pulverized coal combustion, the particle size is usually so small that the particles belong in the Biot number range of thermally thin particles. However, this is rarely the case with biomass. When biomass particles burn, the three combustion stages partly coincide. When the particle surface temperature rises to about 200°C, the dissociation of the lignocellulosic components (cellulose, hemicellulose and lignin) begins and the devolatilization process starts. At the same time, the particle core can be in a significantly

lower temperature, meaning that the water still evaporates from the interior. At about 500°C, the already formed char starts to become gasified with CO_2, H_2O and O_2 forming CO. Finally, at about 700°C, the relatively slow heterogeneous surface reactions begin and the solid carbon reacts with oxygen to form CO and CO_2. When the particle size is large enough, all these phases can occur simultaneously in different parts of the particle. [9, pp. 32-33]

In addition to the particle size, also the particle shape has an effect on the particle combustion process. Because of the fibrous structure of biomass materials, the shapes of milled biomass particles range from nearly spherical to cylindrical and disk/flake-like particles. This differs remarkably from coal, as the milled coal particles are uniformly more spherical. The drag force on the particles depends on the particle shape, and therefore affects the particle trajectories and residence times inside the combustion chamber.

Lu et al. [17] have studied the devolatilization process of a woody biomass by both numerical and experimental methods. They found that the spherical particles exhibit lower volatile yields compared to non-spherical particles having the same mass. In the experiments, they also found that the non-spherical particles lose their mass in devolatilization faster compared to spherical mass-equivalent particles. When the particle mass and the aspect ratio (larger dimension divided by the smaller dimension) increased, the conversion of the non-spherical particles became even faster in comparison with the spherical particles. These effects can be explained with the increasing surface to volume ratio of non-spherical particles compared to spherical ones. A particle with larger surface area has more effective heat transfer surface and thus exhibits a faster heat-up during the combustion process. The faster heat-up increases the volatile yield and reduces the conversion time of the particle.

As a conclusion, the shape and size of the fuel particles have a predominant effect on the particle combustion process. The overlapping combustion stages of the large particles and the effects of the non-spherical shape make the combustion process of a single biomass particle highly complex. These properties complicate the numerical modeling of biomass combustion, which will be discussed in the following chapter.

2.4 Combustion Technologies

The most frequently used biomass combustion technologies can be divided in three main categories [14]:

1. Fixed bed combustion,
2. Pulverized fuel (also called suspension, dust or entrained flow) combustion, and
3. Fluidized bed combustion.

The fixed bed combustion includes a variety of combustion technologies, such as the log wood boilers, understoker furnaces and moving grate furnaces. The biomass is fed onto the grate, and the primary air is typically fed through the bottom to initiate the combustion (under-fire air). Over-fire air completes the combustion process. These types of technologies are simple and can handle fuels with a relatively high moisture content (up to 50 w-%) [14]. However, the boilers efficiencies are relatively low, usually in the range of 50 to 60% [18]. The fixed bed technologies are mainly used for heat generation in small and medium scale units, typically ranging from 0.5 MW_{th} up to 5 MW_{th} [14]. To improve the combustion process and scale up the size of the units, a moving grate can be used instead of a fixed grate. It provides several advantages, such as continuous ash removal and higher boiler efficiencies (65 to 75%) [18]. The moving grate biomass furnaces can scale up to 15 MW in medium scale heat and electricity production [14].

Pulverized fuel combustion, also called suspension or dust combustion, is the technology used in most modern coal-fired power stations. The fuel is ground into a fine powder which is then blown into the combustion chamber through a specifically designed burner. The fuel-air mixture burns inside the combustion chamber in a high-temperature flame. Biomass fuels can be burned with a similar technique, but the particle size has to be small enough (below 5 mm) and the moisture content low enough (less than 20 w-%) to allow the complete burnout of the fuel [14]. Biomass power plants of this type can range up to tens of megawatts. In addition to pulverized fuel power plants dedicated to biomass combustion, the interest towards co-firing biomass with coal in the existing coal plants is increasing rapidly. The advantages of co-firing are the lower specific cost and higher boiler efficiencies (up to 80% [18]) characteristic for the larger power plants (up to 1000 MW_e), and the possibly reduced emission levels due to biomass inclusion [14].

The basic idea behind the third combustion technology, fluidized bed combustion, is to use a bed of inert material inside the combustion chamber. When the fuel is mixed with the inert material, nearly homogeneous temperature and species concentrations can be

achieved. The advantages of the fluidized bed boilers include fuel flexibility, ability to burn fuels with high moisture contents (up to 55 w-%), high boiler efficiencies (80 to 82%) and possibility to include chemical reactants into the bed in order to reduce the pollutant emissions [18]. The fluidized bed technology can be further divided in bubbling and circulating bed types. In Bubbling Fluidized Bed (BFB) combustion, the bed stays at the bottom of the combustion chamber. The combustion air is blown through the bed with a high velocity, making the medium behave in a fluid-like manner. The size range of the BFB boilers is usually between 50 to 150 MW [14]. In Circulating Fluidized Bed (CFB), the air flow rate is even higher and part of the inert material is entrained from the bed. The entrained material is recirculated back to the bed, usually by separating the particles from the gas flow in a cyclone separator. CFB boilers belong usually in the size range of 100 to 300 MW [14], but recently the size of the units has been increasing, examples being the Lagisza power station with a 460 MW CFB boiler in Poland and the Alholmens Kraft power station with a 550 MW CFB boiler in Finland.

3. THEORETICAL BACKGROUND OF NUMERICAL COMBUSTION MODELING

The governing equations in Computational Fluid Dynamics (CFD) are partial differential equations, which together with the boundary conditions describe the motion and heat transfer in fluid systems. These equations are used in a wide range of industries including the aeronautic, automotive and energy industries. CFD tools are used for example in product design and optimization, examples being the designing of an airplane wing and optimizing the air-staging of a boiler in energy production. The advantage of CFD is that it can provide information that is difficult or impossible to measure. It is also a cost-effective tool, as many different product designs can be tested numerically without building expensive prototypes for experimental testing. In this chapter, the theoretical background of biomass combustion (CFD) modeling will be discussed.

3.1 Governing Equations of Fluid Flow

The basis of all fluid flow calculations are the Navier-Stokes equations. Navier-Stokes equations are non-linear partial differential equations that describe the fluid motion in a system with well-defined boundary conditions. These equations are valid as long as the fluid can be treated as a continuous mass (continuum) rather than a collection of single molecules.

The Navier-Stokes equations can be written in the following form using the Einstein tensor notation:

$$\frac{\partial(\rho u_i)}{\partial t} + \frac{\partial(\rho u_i u_j)}{\partial x_i} = -\frac{\partial p}{\partial x_j} + \frac{\partial \tau_{ij}}{\partial x_i} + \rho \sum_{k=1}^{N} Y_k f_{k,j}, \tag{3.1}$$

where ρ is the density of the fluid mixture, u_i are the velocity components, t stands for the time, x_i are the coordinate axes, p is the pressure, τ_{ij} is the viscous stress tensor, Y_k is the mass fraction of species k in the fluid mixture, and $f_{k,j}$ is the volume force acting on species k in j-direction [19, p. 13]. In a physical sense, Eq. (3.1) is the conservation

equation for momentum in a fluid mixture consisting of $k = 1...N$ chemical species. It has the same form in reactive and non-reactive flows. However, in reactive flows such as combustion, the transport properties of the fluid mixture are strongly dependent on the thermodynamic state variables such as temperature or pressure. Therefore, additional equations are needed in order to solve Eq. (3.1). One option is to use the ideal gas equation to relate the density of the fluid to the temperature and pressure. In addition, a theory for the viscous stress tensor τ_{ij} is needed. Usually the mixture can be assumed as a Newtonian fluid and the stress tensor can be obtained from

$$\tau_{ij} = -\frac{2}{3}\mu\frac{\partial u_k}{\partial x_k}\delta_{ij} + \mu\left(\frac{\partial u_i}{\partial x_j} + \frac{\partial u_j}{\partial x_i}\right), \qquad (3.2)$$

where μ is the dynamic viscosity of the mixture and δ_{ij} is the Kronecker delta [19, p. 7].

In addition to the conservation of momentum, the mass and the elementary composition have to be conserved in the fluid system. The conservation of mass can be written in the following form [19, p. 13]:

$$\frac{\partial\rho}{\partial t} + \frac{\partial(\rho u_i)}{\partial x_i} = 0. \qquad (3.3)$$

Eq. (3.3) is also called the continuity equation and it states that the total mass of the system has to be conserved at every instant. In other words, no mass can be created nor destroyed (which applies if there is no radioactive decay in the fluid system). In reactive flows, the continuity equation has the same form, but the chemical reactions can increase and decrease the mass of some species in the fluid mixture. Then, conservation equations also are needed for the chemical species:

$$\frac{\partial(\rho Y_k)}{\partial t} + \frac{\partial}{\partial x_i}[\rho Y_k(u_i + V_{k,i})] = \dot{\omega}_k, \qquad (3.4)$$

where $V_{k,i}$ is the *i*-component of the diffusion velocity of species k and $\dot{\omega}_k$ is the reaction rate of species k [19, p. 13]. Together, Eq. (3.3) and Eq. (3.4) state that the total mass of the system is conserved, but the mass of some of the chemical species may change through the chemical reactions and produce other chemical species. Usually in CFD codes, Eq. (3.4) is solved only for $(N-1)$ species, and the mass of the final species N is obtained directly by subtracting the mass of the calculated $(N-1)$ species from the total mass in the system. In order to solve Eq. (3.4), a theory for the diffusion velocities $V_{k,i}$ has to be obtained, for example through the Hirschfelder and Curtiss approximation for multispecies diffusion [19, p. 14]. In addition, the reaction rates $\dot{\omega}_k$ for the species have to be solved, for example, through the empirical Arrhenius law. For a simple chemical

reaction described by equation $aA + bB \rightarrow cC + dD$, the reaction rate of species A can be expressed using the Arrhenius law as:

$$\dot{\omega}_F = AT^{\alpha}Y_A^a Y_B^b e^{-E_a/R_u T}, \tag{3.5}$$

where A is the pre-exponential factor, T the temperature, α the temperature exponent, Y_A and Y_B the mass fractions of species A and B, E_a the activation energy and R_u the universal gas constant [20, p. 360]. In Eq. (3.5) the reaction rate $\dot{\omega}_F$ has units of $[kg/m^3 s]$, which is the required form for the source term in the species conservation equation. However, the reaction rate equation and the constants it includes are often expressed in many different units, and care must be taken when the equations are used. As seen in Eq. (3.5), the reaction rate depends exponentially on temperature.

Even in simple laminar flows with combustion, there might be hundreds of species and thousands of reactions. This results in enormous number of equations and requires detailed information on the chemical kinetics. When turbulence is added in the problem, a complete solution for a reacting flow is yet impossible to obtain. Therefore, the effects of turbulence are modeled with a turbulence model, and the chemistry is often simplified by global reaction mechanisms. More details about the turbulence modeling and the turbulence chemistry interaction will be presented in Sections 3.2 and 3.3.

The final conservation equation needed to describe a reacting flow is the equation for energy conservation. Conservation of energy can be written in many different forms, for example using the definition of total chemical enthalpy h_t or sensible enthalpy h_s. In some simplified cases the energy conservation can also be directly written as a function of temperature T. Eq. (3.6) presents a general form of the energy conservation written as a function of total energy e_t (sum of chemical, sensible and kinetic energies):

$$\frac{\partial(\rho e_t)}{\partial t} + \frac{\partial}{\partial x_i}(\rho u_i e_t) = -\frac{\partial q_i}{\partial x_i} + \frac{\partial}{\partial x_j}[(\tau_{ij} - p\delta_{ij})u_i] + \dot{Q} + \rho\sum_{k=1}^{N} Y_k f_{k,i}(u_i + V_{k,i}), \tag{3.6}$$

where $\dot{Q}$ is the heat source term, for example due to radiative flux [19, p. 17]. The modeling of the radiation is its own challenging task, and it will be discussed in more detail in section 3.4. It must be noted that while $\dot{Q}$ is the heat source term it does not include the heat released due to combustion, as it is already included in the species enthalpies. The last term on the right hand side of Eq. (3.6) is the power produced by the volume forces f_k on species k in the mixture. Finally, the term q_i accounts for the energy flux in the mixture

and has the form:

$$q_i = -k\frac{\partial T}{\partial x_i} + \rho \sum_{k=1}^{N} (h_k Y_k V_{k,i}), \tag{3.7}$$

where the first term on the right hand side accounts for the heat conduction through Fourier's law (k is the thermal conductivity) and the second term the energy flux through species diffusion in the mixture [19, p. 13].

As discussed above, many different forms of energy conservation exist and the general form in Eq. (3.6) is not very easy to implement. Therefore, the energy equation is often simplified and written in a form that is more easily applicable for the problem in question. The different forms of the conservation of energy can be found on reference [19, p. 21].

The conservation equations presented in this section are the basis of computational fluid dynamics modeling. However, the general forms of the equations are not directly applicable for industrial problems, because of issues caused by the turbulent nature of most real life fluid flows. Furthermore, the general equations or the simplified forms derived from them, are not directly solvable in the differential form they were presented in this section. Because no general mathematical theories exist for solving non-linear partial differential equations, these equations are approximatively solved by numerical methods. This gives the rise for Computational Fluid Dynamics (CFD), where the equations are solved in a finite number of computational cells. The idea behind CFD is to write the partial differential equations in a discrete form, and solve the conservation equations in every computational cell using algebraic equations.

The theory of how to transform the partial differential equations into the discrete form is its own mathematical problem and will not be discussed here in detail. However, the reader is directed to reference [20], which deals with the Finite Volume Method (FVM) for discretizing the governing equations. The FVM is the most common method used in the commercial CFD codes, but other methods also exist, such as the Finite Difference Method (FDM) and the Finite Element Method (FEM).

3.2 Turbulence Modeling

The turbulent nature of most real life fluid flow problems gives rise to most of the difficulties in CFD modeling. Turbulence is always three-dimensional and time-dependent phenomenon, which means that the governing equations (presented in the previous section) would have to be solved in three-dimensional computational grids and with the transient

formulation of the equations. In addition, the smallest scales (Kolmogorov microscales) in turbulent fluid flows are extremely fine. If all details of the flow field are solved in Direct Numerical Simulation (DNS), the time step and cell size have to be smaller than the Kolmogorov microscales. These kind of simulations for industrial scale problems are yet impossible to be solved with the existing computers. A relatively new method for solving the governing equations is the so-called Large Eddy Simulation (LES). In LES, the equations are directly solved down to certain limiting scales (significantly larger than the Kolmogorov scales), while the physics related to the smallest scales are modeled with some approximations. This enables to use larger cell size and time-steps than in the DNS, but the computations are still three-dimensional and transient, and thus computationally demanding.

In order to reduce the computational time of CFD simulations, the Reynolds-averaging procedure is applied. In Reynolds averaging, every variable f in the governing equations is divided into a time-averaged value $\overline{f}$ and a fluctuating component f' around the mean, such that $f = \overline{f} + f'$ (Reynolds decomposition). When the variables in the governing equations are replaced with this definition, and the equations are time-averaged, the so-called Reynolds-Averaged Navier-Stokes (RANS) equations are obtained.

The RANS formulation can be derived for any governing equation of interest, although the name only refers to the Navies-Stokes equations. The idea behind the RANS formulation is that the equations are now written as a function of the time-averaged values of the variables of interest. This enables solving the turbulent flow field in steady state, as the time-averaged values can be assumed independent of time. With RANS formulation, the governing equations can be also solved with a considerably larger cell size, because the length scales of the mean value variations are significantly larger compared to the instantaneous ones [19, p. 136]. These benefits make solving the RANS equations very appealing compared to the computationally expensive DNS and LES calculations. However, RANS solutions do not provide as much information on the problem physics as the other options presented, and they also need many closure models to obtain a solution. Because every closure model has its own assumptions, the solutions may be inaccurate.

In reactive flows and combustion modeling, the Favre average formulation (mass-weighted average) is usually preferred. Favre averaging is favorable in cases where the density fluctuations are large, because they give rise to many unknown variables that would have to modeled if Favre averaging was not applied [19, p. 141]. The Favre average value of a variable f can be written is a similar manner as in Reynolds averaging, such that

$f = \widetilde{f} + f''$, where $\widetilde{f}$ is the mass-weighted average and f'' the fluctuating component around the mean. The relation between Reynolds and Favre averaged values is obtained through:

$$\widetilde{f} = \frac{\overline{\rho f}}{\overline{\rho}},$$

and thus, the mass-weighted time-average values are solved from the governing equations [19, p. 141]. Using the definitions above, all the governing equations presented in the previous section can be written as a function of the Reynolds and Favre averaged values. As an example, Eq. (3.8) presents the Navier-Stokes equations in this form (volume forces neglected) [19, p. 141]:

$$\frac{\partial(\overline{\rho}\widetilde{u}_i)}{\partial t} + \frac{\partial(\overline{\rho}\widetilde{u}_i\widetilde{u}_j)}{\partial x_i} = -\frac{\partial\overline{p}}{\partial x_j} + \frac{\partial}{\partial x_i}\left(\overline{\tau_{ij}} - \overline{\rho}\widetilde{u_i''u_j''}\right). \qquad (3.8)$$

The transient term (first term on left hand side) is usually excluded from the calculations and only the average values are solved. However, the so-called Unsteady Reynolds-Averaged Navier-Stokes (URANS) simulations can solve the transient behavior of the mean values if the term is included. The averaged forms of the other governing equations can be found for example in reference [19].

The last term on the right hand side of Eq. (3.8) constitutes the central problem in RANS formulation. The correlations between the fluctuating components f'' and other variables are new unknown terms that rise in the Reynolds averaging procedure, and they have to be modeled in some way in order to obtain a solution for the problem. The last term on the right hand side represents the so-called Reynolds Stresses, which in a physical sense describe the apparent stresses related to the turbulent motion of the fluid flow. However, no general law has been found for these stresses, as they strongly depend on the nature of the specific fluid flow. These terms give rise to the turbulent closure problem and many different turbulence models have been developed in order to obtain a solution for the stresses.

The most commonly used turbulence model is the k-ε model and its variations, such as the Realizable k-ε model. In these models, the Reynolds Stresses (9 in total, 6 independent) are calculated using two new variables, the turbulent kinetic energy k and the turbulent kinetic energy dissipation rate ε, which are solved from equations that can be derived from the Navier-Stokes equations. The advantage of these models is that only two new equations have to be solved in order to obtain all six unknown Reynolds Stresses. However, many assumptions (such as isotropic turbulence) have been made in deriving the equa-

tions for k and ε, and therefore they can provide inaccurate results in some flow cases [20, p. 68].

Another commonly used turbulence model is the Reynolds-Stress-Model (RSM), which solves a transport equation individually for the six independent Reynolds-Stresses, and one for the turbulent kinetic energy dissipation rate. The RSM requires seven new equations to be solved together with the averaged governing equations, and therefore it is computationally more expensive compared to the k-ε models. However, the RSM can provide more accurate results in situations where the turbulence is exceedingly non-isotropic [20, p. 93], such as in highly swirling flows.

In addition to the models above, many other turbulence models exist, some examples being the Mixing-Length model (no additional equations), Spalart-Almaras model (1 additional equation) and $k - \omega$ model (2 additional equations). More details about the different turbulence models can be found for example in reference [20].

3.3 Turbulence and Chemistry Interaction

As discussed in the previous section, most of the real life fluid problems involve a turbulent flow. When the turbulent flow enters a flame, the chaotic velocity fluctuations and the complex chemical reactions impact on one another. The material properties change rapidly over the flame front, which modifies the flow turbulence (mainly increasingly). On the other hand, the turbulent fluctuations in the incoming gas alter the flame structure, which in turn affects the flame properties. The turbulent eddies often increase the mixing between the reactant gases, which results in a more efficient combustion compared to laminar flame structures. [19, pp. 125–126] This section presents the basic theory for turbulent combustion modeling. For detailed information, the reader is directed to reference [19].

The Reynolds and Favre averaging procedures were discussed in the previous section, and the time-averaged form of the momentum equation was introduced. The Reynolds stresses were identified in the time-averaged momentum equations, as they give rise for the need of turbulence modeling. When the species conservation equations described by Eq. (3.4) are averaged, the following form is obtained [19, p. 141]:

$$\frac{\partial (\overline{\rho}\widetilde{Y_k})}{\partial t} + \frac{\partial}{\partial x_i}\left(\overline{\rho}\widetilde{u_i}\widetilde{Y_k}\right) = -\frac{\partial}{\partial x_i}\left(\overline{V_{k,i}Y_k} + \overline{\rho}\widetilde{u_i''Y_k''}\right) + \overline{\dot{\omega}_k}. \tag{3.9}$$

Similarly with the momentum equation, the time-averaging introduces new unknown variables. In order to solve the average mass fractions $\widetilde{Y}_k$ of species k, the terms on the right hand side of Eq. (3.9) have to closed with appropriate models. The laminar diffusive fluxes $\overline{V_{k,i}Y_k}$ of species k are generally neglected by assuming large Reynolds numbers and insignificant effect compared to turbulent transport. They can also be included by using laminar diffusivity and classical gradient assumption [19, p. 143].

Furthermore, the turbulent fluxes are usually closed by the classical gradient assumption:

$$\overline{\rho}\widetilde{u_i''Y_k''} = -\frac{\mu_t}{Sc_{kt}}\frac{\partial \widetilde{Y}_k}{\partial x_i}, \tag{3.10}$$

where μ_t is the turbulent viscosity determined from the variables of the turbulence model (k and ε), and Sc_{kt} the turbulent Schmidt number of species k [19, p. 147].

Determining the mean reaction rate $\overline{\dot{\omega}_k}$ in Eq. (3.9) constitutes the central problem in turbulent combustion modeling. If the Arrhenius equation is averaged similarly with the other governing equations, many new unknown variables appear due to the high non-linearity of the equation. Therefore, the mean reaction rates are closed with models that are based on physical analysis concerning the interaction between turbulence and the chemical kinetics [19, p. 147].

Many different models for the mean reaction rate have been developed, such as the Eddy Dissipation Model (EDM) and Eddy Dissipation Concept (EDC). However, models have been developed that do not require solving all the species conservation equations separately every species. These models describe the chemistry using one single variable, called the mixture fraction. The mixture fraction models require statistical methods and use Probability Density Functions (PDF) to describe the flow variables. In general, the different models are often suitable for only a single combustion regime, because the physical phenomena in premixed and non-premixed combustion have many dissimilarities. Detailed information about the different turbulence-chemistry interaction models can be found in [19, 20].

The EDM model of Magnussen and Hjertager (see Fluent theory guide [6]), is used in the 50kW reactor modeling of this work. The idea of the EDM model is based on observation that the overall reaction rate in both premixed and non-premixed combustion is often controlled by the flow turbulence. In premixed flames, the turbulence mixes the cold reactants and hot products into the reaction zones where the chemical reactions occur, while in non-premixed flames the turbulent mixing of the fuel and oxidizer control the

combustion [6]. In these situations, the chemical kinetics can often be assumed infinitely fast and the combustion is said to be mixing-limited.

In the EDM model, assuming the mixing-limited combustion regime, the reaction rate is calculated directly using the turbulence variables (k and ε) and the species concentrations. In ANSYS Fluent, the effects of chemical kinetics can be included in the simulations by using the so-called Finite-Rate/Eddy-Dissipation model. The model calculates both the EDM reaction rate, and the reaction rate from the Arrhenius equation that is written for the mean flow variables, and takes the net reaction rate as the minimum of these two. More details about the Finite-Rate/Eddy-Dissipation Model can be found on Fluent theory guide [6] and in reference [20].

3.4   Radiation Modeling

The heat transfer due to radiation can be described by the radiative transfer equation (RTE). The RTE for an absorbing, emitting and scattering medium can be expressed in the following form:

$$\frac{dI(\vec{r},\vec{s})}{ds} = \kappa I_b(\vec{r}) - \beta I(\vec{r},\vec{s}) + \frac{\sigma_s}{4\pi} \int_{4\pi} I_-(\vec{s}_i)\Phi(\vec{s}_i,\vec{s})d\Omega_i, \qquad (3.11)$$

where $I(\vec{r},\vec{s})$ is the radiant intensity at position $\vec{r}$ in direction $\vec{s}$, κ is the absorption coefficient of the fluid mixture, I_b the black body intensity, σ_s its scattering coefficient, $\beta = \kappa + \sigma_s$ the extinction coefficient, $I_-(\vec{s}_i)$ the intensity upon the point at $\vec{r}$ from all possible directions $\vec{s}_i$, $\Phi(\vec{s}_i,\vec{s})$ the scattering phase function [20, p. 424]. The integration on the right hand side is conducted over a unit sphere (solid angle of 4π steradians) surrounding the particular point at $\vec{r}$ in the medium, in order to obtain the in-scattered intensity from all possible directions. The physical significance of the terms in the RTE from left to right are the following:

1. Change in the radiation intensity per unit path length
2. Intensity emitted by the fluid mixture
3. Intensity absorbed by the fluid mixture
4. Intensity scattered out of the fluid mixture
5. Intensity scattered into the fluid mixture from the surroundings [20, p. 424].

In combustion simulations, the radiant intensity $I(\vec{r},\vec{s})$ has to be solved in order to obtain the heat source term due to radiation in the energy equation. For solving the radiant in-

tensity, the radiative properties of the fluid mixture have to be known. However, these properties, i.e. the absorption coefficient, scattering coefficient and phase function, are in general strongly dependent on other flow variables. The absorption coefficient κ depends on the fluid temperature, species concentrations and pressure. The scattering coefficient σ_s and the scattering phase function $\Theta(\vec{s_i}, \vec{s})$ depend on the properties of the particulate matter contained in the fluid mixture, such as the size, shape, concentration and material properties of the particulates. Furthermore, all these properties have a complex wavelength dependence, and for accurate simulations the radiation has to be spectrally resolved, or the wavelength dependence somehow modeled. [20, p. 420]

The wavelength dependence of the radiative properties make the radiation calculations computationally expensive and complicated, as the RTE would have to be solved independently for a large number of wavelength bands in order to obtain a complete solution. For this reason, in practical purposes the radiative properties are evaluated globally using approximations, for example based on experimental data. The most widely used method in combustion simulations is the so-called Weighted-Sum-of-Grey-Gases Method (WSGGM), which is a reasonable compromise between the gray gas assumption and the whole wavelength range solution for estimating the mixture absorption coefficient [6].

Exact analytical solutions for the RTE have been derived only for simple idealized cases. In general combustion applications, the modeling has to be conducted in three-dimensions and the equation has to be solved in all angular directions. Many different numerical models have been developed in order to solve the RTE and most of them follow a similar iterative solution procedure. The iterative procedure is required because the integral term of Eq. (3.11) is initially unknown. The iterations begin by assumed values for the surface intensities. After calculating a sufficient number of ray paths, the integral terms can be evaluated. This provides more accurate estimations for the surface intensities and the iterative process continues. [20, p. 426]

In the commercial CFD software ANSYS Fluent, multiple radiation models are available, including the P-1 model, Discrete Transfer Radiation Model (DTRM) and Discrete Ordinates (DO) model. In combustion simulations, the DO model is often applied and it is also used in the simulations of this work. The idea behind the DO model is to solve the RTE for a finite number of discrete solid angles, each associated with a vector direction $\vec{s}$. The RTE is transformed into a transport equation for the radiant intensity, similar to the fluid flow equations, and the transport equation is solved for all directions $\vec{s}$. Fluent offers two implementations of the DO model, which are referred as the finite-volume scheme

and the coupled ordinates method (COMET). [6] More information on the DO model and other radiation models can be found in [6, 20].

3.5 Particle Combustion Modeling

In general, multiphase flows (fluid flow including solid particles, bubbles or droplets) can be treated in three different manners. The first option, called as the Eulerian-Lagrangian treatment, is to treat the fluid as a continuous (Eulerian) phase and the discrete phase (particulate phase) as a Lagrangian phase. In Lagrangian particle treatment, the properties of a single particle are calculated as it moves together with the fluid flow and the possible effects on the flow field are included via source terms. In this approach, the idea is to repeat this procedure for a representative number of particles in order to obtain a solution for the multiphase flow. The second option is to use the Eulerian-Eulerian approach, where the discrete phase is not treated as single particles but rather as a continuum in a similar manner as the fluid flow. The choice between the Eulerian-Lagrangian and the Eulerian-Eulerian methods depends on the physical problem examined. The Eulerian-Eulerian treatment is usually preferred for high particle concentrations, because the computational time of the Lagrangian particle treatment increases drastically when the number of particles increases and when the particle-particle interactions have to be taken into consideration. The third and less popular option for multiphase flows is to use probabilistic formulation for the discrete phase. In this approach, the distribution of the particles in a continuous phase is calculated based on a Probability Density Function (PDF).

Flows with discrete particles can be divided into three groups depending on the level of interaction between the different phases. In one-way coupling, the discrete phase has no effect on the flow field. This means that the movement of the particles can be calculated after the flow field solution is obtained. One-way coupling can be used in situations where the particles occupy a very low volume fraction α_P in the flow (below 10^{-6} [21]). In two-way coupling, the particles exchange momentum, mass and energy with the continuous phase and it is recommended when particle volume fraction is roughly between $10^{-6} < \alpha_P < 10^{-3}$ [21]. Finally, if the particle concentration is so high that the particles have a significant impact on one another, for example through collisions, the particle-particle interactions have to taken into consideration. This approach is often referred as four-way coupling and it is recommended for flows having a discrete phase volume fraction α_P higher than 10^{-3} [21]. The theory presented in this section will concentrate on the Lagrangian particle treatment and two-way coupling between the gas and particle phases, which are commonly used in combustion simulations. The theory focuses on the Discrete

Phase Model (DPM) of ANSYS Fluent [6], which is used in the CFD modeling cases of this work.

In the DPM model of ANSYS Fluent, the particles are treated in a Lagrangian way and their effect on the flow field is included in the continuous phase equations via source terms (two-way coupling). Therefore, the particles can exchange heat, mass and momentum with the gas stream. The strategy for the simulation is to alternate the Eulerian flow field and Lagrangian particle trajectory calculations as long as the converged solution is obtained. The following sections will represent the theory of the DPM model.

3.5.1 Particle Trajectories

The particle velocity at every instant during its travel in the fluid flow can be determined by writing the Newton's second law and integrating it over the time. The equation of motion can be written per unit particle mass in the following form:

$$\frac{d\vec{u}_p}{dt} = f_D(\vec{u} - \vec{u}_p) + \frac{\vec{g}(\rho_p - \rho)}{\rho_p} + \vec{f},$$

(3.12)

where $\vec{u}_p$ is the particle velocity vector, $\vec{u}$ the surrounding gas velocity, ρ_p and ρ the particle and gas densities and $\vec{f}$ the additional forces (per unit particle mass) affecting the particle [6]. Fluent offers multiple forces to be included in the additional forces, such as the Brownian force and the thermophoretic force. Full details can be found in Fluent theory guide [6]. The second term on the right hand side of Eq. (3.13) represents the force of gravity, while the first term represents the drag force on the particle. The variable f_D is obtained through:

$$f_D = \frac{18\mu}{\rho_p d_p^2} \frac{C_D Re}{24},$$

(3.13)

where μ is the dynamic viscosity of the fluid, d_p the particle (spherical) diameter, C_D the drag coefficient and $Re = \rho d_p \left| \vec{u}_p - \vec{u} \right| / \mu$ the particle Reynolds number [6].

In order to solve the particle trajectory in the fluid flow, Eq. (3.13) can be solved together with equation

$$\vec{u}_p = \frac{d\vec{x}_p}{dt},$$

(3.14)

where $\vec{x}_p$ is the particle position vector [6]. Equations (3.13) and (3.14) form a set of coupled ordinary differential equations, which can be solved by integrating the equations

over discrete time-steps for obtaining the particle velocity and position in the fluid flow at each instant.

The equation set has to be closed by an appropriate equation for the drag coefficient. Fluent offers multiple choices, including a spherical drag and a non-spherical drag law. For biomass particles that will be further examined in this thesis, the non-spherical drag law is the most suitable option as the biomass particles are often highly irregular in shape. The non-spherical drag law uses the correlation developed by Haider and Levenspiel [22], which has been found satisfactory for many different particle shapes and flow regimes [25]. Thus, the drag coefficient is obtained through

$$C_D = \frac{24}{Re_{sph}} \left(1 + b_1 Re_{sph}^{b_2}\right) + \frac{b_3 Re_{sph}}{b_4 + Re_{sph}}, \tag{3.15}$$

where Re_{sph} is the particle Reynolds number calculated using the sphere-equivalent particle diameter (the sphere and the real particle have the same volume) [6]. The coefficients b_1, b_2, b_3, b_4 are functions of the shape factor SF (see Fluent theory guide for full equations), which is defined as

$$SF = \frac{A_{sph}}{A}, \tag{3.16}$$

where A_{sph} is the surface area of the sphere-equivalent particle and A the actual surface area of the particle [6].

In case of biomass, the particles are often cylindrical in shape. The shape factor of a cylinder SF_c can be obtained through

$$SF_c = \frac{d_{sph}^2}{\left(AR + \frac{1}{2}\right) d_c^2}, \tag{3.17}$$

where d_{sph} is the sphere-equivalent particle diameter, d_c the diameter of the cylinder and AR the aspect ratio of the cylinder (length divided by diameter). Eq. (3.16) can be used as a first approximation for the shape factor of biomass particles.

In addition to the forces presented above, the turbulent fluctuations in turbulent flow regimes have a significant effect on the particle trajectories. The Discrete Random Walk (DRW) model in Fluent offers a way to include these effects on the particle trajectories. In the DRW model, the turbulent velocity fluctuations are considered by using the instantaneous gas velocity $u_i(t)$ in the particle trajectory calculations, which is obtained from the Reynolds decomposed form $u_i(t) = \bar{u}_i + u'_i(t)$. The mean velocity $\bar{u}_i$ is obtained from

the continuous phase calculations and the velocity fluctuations $u'_i(t)$ are modeled using a Gaussian probability distribution and the variables obtained from the turbulence model. When the Reynolds decomposed form of the gas velocity is used in the particle trajectory calculations, the random effects of turbulence can be taken into account. The trajectory calculations can be repeated for a sufficient number of particles (termed as number of tries in Fluent), so that the turbulent dispersion is extensively accounted. However, the DRW includes a modeling constants and the accuracy of the method can depend on the flow in question.

3.5.2 Laws for Heat and Mass Exchange

The heat and mass transfer of the combusting particles can be modeled using six different laws in the DPM model of ANSYS Fluent [6]. The laws describe the different particle combustion stages presented in Section 2.3, i.e. the particle heat up, water evaporation, devolatilization and char burnout. The water content of the fuel can be modeled using the Wet Combustion Model, which includes an additional water droplet inside the combustible particle. As a default, the different laws can be activated only one at a time. The six laws are presented in Table 3.1 together with their validity ranges.

Table 3.1 *Laws of the DPM model in ANSYS Fluent [6], used in particle combustion modeling.*

Combustion stage	Law Validity
Inert heating or cooling (Law 1 and Law 6 in Fluent)	$T_p < T_{vap}$ or $T_p < T_{dev}$ and $m_p \leq (1 - f_{v,0} - f_{comb})(1 - f_{w,0})m_{p,0}$
Water evaporation (Law 2 in Fluent)	$T_{vap} \leq T_p < T_{bp}$ and $m_p > (1 - f_{w,0})m_{p,0}$
Water boiling (Law 3 in Fluent)	$T_p \geq T_{bp}$ and $m_p > (1 - f_{w,0})m_{p,0}$
Devolatilization (Law 4 in Fluent)	$T_p \geq T_{dev}$ and $m_p > (1 - f_{v,0})(1 - f_{w,0})m_{p,0}$
Char burnout (Law 5 in Fluent)	$m_p \leq (1 - f_{v,0})(1 - f_{w,0})m_{p,0}$ and $m_p > (1 - f_{v,0} - f_{comb})(1 - f_{w,0})m_{p,0}$

Law 1, the inert heating and cooling, is applied as long as the particle temperature T_p is below the user-defined (water) vaporization temperature T_{vap}. It is also applied after the particle drying stage, if the particle temperature is still below the user-defined devolatilization temperature T_{dev}. The vaporization and devolatilization temperatures are modeling

constants which allow the user to define a temperature where the water evaporation and devolatilization begin. Law 6, on the other hand, is applied after the user-defined initial mass-fractions of water $f_{w,0}$, volatiles $f_{v,0}$ and char f_{comb} have been consumed from the particle. Thereafter, the ash content of the particle is heated or cooled via Law 6.

After the particle temperature reaches the evaporation temperature T_{vap}, it transfers to law 2. During law 2, the water content in the fuel is evaporated until it is completely consumed, or until the particle temperature has reached a user-defined boiling point temperature T_{bp} (commonly 100°C). If the particle reaches the boiling point temperature T_{bp} before all the water has been evaporated, the rest of the water is being consumed via water boiling law (Law 3). During the boiling law, the particle remains at a constant temperature (T_{bp}).

The devolatilization law (law 4) begins after the particle has completely dried. However, the devolatilization can only begin after the particle has reached a user-defined devolatilization temperature T_{dev}. Therefore, the particle can be heated via law 1 before the devolatilization begins. Finally, the char combustion stage initiates as soon as the volatile fraction $f_{w,0}$ is consumed, and continues until there is only ash left in the particle. The following sections present the theory behind the six laws.

Inert Heating and Cooling (Law 1 and Law 6)

During laws 1 and 6, the particle is heated via convection and radiation. A simple heat balance can be written for the particle:

$$m_p c_p \frac{T_p}{dt} = hA_p(T_\infty - T_p) + \varepsilon_p A_p \sigma(\Theta_R^4 - T_p^4), \tag{3.18}$$

where m_p is the particle mass, c_p the specific heat capacity, h convective heat transfer coefficient, A_p the particle surface area, T_∞ the surrounding gas temperature, T_p the particle temperature, ε_p the particle surface emissivity, σ the Stefan-Boltzmann constant, $\Theta_R = (G/4\sigma)^{1/4}$ the radiation temperature and G the incident radiation on the particle surface [6]. During the laws 1 and 6, Eq. (3.18) is integrated over time the discrete time-steps, and solved in conjunction with the particle trajectory calculations for obtaining the particle temperature T_p at each time step. It is important to note here, that the particle is considered isothermal.

In order to solve Eq. (3.18), an expression for the convective heat transfer coefficient h is needed. Fluent uses the correlation of Ranz and Marshall [23, 24], which can be written as

$$Nu = \frac{hd_p}{k} = 2.0 + 0.6(Re^{1/2}Pr^{1/3}), \tag{3.19}$$

where Nu stand for the Nusselt number, k for the particle thermal conductivity and Pr for the Prandtl number of the surrounding fluid [6]. The particle is assumed isothermal and spherical.

Water Evaporation (Law 2)

The heat transfer on the water droplet inside the fuel particle is calculated with a similar equation as Eq. (3.18), but the latent heat required for the water evaporation is included on the right hand side. This results in the following equation:

$$m_p c_p \frac{T_p}{dt} = hA_p(T_\infty - T_p) + \varepsilon_p A_p \sigma(\Theta_R^4 - T_p^4) - \frac{dm_p}{dt} h_{fg}, \tag{3.20}$$

where the subscript p refers now to properties of the water droplet inside the combusting particle and h_{fg} is the latent heat of water [6].

The release of water from the particle to the surrounding gas (dm_p/dt) can be calculated with either Diffusion Controlled or Convection/Diffusion Controlled model. In both models, the mass transfer coefficient k_c is calculated using a Sherwood number correlation [23, 24], similar to the convective heat transfer:

$$Sh_{AB} = \frac{k_c d_p}{D_{i,m}} = 2.0 + 0.6Re_d^{1/2}Sc^{1/3}, \tag{3.21}$$

where Sh_{AB} stands for the Sherwood number, $D_{i,m}$ is the bulk diffusion coefficient of water vapor and $Sc = \mu/\rho D_{i,m}$ is the Schmidt number. More details about the evaporation models can be found in Fluent theory guide [6].

Water Boiling (Law 3)

The water boiling law is applied if the particle temperature reaches the user-defined boiling point temperature before all the water has evaporated from the particle. During the boiling law, the particle temperature is assumed constant and the term on the left hand

side of Eq. (3.20) becomes zero. The change in the particle mass after each time-step can be derived from the resulting equation, which yields

$$\frac{d(d_p)}{dt} = \frac{2}{\rho_p h_{fg}} \left[\frac{k_\infty Nu}{d_p}(T_\infty - T_p) + \varepsilon_p \sigma(\Theta_R^4 - T_p^4) \right], \tag{3.22}$$

where the subscript p refers to properties of the water droplet inside the combusting particle. The Nusselt number Nu can be solved by Eq. (3.19) [6].

Devolatilization (Law 4)

The devolatilization stage of the particle combustion can be modeled with multiple different submodels in Fluent. The Single Kinetic Rate and the Two Competing Rates (Kobayashi) models will be discussed in more detail, as these models are later used in the biomass devolatilization modeling.

During devolatilization phase, the heat transfer on the particles is obtained from Eq. (3.20), but the latent heat h_{fg} is replaced by the heat required for the volatile species formation. The mass transfer of volatiles from the particle to the surrounding gas is calculated with the equation of the chosen submodel. In the Single Rate model, it is assumed that the devolatilization rate is first-order dependent on the amount of volatiles remaining in the particle:

$$-\frac{dm_p}{dt} = k[m_p - (1 - f_{v,0})(1 - f_{w,0})m_{p,0}], \tag{3.23}$$

where k is the apparent kinetic rate of the devolatilization, $f_{v,0}$ the initial mass fraction of volatiles, $f_{w,0}$ the initial mass fraction of water and $m_{p,0}$ the initial particle mass [6]. The kinetic rate k is calculated via Arrhenius equation:

$$k = Ae^{-(E/R_u T_p)}, \tag{3.24}$$

where A is the pre-exponential factor, E the activation energy and R_u the universal gas constant [6]. The aim of the reactivity parameter optimization for the two biomass fuels, that will be presented in Section 5.2, is to define the pre-exponential factors A and the activation energies E such that the mass loss of the biomass particles matches with the experiments.

In the Kobayashi devolatilization model, the mass loss rate of the particles is calculated using two different kinetic rates $\Re_1$ and $\Re_2$, that may control the devolatilization in dif-

ferent temperature ranges [6]. The idea of the Kobayashi model is to take into account the experimentally observed behavior, that the final mass loss level after devolatilization may vary depending on the particle temperature history and heating rate. However, as a default the mass fraction of volatiles $f_{v,0}$ in the particles is a pre-determined constant in the DPM model, and the particles have to reach this mass loss level independently of the particle temperature history and heating rate. Nevertheless, the Kobayashi model offers some flexibility on the shapes of the particle mass loss curves as the two competing rates are applied.

The mass loss rate in the Kobayashi model is obtained through:

$$\frac{m_v(t)}{(1 - f_{w,0})m_{p,0} - m_a} = \int_0^t \left(\alpha_1 \Re_1 + \alpha_2 \Re_2 \right) e^{-\int_0^t (\Re_1 + \Re_2)dt} dt, \qquad (3.25)$$

where $m_v(t)$ is the volatile yield up to time t, m_a is the ash content in the particle, and α_1 and α_2 are the yield factors of the two competing reactions [6]. The kinetic rates $\Re_1$ and $\Re_2$ are obtained from the Arrhenius equations [6]:

$$\Re_1 = A_1 e^{-(E_1/RT_p)}, \qquad (3.26)$$

$$\Re_2 = A_2 e^{-(E_2/RT_p)}. \qquad (3.27)$$

In a physical sense, the kinetic rate $\Re_1$ represents the devolatilization in a lower temperature level, while the kinetic rate $\Re_2$ is for very high temperatures [6]. The yield factors α_1 and α_2 represent the volatile yields that would be achieved at the lower and higher temperature levels. In case of the Kobayashi model, the reactivity parameter optimization for the two biomass fuels aims to determine the pre-exponential factors, activation energies and yield factors so that the particle mass loss matches with the measurements in a best possible way.

In addition to the heat and mass transfer, the change in the particle size can be modeled during devolatilization. A model constant called the swelling coefficient C_{sw} can be chosen in the Fluent software in order to account the swelling or shrinking of the fuel particles. The change in the particle diameter is calculated through the following equation:

$$\frac{d_p}{d_{p,0}} = 1 + (C_{sw} - 1)\frac{(1 - f_{w,0})m_{p,0} - m_p}{f_{v,0}(1 - f_{w,0})m_{p,0}}, \qquad (3.28)$$

where $d_{p,0}$ is the particle diameter at the start of devolatilization and d_p the current particle diameter [6]. Eq. (3.28) states that the particle diameter depends on the ratio of the

devolatilized mass to the total volatile mass. When the swelling coefficient is equal to 2.0 the particle diameter doubles during the devolatilization process, while a value of 0.5 results in a diameter half of the initial diameter [6].

Char Burnout (Law 5)

The char burnout model is also called as the surface reaction model, because the solid char is consumed at the particle surface in heterogeneous reactions. Fluent offers multiple choices for the char burnout stage modeling. The Kinetics/Diffusion Limited Rate model will be discussed in further detail, as it was chosen for the biomass combustion modeling later presented in this thesis. With the Kinetics/Diffusion Limited Rate model, only one particle surface reaction can be accounted, which is described by

$$\text{Char (s)} + S_b \text{Oxidizer (g)} \rightarrow \text{Product (g)}, \tag{3.29}$$
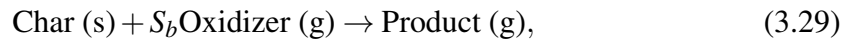
where S_b is the mass of oxidant per mass of char [6]. The Kinetics/Diffusion Limited Rate model assumes that the reaction rate for Eq. (3.29) is limited either by the chemical kinetics or by the diffusion of oxygen to the particle surface. Fluent uses the model of Baum and Street [26] and Field [27], where the kinetic rate $\Re$ and the diffusion rate coefficient D_0 determine the char combustion rate as follows:

$$\frac{dm_p}{dt} = -A_p p_{ox} \frac{D_0 \Re}{D_0 + \Re}, \tag{3.30}$$

where p_{ox} is the partial pressure of oxygen surrounding the particle [6]. The diffusion rate coefficient is obtained through

$$D_0 = C_1 \frac{[(T_p + T_\infty)/2]^{3/4}}{d_p}, \tag{3.31}$$

where C_1 is a modeling constant with a default value of $5 \cdot 10^{-12}$ in Fluent [6]. Furthermore, the kinetic rate is obtained through the Arrhenius equation [6]:

$$\Re = C_2 e^{(-E/RT_p)}. \tag{3.32}$$

Again, the goal of the reactivity parameter optimization for the two biomass fuels is to obtain appropriate values for the model parameters C_1, C_2 and E. In the Kinetics/Diffusion

Limited Rate model the particle diameter is kept constant, which results in a decreasing particle density as the char combustion proceeds.

The heat transfer during char combustion stage is modeled with a similar heat balance as presented in the previous sections. However, the heat released from the char burnout reaction has to included, which results in:

$$m_p c_p \frac{T_p}{dt} = hA_p(T_\infty - T_p) + \varepsilon_p A_p \sigma(\Theta_R^4 - T_p^4) - f_h \frac{dm_p}{dt} H_{reac}, \qquad (3.33)$$

where H_{reac} is the heat release from the char burnout reaction and f_h the fraction the particle absorbs in itself [6]. Therefore, only the fraction $(1 - f_h)$ of the heat release is included in the continuous phase sources.

4. EXPERIMENTAL METHODS

This chapter introduces the experimental test facilities, and the measurements that were conducted during the biomass reactivity studies. The chapter begins with Section 4.1, in which the Drop-Tube Reactor (DTR) test facility at Tampere University of Technology (TUT) is introduced. The DTR was used for determining the reactivity of two biomass fuels, which are denoted as biomass fuel 1 and biomass fuel 2 in this work. The properties of these two fuels are presented in Section 4.2. The chapter ends with Section 4.3, where the experimental measurements with the DTR are introduced. The experimental work was conducted by B.Sc. Teemu Saarinen during his Master of Science thesis work [5].

4.1 Drop-Tube Reactor (DTR) Test Facility

A schematic picture of the Drop-Tube Reactor (DTR) test facility at Tampere University of Technology (TUT) is shown in Fig. 4.1. The DTR consists of three modular parts: a cylindrical reactor part, a particle feeding probe, and a particle collection system. In addition to the reactor, a system for particle geometry analysis exist at the test facility and it is also shown in the figure.

The reactor part of the DTR is made of austenitic stainless steel and it has an inner diameter of 2.67 cm and a temperature resistance of up to 1300°C. The reactor can be electrically heated and it has eight separately adjustable heating elements. The heating elements are insulated with a 5 cm layer of kaowool insulator. The length of the reactor part is 67.5 cm. In order to prevent excess heating of the collection system, the final 2.5 cm of the reactor part is not covered by the heating elements. Two measuring windows are placed in the lower end of the reactor, having a center point at 53.5 cm from the reactor top. The CCD camera and the two-color pyrometer can be used for particle velocity and temperature measurements through the windows. The reactor can be filled with different gas atmospheres by feeding gas from the reactor top. The gas flows into the reactor through a flow straightener and it enters between the feeding probe outer wall and the reactor inner wall. The flow rate of the gas can be regulated with a mass flow controller.
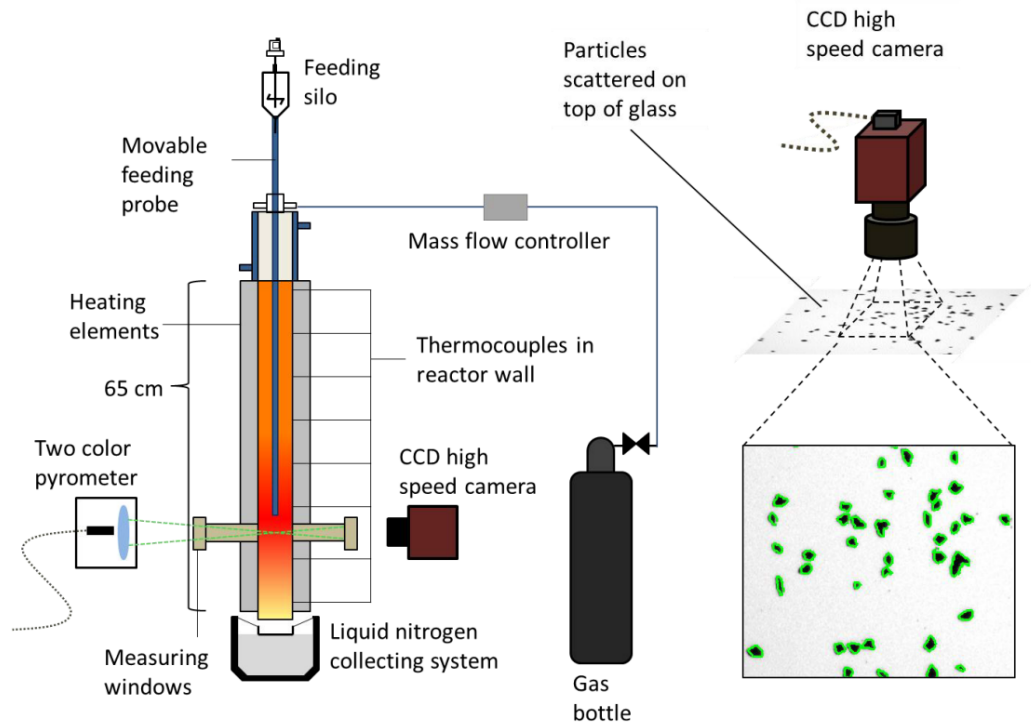
Figure 4.1 *A schematic picture of the Drop-Tube Reactor (DTR) test facility at Tampere University of Technology (TUT). The DTR consists of three modular parts: a cylindrical reactor part, a particle feeding probe, and a particle collection system. The CCD camera is used in particle velocity measurements and geometry analysis. Reprinted with permission from Elsevier Inc.*

The particle feeding probe has an inner diameter of 0.5 cm. It is cooled down by a water jacket so that the temperature inside the probe can be maintained at a temperature of less than 100 °C. This way the particle pyrolysis and combustion processes do not start before the particles enter to the heated reactor part. The particle feeding probe can be moved vertically, which enables particle drop height and residence time adjustments. The maximum and minimum particle drop-heights are 67.5 cm and 5.5 cm, respectively. The particles are fed into the feeding probe through a feeding silo, which has a screw mechanism to help in the feeding. In addition, particle carrier gas can be fed through the silo in order to push particles into the reactor.

The particle collection system consists of a collection vessel that is cooled down by liquid nitrogen. The low temperature of the vessel ensures that the combustion process stops after the particles enters to the vessel. The mass of the particles can be measured before and after they are dropped through the reactor. This way the mass loss of the particles can be measured from any drop height.

The AVT Marlin 145-B2 CCD high speed camera, shown in Fig.4.1, can take up to 10 pictures per second with a resolution of 1380x1090. The camera is used for two different purposes. Firstly, the particle velocities can be measured by taking pictures of the particles while they are dropping inside the reactor. A light pulse are shot from the opposing window to the camera, which makes two shadows of each particle into the picture. An analysis program determines the velocity of the particles based on the distance between the two shadows and on the time delay of the light pulse. Fig.4.2 shows a picture of four biomass particles dropping inside the reactor and the two shadows produced by the light pulse.
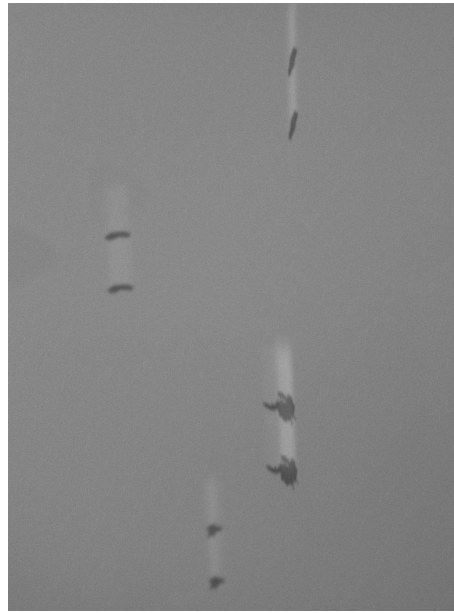
Figure 4.2 *A picture of four biomass particles dropping inside the DTR. The two shadows of each particle were produced by a light pulse that was shot from the opposing window to the camera.*

In addition to velocity measurements, the camera can be used in particle geometry analysis (see Fig.4.1). The particles can be scattered on top of a glass plate that is luminated from below. The camera is used for imaging the particles from above the glass plate and the pictures are then analyzed by a program developed by D.Sc. Markus Honkanen. The main idea of the program is to calculate spherical volume-equivalent particle diameters from the pictures. The program uses the outer line of a particle 2D projection and calculates the sphere-equivalent diameter based on the pixels inside it. The geometry analysis provides useful information on the shape and size of the biomass particles, and the sphere-equivalent diameters can be also used in the numerical modeling. More information on the experimental test facilities and previously conducted research can be found in references [28, 29, 30, 31].

4.2 Fuel Characterization

The reactivity measurements were conducted for two biomass fuels, denoted as biomass fuel 1 and biomass fuel 2. The two fuels were milled into a particle size characteristic for pulverized fuel combustion. The milled fuels were then sieved with a vibration sieve and three different size groups for both fuels were taken for further analysis:

(a) Small size fraction: sieving size of 112-125 μm,

(b) Medium size fraction: sieving size of 500-600 μm,

(c) Large size fraction: sieving size of 800-1000 μm.

The different size groups will be named B1a, B1b, B1c, B2a, B2b and B2c later in this work. B1 stands for biomass fuel 1 and B2 for biomass fuel 2, while the letters represent the size groups presented above. Three size groups were chosen so that the reactivity of different particle sizes could be analyzed. The DTR experiments were conducted for these size groups as will be described in Section 4.3.

After the vibration sieving, the particle size groups were imaged with the CCD camera. From the obtained pictures, sphere equivalent particle size distributions were determined for each size group using the geometry analysis software of D.Sc. Markus Honkanen. The size distributions are presented in Fig. 4.3. The distributions were later needed in the reactivity parameter optimization and CFD modeling.
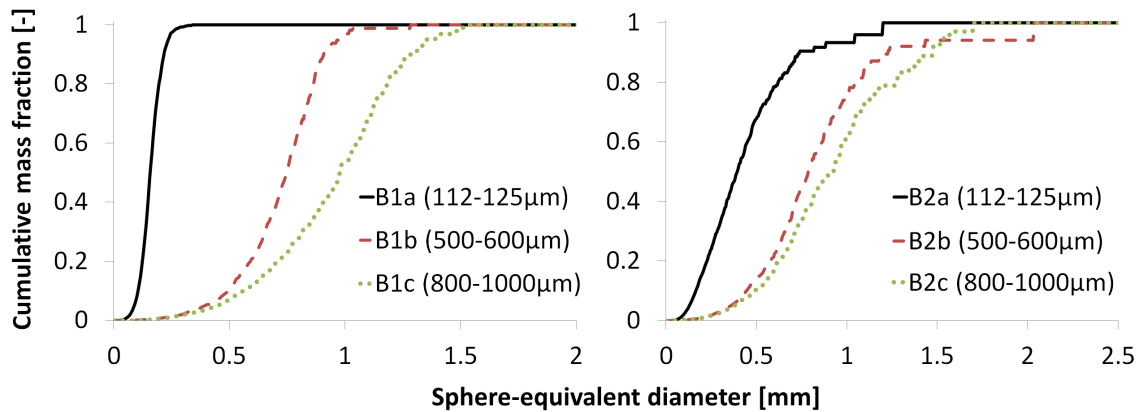
Figure 4.3 *The sphere equivalent size distributions of the three particle size groups of biomass fuel 1 and biomass fuel 2 [5].*

The geometry analysis also provided useful information on the particle shapes, aspect ratios and other particle properties. As an example, Fig. 4.4 shows two representative

particles from the medium size fraction of biomass fuel 1 and 2. The figure also demonstrates how the software recognizes the outer lines of the particles, which is essential for the sphere equivalent diameter calculations. More details about the geometry analysis can be found from the thesis of Teemu Saarinen [5].
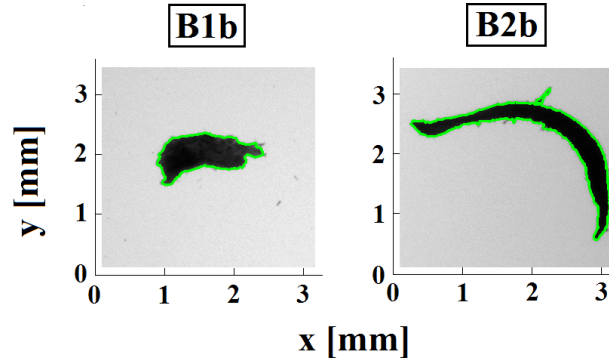
Figure 4.4 *Two representative particles from the medium size fraction (sieving size of 500-600 μm) of biomass fuel 1 and 2. The figure demonstrates how the software recognizes the outer lines of the particles, which is required for the sphere equivalent diameter calculations.*

As the particle mass affects both the combustion process and the aerodynamic behavior of the fuel particles, it is important that the spherical particles in the numerical modeling have the same mass as the real particles. In order to estimate the mass of the particles correctly, the particle densities were measured at the Laboratory of Paper Coating and Converting at Åbo Akademi University, using a mercury porosimetry. The mercury porosimetry provided the particle density as a function of external and internal pore size, allowing for the correct proportions of solid mass and air (inside the pores) to be included in the chosen density value. The accuracy of the geometry analysis program to determine the spherical volume equivalent diameters was unknown. Therefore, the limit of the pore size that determined the density had to be roughly approximated. The limiting pore size was chosen based on the resolution of the CCD camera, as it determined how accurately the geometry analysis program could recognize the outer lines of the particles. However, a more accurate way for determining the particle densities is under development. The densities and specific heats that were chosen for both fuels are shown in Table 4.1 [5].

Table 4.1 *The densities and specific heats chosen for the particle size groups [5].*

	Density [kg/m³]	Specific heat [J/kg K]
Biomass 1 (B1a, B1b, B1c)	700	1500
Biomass 2 (B2a)	600	1400
Biomass 2 (B2b, B2c)	1325	1500

As seen in Table 4.1, the density of biomass fuel 2 was measured separately for the small (B1a) and the larger (B2b, B2c) size groups. Biomass fuel 2 consisted of two visually different materials, and the measurements showed that also their densities were different. For this reason, separate values were later used in the reactivity parameter optimization and CFD modeling for the biomass fuel 2 size groups. The specific heats of the size groups were chosen based on literature [5]. Finally, both fuels were analyzed in a laboratory for obtaining the ultimate and proximate analyzes. The analyzes were obtained from commercial research laboratories which use standardized methods for the fuel compositions. The results are shown in Table 4.2.

Table 4.2 *The ultimate and proximate analyzes for biomass fuel 1 and biomass fuel 2.*

Proximate analysis	BIOMASS 1	BIOMASS 2
Total moisture [w-%]	8.2	7.5
Ash (815°C), dry [w-%]	0.83	8.0
Volatile matter, dry [w-%]	84.1	72.3
Fixed carbon, dry [w-%]	15.07	19.7
Lower heating value (LHV), dry [MJ/kg]	18.36	19.13
Ultimate analysis	**BIOMASS 1**	**BIOMASS 2**
Carbon, dry [w-%]	49.4	48.5
Hydrogen, dry [w-%]	6.2	5.8
Oxygen (calculated), dry [w-%]	43.1	36.4
Nitrogen, dry [w-%]	<0.1	1.14
Sulphur, dry [w-%]	0.013	0.12

4.3 Experimental Measurements with the DTR

This section shortly describes the experimental work conducted for the two biomass fuels. More detailed information can be found on [5]. The experimental reactivity measurements were conducted for both fuels with the three particle size groups introduced in Section 4.2. The particles were dropped through the DTR from different drop heights, so that different residence times inside the high temperature reactor could be achieved. The mass loss of the particles was measured by weighting the dropped particles before and after the experiments with each drop-height. A large number of particles were dropped in order to have a representative sample of the mass loss of each particle size group. The fuels were oven-dried before the experiments.

The particle mass loss studies were conducted in three different gas atmospheres and two different temperature levels. In total, four different tests were conducted for each particle size group:

1. Devolatilization in 600°C, 100% N_2 atmosphere
2. Devolatilization in 900°C, 100% N_2 atmosphere
3. Combined devolatilization and char burnout in 900°C, 97 vol-% N_2, 3 vol-% O_2 atmosphere
4. Combined devolatilization and char burnout in 900 °C, 79 vol-% N_2, 21 vol-% O_2 atmosphere.

The experiments 1 and 2 were used for studying the devolatilization of the fuels. The mass loss data from these experiments was used in the numerical reactivity parameter optimization for the devolatilization models (see Section 3.5.2). Two temperature levels were used to ensure that the optimized reactivity parameters work in a wide temperature range.

The experiments 3 and 4 were used for studying the particle combustion process as a whole. The mass loss data from these experiments was used in the reactivity parameter optimization for the char combustion model (see Section 3.5.2). Two different oxygen levels were used for examining how the oxygen level affects the char burnout rate. Raw fuel particles were used instead of the already formed char particles from the devolatilization experiments, because the char particles were too fragile to be used in any further experiments.

Before the DTR experiments the reactor was heated up to the wanted temperature level, and the reactor wall temperature was recorded at the 8 measurement points at the wall. After changing the drop height of the particles, the wall temperature profile was adjusted to be similar with the other experiments. After this, a thermocouple was used for measuring the reactor center line temperature at different vertical positions after the feeding probe outlet (see Fig. 4.1 for clarity). The center line temperature was measured in order to have information on the gas temperature surrounding the dropping particles. The gas temperature was needed for calculating the convective heat transfer on the particles in the reactivity parameter optimization.

An example of the wall temperature and thermocouple measurements can be seen in Fig. 4.5. The temperatures were measured and recorded this way for all different particle drop heights in each experiment, as the measurements were later used in the reactivity parameter optimization and CFD modeling. In Fig. 4.5, the first thermocouple measurements are just from the feeding probe outlet position. The thermocouple measurements show a significantly lower temperature compared to the wall at this position, because the feeding probe was kept in a low temperature with the water cooling.
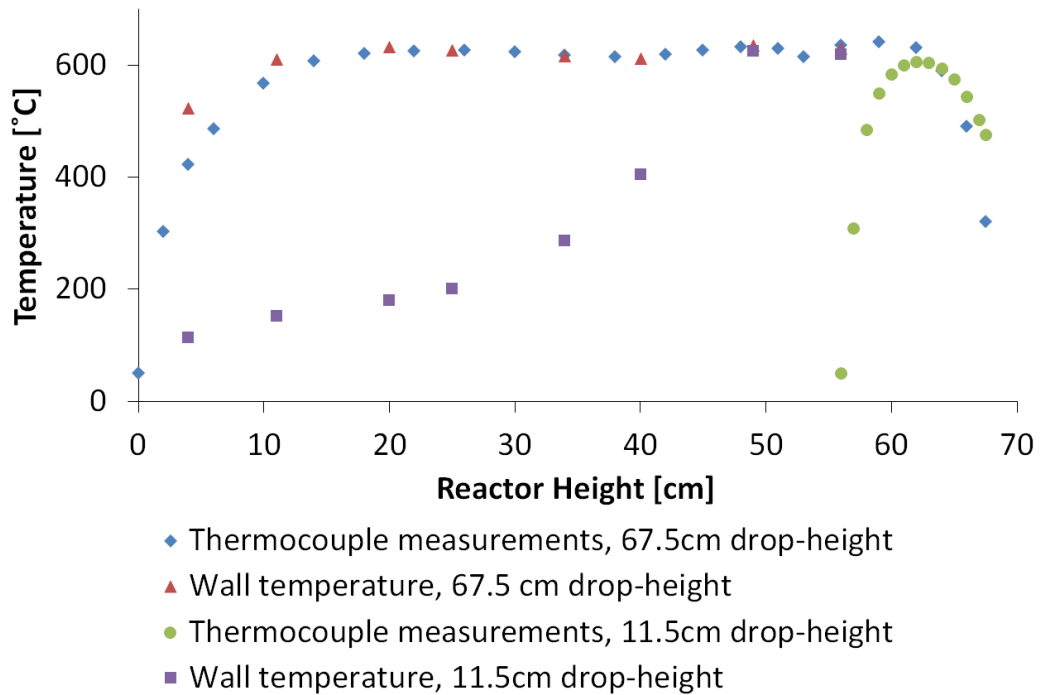
Figure 4.5 *The measured wall and center line temperatures of the DTR for the full drop height of 67.5 cm and for a lower drop height of 11.5 cm in 600°C devolatilization experiments. Reactor height at 0 cm denotes the reactor top (gas inlet plane), while the reactor outlet locates at 67.5 cm. [5]*

In all experiments, the primary gas mass flow rate was adjusted so that the volume flow (velocity) in a fully-developed pipe flow was the same independently of the temperature level and gas atmosphere. The aim was that the particle residence times would stay as same as possible in all experiments. Furthermore, the Reynolds number was kept fairly in the laminar regime. The mass flow rate of the carrier gas was kept constant, as it was so small that it was not meaningful to adjust it.

The final measurements were conducted for the particle velocities. The velocities were needed for determining the residence times of the particles inside the reactor and for obtaining the particle velocity profiles for the reactivity parameter optimization. The velocity measurements were conducted separately for all different particle size groups using the CCD camera and analysis program (see section 4.1). A large number of dropping particles from each size group were pictured from different particle drop heights, and the data was then used for calculating the mean velocity of the size group for each height. For example for the smallest particle size group of biomass fuel 1 (B1a), 2799 particles were detected in the CCD camera pictures from the 25.5 cm drop height in the experiment 1.

The average value of these velocity samples was then used for calculating the mean particle velocity of B1a at a distance of 11.5 cm after the particle feeding probe outlet (in 25.5 cm drop height the center point of the window pipes was 11.5 cm below the feeding probe outlet). The results for the particle velocity measurements are presented in Section 6.3.

5. REACTIVITY PARAMETER OPTIMIZATION

5.1 Fuel Treatment in Numerical Modeling

As discussed in Section 4.2, both fuels (B1, B2) were divided into three size groups (a, b, c) for the experimental mass loss studies and the size distributions were measured for each group (see Fig.4.3). In the numerical modeling, the size distributions were discretized into 10 size classes each containing 10% of the total particle volume. This means that the smallest size class accounted for 10% of the total particle volume, the second smallest accounted for another 10% and so on. Furthermore, a volume-mean particle diameter was calculated for each size class. The idea is presented in Fig. 5.1.
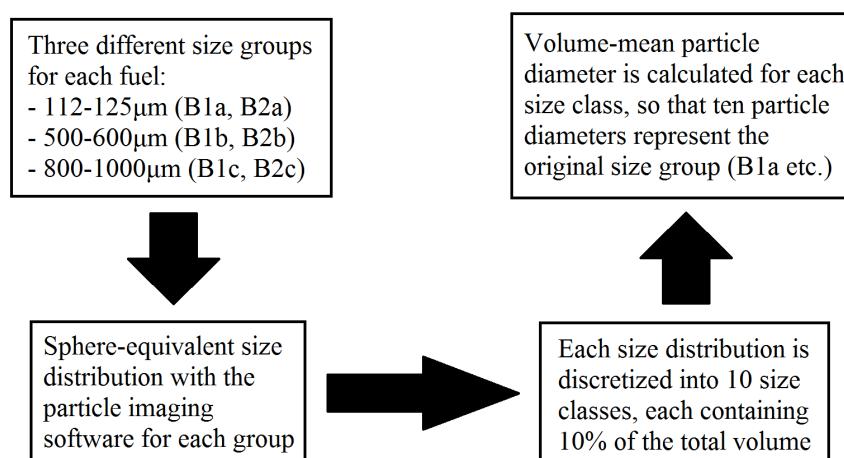
Figure 5.1 *In the numerical modeling, ten spherical particles having different diameters represent each particle size group of different sieving size.*

The volume-mean diameters of the 10 particle size classes are presented in Table 5.1. As discussed in Section 4.2, the density of the particles was measured with a mercury porosimeter and the goal was to determine the particle density so that the spherical particles would have the same solid mass as the real irregular biomass particles. This way the volume-mean particles presented in Table 5.1 would also represent the mass-mean particles of the different size classes.

Table 5.1 *The volume-mean diameters for the different particle size classes.*

	B1a, diameter [μm]	B1b, diameter [μm]	B1c, diameter [μm]	B2a, diameter [μm]	B2b, diameter [μm]	B2c, diameter [μm]
Particle 1	93.1	398	445	133	364	378
Particle 2	120	547	649	200	519	579
Particle 3	136	633	771	260	625	683
Particle 4	147	684	871	315	700	767
Particle 5	157	728	962	369	753	854
Particle 6	168	766	1021	426	820	960
Particle 7	178	807	1087	482	895	1032
Particle 8	192	849	1140	574	995	1141
Particle 9	211	880	1235	680	1121	1380
Particle 10	241	969	1358	1049	1437	1522

The spherical particles of Table 5.1 were used in the the reactivity parameter optimization and CFD modeling. The material properties of the fuels were presented in Section 4.2.

5.2   Reactivity Parameter Optimization Procedure

The apparent reactivity parameters for the two fuels were optimized for two different devolatilization models and for one char combustion model using the optimization tools in MATLAB R2015a [4]. The particles were treated in the same manner as in the commercial CFD software ANSYS Fluent [6]. This means that the mass loss during the combustion process was calculated using the same equations and assumptions that were presented in Section 3.5. This ensured that the optimized reactivity parameters were directly utilizable in Fluent calculations. The basic idea of the optimization procedure will be introduced in this section and more detailed information can be found from the M.Sc. thesis of Teemu Saarinen [5].

In the reactivity parameter optimization, the particle mass loss inside the DTR was calculated using either the Single Kinetic Rate model or the Two Combeting-Rates model for the devolatilization stage, and the Kinetics/Diffusion-Limited Rate model for the char burnout stage (see Section 3.5.2). The apparent reactivity parameters, namely, the model activation energies and pre-exponential factors, were optimized separately for the different particle size groups. Each particle size group was described by ten particles of different size, as described in the previous section. The goal of the optimization was to find reactivity parameters that describe the experimentally determined mass loss.

The real biomass particles were highly non-spherical and belonged mostly in the size range of thermally thick particles (see Section 2.3). However, in the numerical modeling the particles were assumed spherical and isothermal. For this reason, the particle temperature histories are not expected to be realistic. The idea of the apparent reactivity parameter optimization was to determine the model parameters in a way that the spherical particles lose their mass at the same rate as the real biomass particles. Therefore, the reactivity parameters can describe the mass loss of the real particles despite of the unrealistic temperature histories. The spherical particle diameters were constructed in a way that they describe the real mass of the biomass particles, and the external flow and temperature conditions were kept as realistic as possible in the numerical modeling. This strategy can possibly work in biomass combustion modeling even though the particle shapes and temperatures are not realistically covered, as the most crucial thing for the CFD modeling is to correctly predict the mass loss of the particles in certain external conditions.

For demonstration purposes, the optimized particle conversion curves during devolatilization of the particle size group B1a are shown in Fig. 5.2. The figure was obtained from the MATLAB software after the parameter fitting had finished, and it was obtained using the Single Kinetic Rate model [5]. The lower and upper curves in the figure represent the conversion of the size group in the 600°C and 900°C temperature levels, respectively. The thin curves represent the conversion curves of the ten particle sizes (see Table 5.1) describing this particular size group. The thick curves are the average values of the ten size classes in each temperature level. The points represent the experimental mass loss from the DTR measurements at the corresponding temperature levels. The goal of the reactivity parameter optimization was to fit the average mass loss curves (thick curves) to the experimental data in a best possible way in the model limits.

Fig. 5.2 immediately demonstrates a limitation in the modeling assumptions. The final volatile yield the particles have to achieve is a predetermined constant (95% of the dry weight for this size group). However, as seen in the experimental measurements, the final volatile yield does not approach this limit in the lower 600°C temperature level. This is consistent with the existing literature, as the lower heating rate results in a lower volatile yield and higher char yield after devolatilization. As the volatile yield is a predetermined contant in the modeling, the particles have to reach this level independently of the temperature level. In combustion modeling, however, this is probably not a significant drawback because the particles will always experience rather high heating rates, and therefore it is more crucial to have the higher temperature level correctly predicted.

• Experiments in 600°C
• Experiments in 900°C
Solid lines: Modeled particle conversion curves
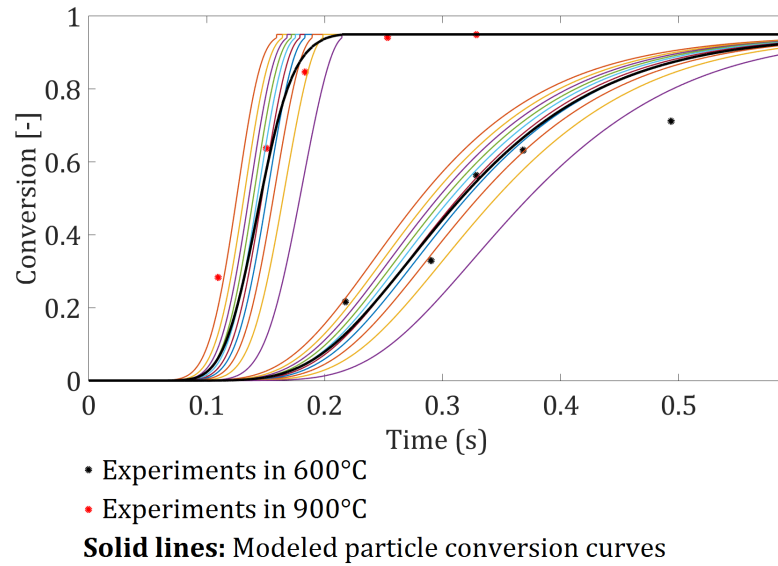
Figure 5.2 *A figure demonstrating the idea of the parameter optimization procedure. [5]*

In the MATLAB modeling, the conversion curves could be rather well fitted to the experimental data, as Fig. 5.2 demonstrates. The next section will present the CFD model of the DTR, which was used to verify that the reactivity parameters also function in the full CFD model.

6. CFD MODEL OF THE DTR

This chapter introduces the CFD model of the DTR. The modeling was conducted with the commercial CFD software ANSYS Fluent (versions 14.5 and 16.1) [6]. The computational meshes were created with the ICEM CFD 14.5 software of ANSYS. The meshes were three-dimensional and contained only hexahedral elements.

The modeling was started with a simplified model, which did not include the measurement window pipes at the lower end of the reactor (see Fig. 4.1). A model of the thermocouple used in the measurements was included in these simulations. This was done because the thermocouple did not have a radiation cover in the measurements, and therefore it expectedly showed an inaccurate gas temperature at the center line of the reactor. However, the temperature was needed in the reactivity parameter optimization in MATLAB for the particle temperature history calculations. Thus, the goal of the thermocouple simulations was to obtain more accurate information on the center line gas temperature, and at the same time to validate the temperature field of the simulation. The thermocouple modeling is presented in Section 6.1.

After the temperature field validation, the DTR was modeled with the same setup as in the particle mass loss experiments (see Section 4.3), using the same gas atmospheres and temperature levels. The calculated gas velocity was compared with the particle velocity measurements, in order to ensure that the the two were in line, i.e. if the profiles were similar and the simulation results in the correct velocity range. After this, it was meaningful to continue towards particle combustion modeling with the Discrete Phase Model (DPM).

Furthermore, the shape factor needed for the particle drag force calculations (see Section 4.3) was adjusted so that the numerical and experimental particle velocities were comparable. The drag force had a major effect on the particle residence times inside the reactor. As an example, biomass fuel 2 particle with a diameter of 500 µm had residence times of 2.7 s and 6.6 s during a 3 m drop distance with the spherical and non-spherical drag law, respectively. Therefore a great care was taken in choosing the drag law and

adjusting the shape factor for the particles. The shape factor adjustment is presented in Section 6.3.

The aim of the temperature and flow field validations, and shape factor adjustment, was to ensure that the particle residence times and temperature histories were accurately calculated. This way the functioning of the optimized reactivity parameters could be analyzed without other affecting factors. Finally, the DTR model was used for calculating the particle conversion curves (mass loss as a function of residence time or path length) with the optimized reactivity parameters. This verified that the reactivity parameters from MATLAB optimization work correctly also in the CFD environment. The conversion curves were compared with the experimental mass loss data and the final conclusions on the functioning of the parameters were made. The results are presented in Section 6.4.

6.1 Temperature Field Validation

6.1.1 Calculation Methods for Thermocouple Simulations

The temperature field of the DTR simulations was validated by comparing the calculated thermocouple temperatures with the experimental thermocouple measurements. The solid thermocouple was included in the CFD model and its temperature was calculated together with the fluid flow. The calculated temperature at the thermocouple probe tip (at the point where the thermocouple junction is welded together with the stainless steel sheath, see Fig. 6.3) was then compared with the real thermocouple measurements.

The boundaries of the calculation domain are shown in Fig. 6.1. The calculations were made in three dimensions and only a cross section of the domain is shown in the figure. During the thermocouple measurements, the particle feeding silo was detached from the reactor and the thermocouple was inserted into the reactor through the particle feeding probe inlet. This position, the reactor top plane at x = 0 cm, was chosen as the upper boundary of the domain. The lower boundary was chosen as the reactor outlet, at position of x = 67.5 cm below the reactor top. The simulations were representative to the 600°C devolatilization experiments, where the particle feeding probe outlet was at a position of x = 48 cm below the reactor top. Because the thermocouple measurements were conducted for multiple center line positions inside the DTR, a new mesh had to be created for each case. In the studied cases, the thermocouple probe tip was at the positions of x = 48 cm, 49 cm, 50 cm, 51 cm, 53 cm, 55 cm, 59 cm, 63 cm, 65 cm and 67 cm below the reactor top.
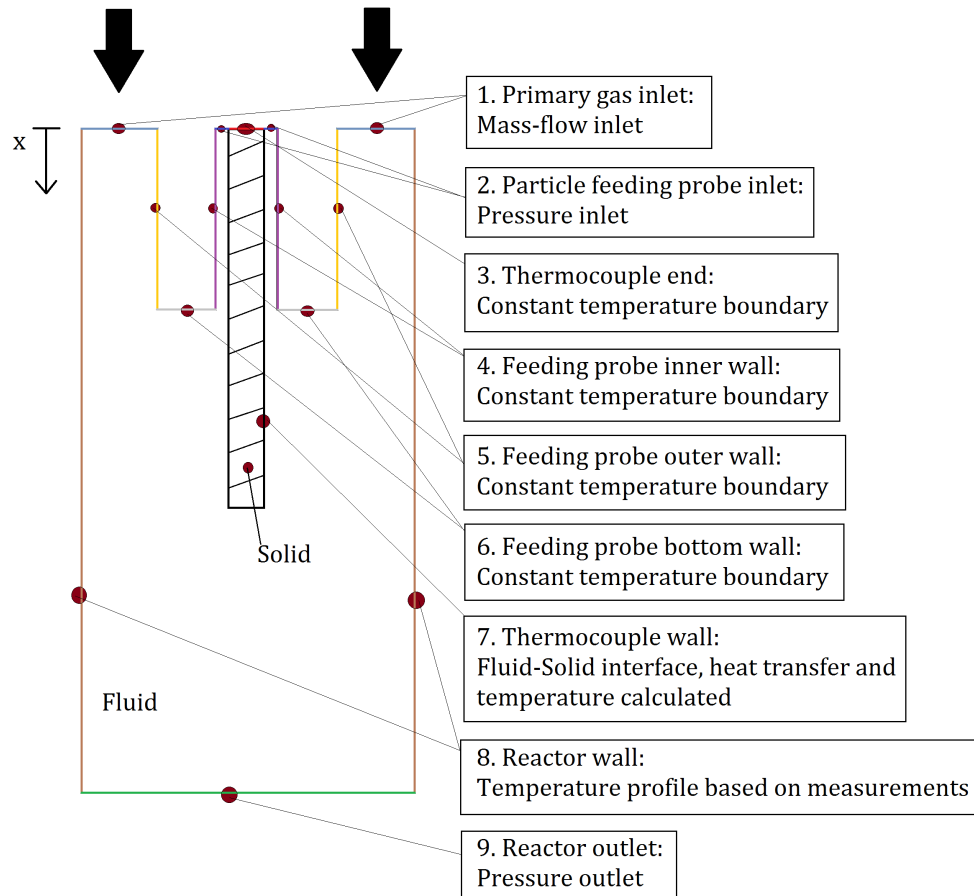
Figure 6.1 *A schematic figure of a cross section of the computational domain used for the thermo-couple measurement modeling.*

The boundary conditions for each boundary shown in Fig. 6.1 are presented in Table 6.1 and Fig. 6.2. As seen in Fig.6.2, the reactor wall reaches the maximum temperature at the feeding probe outlet position (x = 48 cm). The temperature at the end of the reactor falls rapidly, because there were no heating elements at that part of the reactor. As there were no temperature measurements from the end, the wall boundary profile was adjusted so that the thermocouple results matched with the experimental values also at the reactor end.

A schematic figure of the thermocouple is presented in Fig. 6.3. The thermocouple probe was cylindrical having an outer diameter of 0.5 cm. It consisted of an insulation material that was covered by a thin sheath of stainless steel at the outer surface. The thickness of the stainless steel sheath was unknown and a thickness of 0.5 mm was used in the simulations.

Table 6.1 Boundary conditions used in the thermocouple simulations.

Boundary name	Type	Value
1. Primary gas inlet	Mass-flow inlet	2 L/min (STP) of N_2, $T_{in} = 25$ °C
2. Particle feeding probe inlet	Pressure inlet	101325 Pa
3. Thermocouple end	Constant temperature	40°C
4. Feeding probe inner wall	Constant temperature	40°C
5. Feeding probe outer wall	Constant temperature	80°C
6. Feeding probe bottom wall	Constant temperature	90°C
8. Reactor wall	UDF temperature profile	See Fig. 6.2
9. Reactor outlet	Pressure outlet	101325 Pa
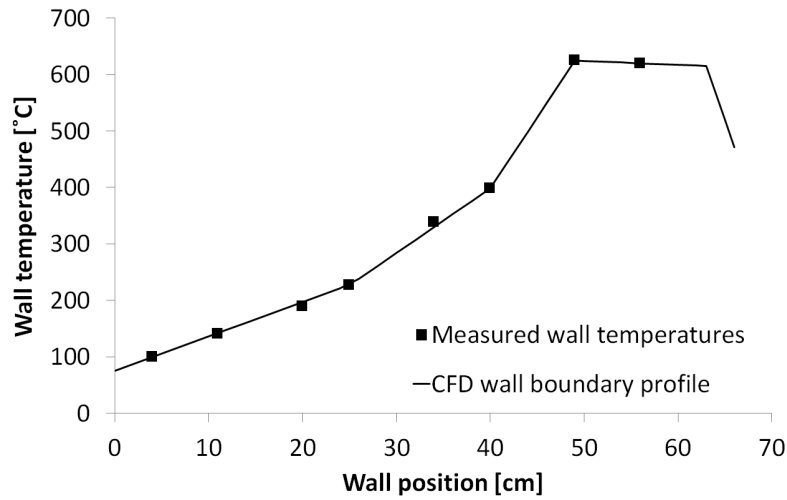
Figure 6.2 Reactor wall temperature profile used in the DTR simulations with the thermocouple, shown together with the measured wall temperatures.

The material properties of the thermocouple are presented in Table 6.2. The properties of the insulation material were chosen based on magnesium oxide, which is a common insulation material used in thermocouples. The thermal properties of the stainless steel were chosen based on the AISI 304 type of steel. An emissivity of 0.5 was used for the steel surface, as the thermocouple surface was covered by soot. The insulation material did not participate in radiation, because the steel sheath was modeled as an opaque surface. Sensitivity of the results on the material properties was studied by varying the thermal properties of the insulation material, and trying properties of different steel types for the stainless steel sheath. The changes did not significantly affect the results.
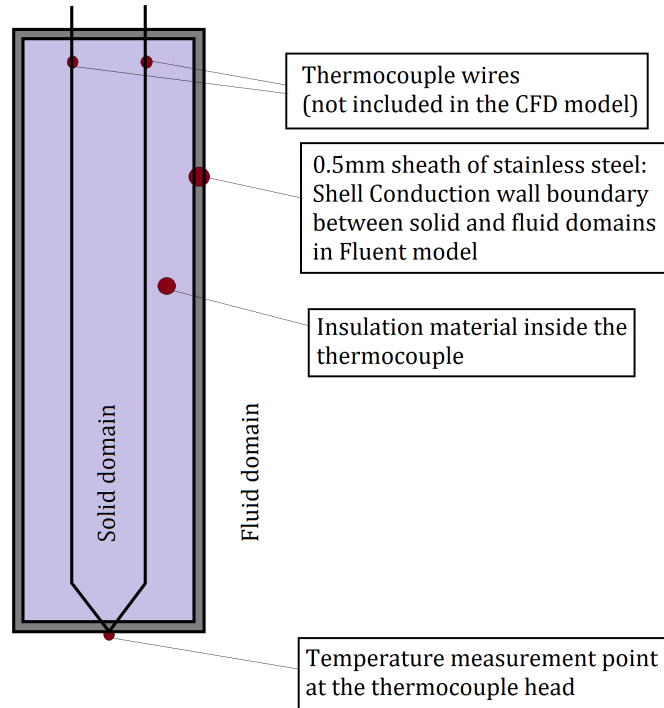
Figure 6.3 *A schematic figure of a cross section of the thermocouple used in the thermocouple simulations.*

The heat transfer through the stainless steel layer was calculated with the Shell Conduction model of ANSYS Fluent (see Fluent theory guide [6]). The Shell Conduction model enables heat transfer calculations in both planar and perpendicular directions of a wall having a certain thickness. This way the stainless steel layer could be modeled with a wall boundary between the solid and fluid domains and only the insulation material of the probe had to be meshed in the solid domain. The final computational meshes consisted of approximately 500 000 hexahedral cells. The surface mesh of the whole calculation domain is shown in Fig. 6.4.

Table 6.2 *Material properties used for the thermocouple sheath and insulation. Specific heat of the insulation was approximated as close to the value of air, other properties from reference [32].*

	Insulation (MgO)	Stainless steel (AISI 304)
Density [kg/m³]	270	7900
Specific heat [J/kg K]	1000	611
Thermal conductivity [W/m K]	0.082	15
Emissivity [-]	-	0.5

The calculations were conducted with the Pressure-Based Steady Solver of ANSYS Fluent 14.5, using the laminar flow equations. The steady state simulation represents the case where the thermocouple probe had been inside the reactor until the measurement had reached a constant value. This was also the case with the real measurement values. The material properties of nitrogen were calculated with the temperature dependent polynomial fits available in Fluent database. The pressure and velocity were coupled with the SIMPLE algorithm, and the pressure was discretized using the PRESTO! scheme. The radiation was modeled with the Discrete Ordinates (DO) model and discretized with the Second Order Upwind scheme. Momentum and energy equations were discretized using the same scheme.
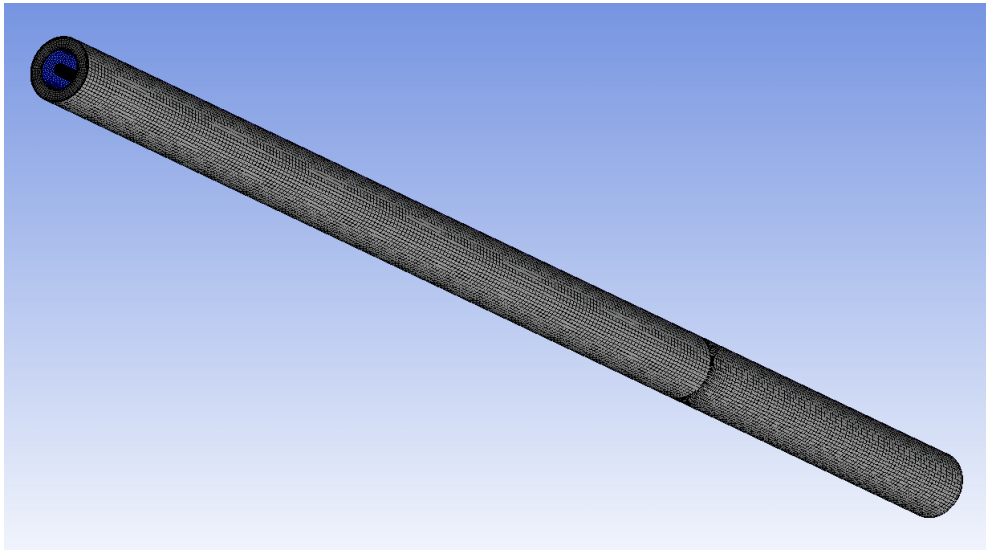
Figure 6.4 *Surface mesh of the computational domain in the thermocouple simulations.*

6.1.2   Results for Thermocouple Simulations

The calculated thermocouple probe temperatures and measurements are compared in Fig. 6.5. The figure also presents the calculated gas temperature at the reactor center line in the normal operational case without thermocouple, which is presented in more detail in Section 6.2.

The calculated thermocouple temperatures match very well with the measurements, as seen in Fig. 6.5. At the first temperature measurement point, the thermocouple probe tip was positioned just at the particle feeding probe outlet (x = 48 cm). At this position the reactor wall temperature had reached the maximum of 600°C (see Fig. 6.2), but the

thermocouple shows a much lower value because it is entirely inside the water cooled particle feeding probe. The gas temperature at the center line rises slowly and reaches the maximum temperature at approximately x = 64 cm below the reactor top. The calculated thermocouple values at positions x = 53 cm and 55 cm show a small deviation compared to the measurements. This is the position of the measurement windows (not included in the simulations), which explains the deviations.

♦ Thermocouple measurements at different depths inside the reactor
■ CFD: Thermocouple tip temperature at different depths inside the reactor
— CFD: Gas temperature at the centerline of the reactor
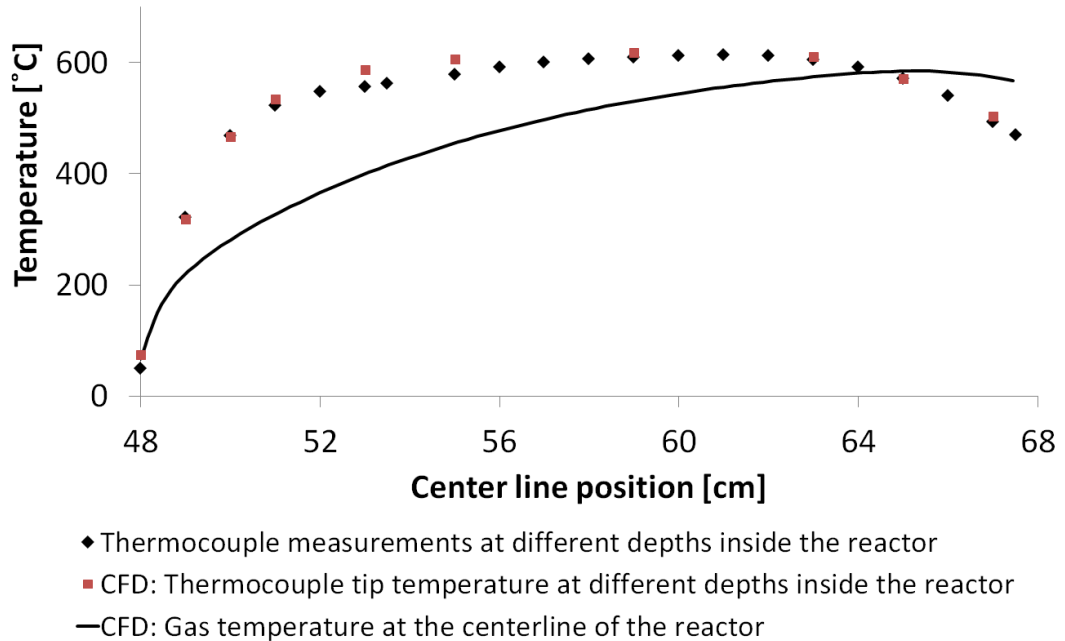
Figure 6.5 The thermocouple measurements at the center line of the DTR shown together with the calculated thermocouple and gas temperatures. The measurements and simulations were conducted for the case where the particle feeding probe was at x = 48 cm below the reactor top, and the reactor wall was heated to 600°C in pure N_2 atmosphere.

Compared to the gas temperature, the thermocouple measurements show a higher temperature in all positions except at the end of the reactor, where the wall temperature begins to fall (see Fig. 6.2). The thermocouple measurements deviate from the gas temperature, because the radiation from the walls effectively heats the thermocouple probe inside the reactor. The gas temperature rises more slowly at the center line, because the oxygen and nitrogen gases do not absorb the heat from radiation.

Temperature contours in a cross section of the DTR for three different simulation cases are shown in Fig. 6.6. The thermocouple tip positions from left to right are 50 cm, 63 cm and 67 cm from the reactor top, respectively. In the left contour, the thermocouple temperature is higher than the surrounding gas temperature, because it is heated up by radiation from the reactor walls. In the right contour, the thermocouple tip is at a lower

temperature than the surrounding gas, as heat is lost in radiation to the reactor outlet and wall. The figure demonstrates how the thermocouple temperature reflects more of the wall temperature than the surrounding gas temperature.
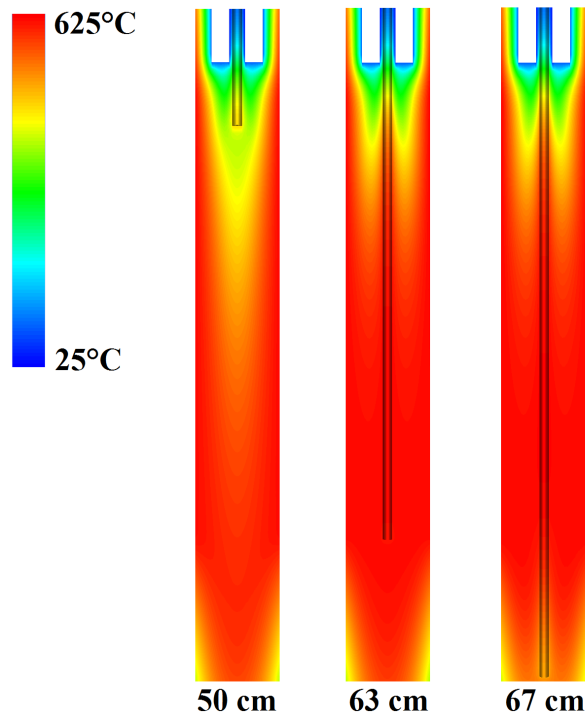
Figure 6.6 *Temperature contours in a cross section of the DTR for three simulation cases where the thermocouple is at different depth inside the reactor. The thermocouple tip positions from left to right are 50 cm, 63 cm and 67 cm from the reactor top, respectively.*

As a conclusion, the results indicate that the temperature field of the DTR is accurately captured in the simulation, and the CFD model can be further used in the particle combustion modeling. The simulations show clearly how the thermocouple measurements did not give the correct gas temperature at the center line of the reactor, and therefore the gas temperature obtained from the CFD simulations was used in the reactivity parameter optimization with MATLAB.

6.2 Flow Field Validation

6.2.1 Calculation Methods for Flow Field Simulations

The biomass particles were dropped through the reactor as single particles and thus they had an insignificant effect on the flow field inside the DTR. The CFD models presented in

this section were also used for the particle mass loss studies, because the particle modeling could be conducted as a postprocessing step after the flow and temperature fields of the reactor had been validated. This approach represents the one-way coupling discussed in Section 3.5. The flow field results were validated by comparing the simulated gas velocity to the measured particle velocities. The primary simulations were conducted without the window pipes at the lower end of the reactor, but the pipes were later added in order to analyze their effect on the flow field. The surface mesh of the DTR including the window pipes is shown in Fig. 6.7. Multiple simulations were conducted having the particle feeding probe at different depth inside the reactor.
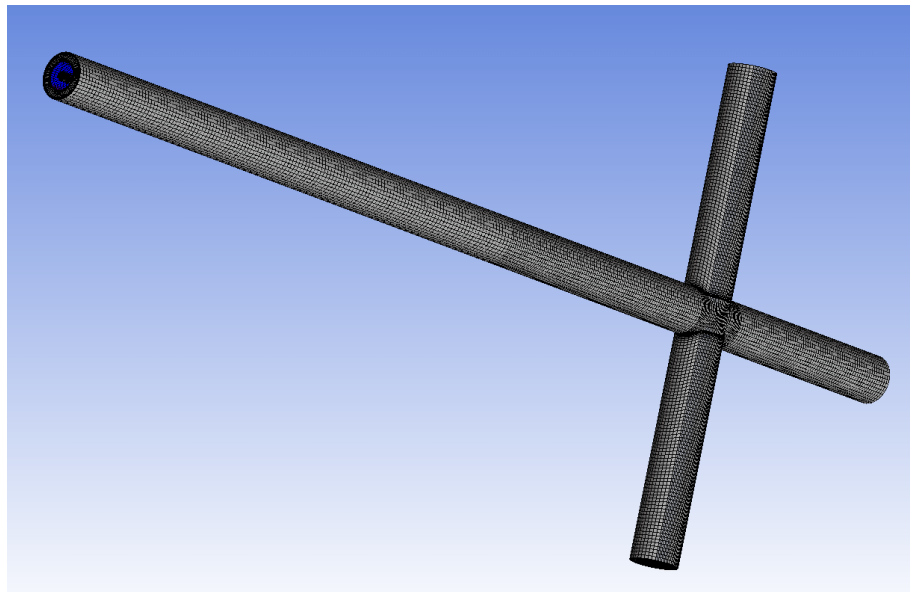
Figure 6.7 *The surface mesh of the computational fluid domain of the DTR.*

The boundaries of the calculation domain are shown in Fig. 6.8. The calculations were conducted in three dimensions and only a cross section of the domain is shown. The boundary conditions for each boundary are shown in Table 6.3.

The mass flow rate for the primary gas was adjusted separately for the different gas atmospheres and temperature levels, as discussed in Section 4.3. The mass flow rate was based on the average velocity in a fully developed pipe flow, aiming to keep the velocity same for all gas atmospheres and wall temperatures. This way the particle residence times would be comparable in all experiments. The reactor wall temperature profiles were constructed based on the experimental data, in the same manner as presented in Fig. 6.2. The calculations used the same discretization schemes and solver settings as the thermocouple simulations, and the gas properties were calculated with the temperature dependent polynomial fits available in Fluent database.
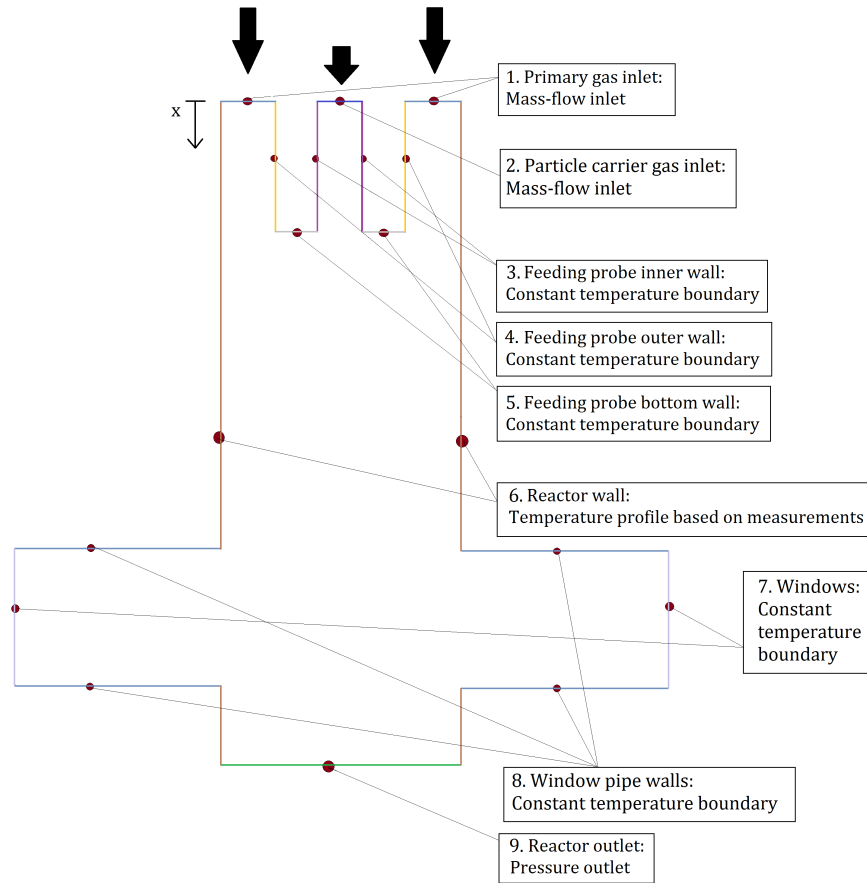
Figure 6.8 *A schematic figure of a cross section of the computational domain used for the flow field validation and particle combustion modeling.*

Table 6.3 *Boundary conditions used in the DTR simulations and particle combustion modeling.*

Boundary name	Type	Value
1. Primary gas inlet	Mass-flow inlet	Variable mass flow rates depending on the gas atmosphere and wall temperature, $T_{in} = 25$ °C
2. Particle carrier gas inlet	Mass-flow inlet	0.64 L/min (STP) of N_2, $T_{in} = 25$ °C
3. Feeding probe inner wall	Constant temperature	40°C
4. Feeding probe outer wall	Constant temperature	80°C
5. Feeding probe bottom wall	Constant temperature	90°C
6. Reactor wall	UDF temperature profile	See Fig. 6.2
7. Windows	Constant temperature	100°C
8. Window pipe walls	Constant temperature	500°C ($T_{wall} = 600$°C), 800°C ($T_{wall} = 900$°C)
9. Reactor outlet	Pressure outlet	101325 Pa

6.2.2   Results for Flow Field Simulations

The calculated gas velocity at the center line of the reactor and the particle velocity measurements are presented in Fig. 6.9. The particle velocity measurements are those of the smallest size group of biomass fuel 1 (B1a). The smallest group was chosen because the small particles follow the gas movements more effectively than the larger particles.

Fig. 6.9 indicates that the slip velocity between the gas and the particles remains almost constant throughout the particle falling inside the reactor. In addition, the particles and the gas have a very similar shape in their velocity profiles. The gas accelerates rapidly after the flow enters the heated reactor part, because it expands due to heat. The acceleration can be observed also in the particle velocity measurements, as the particles speed up right after coming out from the feeding probe. These observations indicate that the flow field in the DTR simulations is accurately modeled.
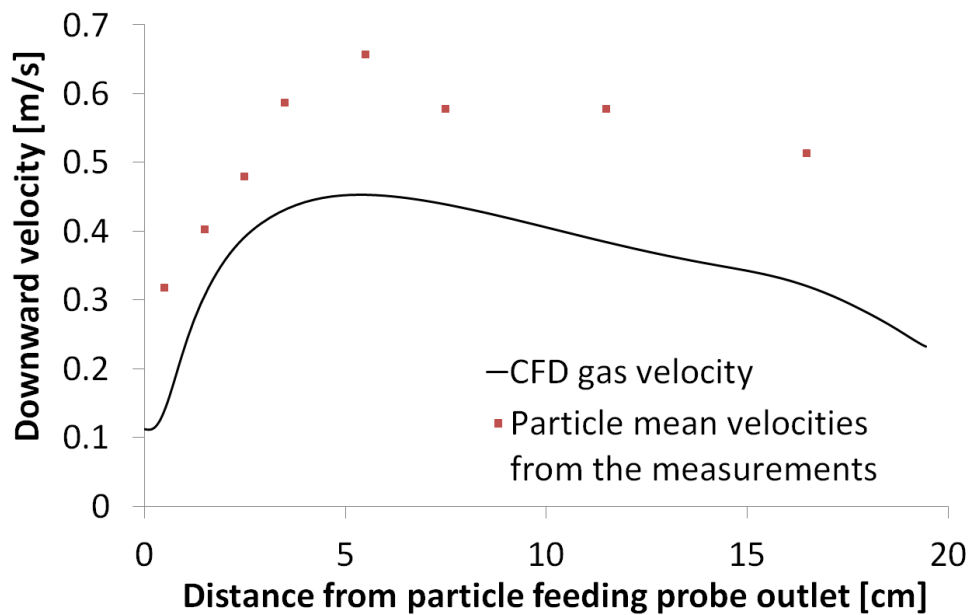
Figure 6.9 *The computed gas velocity at the center line of the reactor and the particle mean velocities (B1a) measured with the CCD camera. The calculations and measurements were conducted with the 600°C wall temperature and pure N_2 atmosphere.*

6.3 Particle Shape Factor Determination

The calculated velocity profiles for the size group B1a are presented together with the measurements in Fig. 6.10. The thin curves in the figure present the velocities of the ten particle size classes introduced in Table 5.1. The uppermost curve is the velocity of the largest particle in the size group, while the curve at the bottom is the smallest one. The thick curve presents the average velocity of these size classes. As was discussed in Section 4.3, the experimental mean velocities were obtained by averaging a large number of velocity samples from the size group. Therefore, the particle velocity measurements in Fig. 6.10 represent the average velocities of all particles belonging in size group B1a. For this reason, the average velocity of the ten particle size classes, the thick curve, is the velocity profile that should be compared with the measurements.
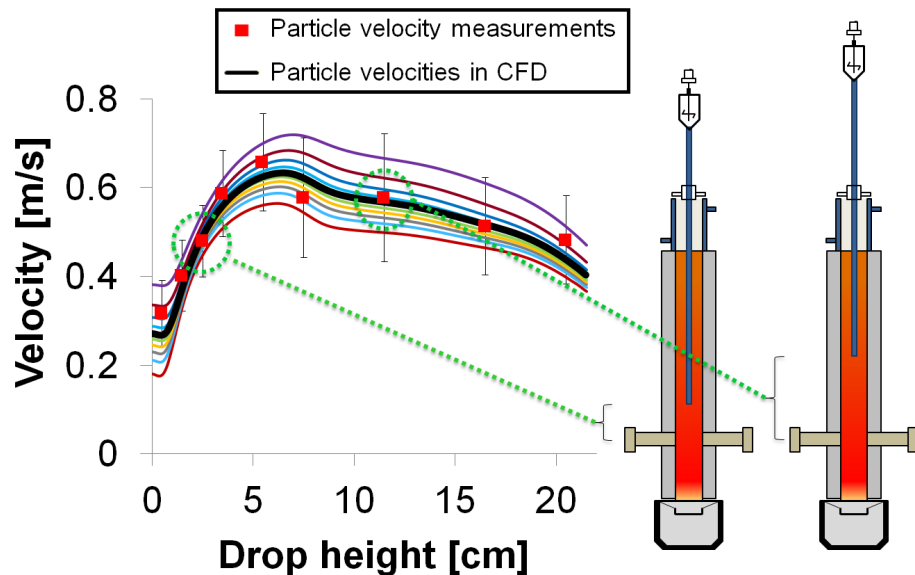
Figure 6.10 *Calculated particle velocity profiles for the ten size classes of B1a, and the mean particle velocities obtained from the measurements. The error bars show the standard deviation of the measured mean values. The thin curves represent the ten size classes of B1a introduced in Table 5.1, while the thick curve presents their average. The simulation and measurements were conducted for the 600°C wall temperature and pure N$_2$ atmosphere.*

The simulation and experiments of Fig. 6.10 were conducted in the 600°C wall temperature and pure N$_2$ atmosphere. In each experiment, the particles were dropped from a different height relative to the measurement window, and this way one experimental point in Fig. 6.10 was obtained. In contrast, the simulated particle velocity profiles were obtained by injecting particles into the reactor from one single drop height, where the feeding probe outlet was at x = 46 cm below the reactor top. Simulations from different

particle drop heights indicated that the particle velocity profiles did not change significantly when the feeding probe was moved inside the reactor. For this reason, the modeled velocity profiles from any single drop-height could be reasonably well compared with the experimental velocities.

Because the real biomass particles were highly non-spherical, the non-spherical drag law (see Section 3.5.1) was used for calculating the particle drag force during their fall inside the reactor. The drag force had a major effect on the particle velocities and therefore the shape factor required for its calculation was carefully determined. Additional simulations indicated that the particle velocities could not go through the measurements if, for example, the spherical drag law was used. As an example, biomass fuel 2 particle with a diameter of 500 µm had residence times of 2.7 s and 6.6 s during a 3 m drop distance with the spherical and non-spherical drag law, respectively. Another factor that highly affected the particle velocities was the density. The densities for the different particle size groups were already determined during the work of Teemu Saarinen [5] and therefore the only option to adjust the particle velocities to match with the measurements, was the shape factor of the non-spherical drag law. The additional factors affecting the particle velocities were the mass loss rate of the particles, i.e. the reactivity parameters, and the swelling coefficient. These factors, however, had only a minor effect on the profile shape after the particles started to lose their mass in devolatilization and char burnout.

Fig. 6.10 presents the calculated velocity profiles and measurements for all particle size groups. The calculations were made using the optimized reactivity parameters and the densities determined in the work of Teemu Saarinen [5]. In case of biomass fuel 1, the shape factor value was chosen as $SF = 0.25$ for all particle size groups, and a value of 0.1 was used for the biomass fuel 2 groups. These values were approximately two times smaller the values calculated from Eq. (3.17).

Fig. 6.10 shows that the velocity profiles match relatively well with the experimental measurements. However, the following points will be further discussed:

1. The shape factor values that were used, were smaller than the values calculated from Eq. (3.17).
2. Some of the calculated mean velocities deviate significantly from the velocity measurements, especially with the size groups B1b, B1c, B2a.
3. The ten size classes have substantially different velocity profiles within all size groups except B1a.
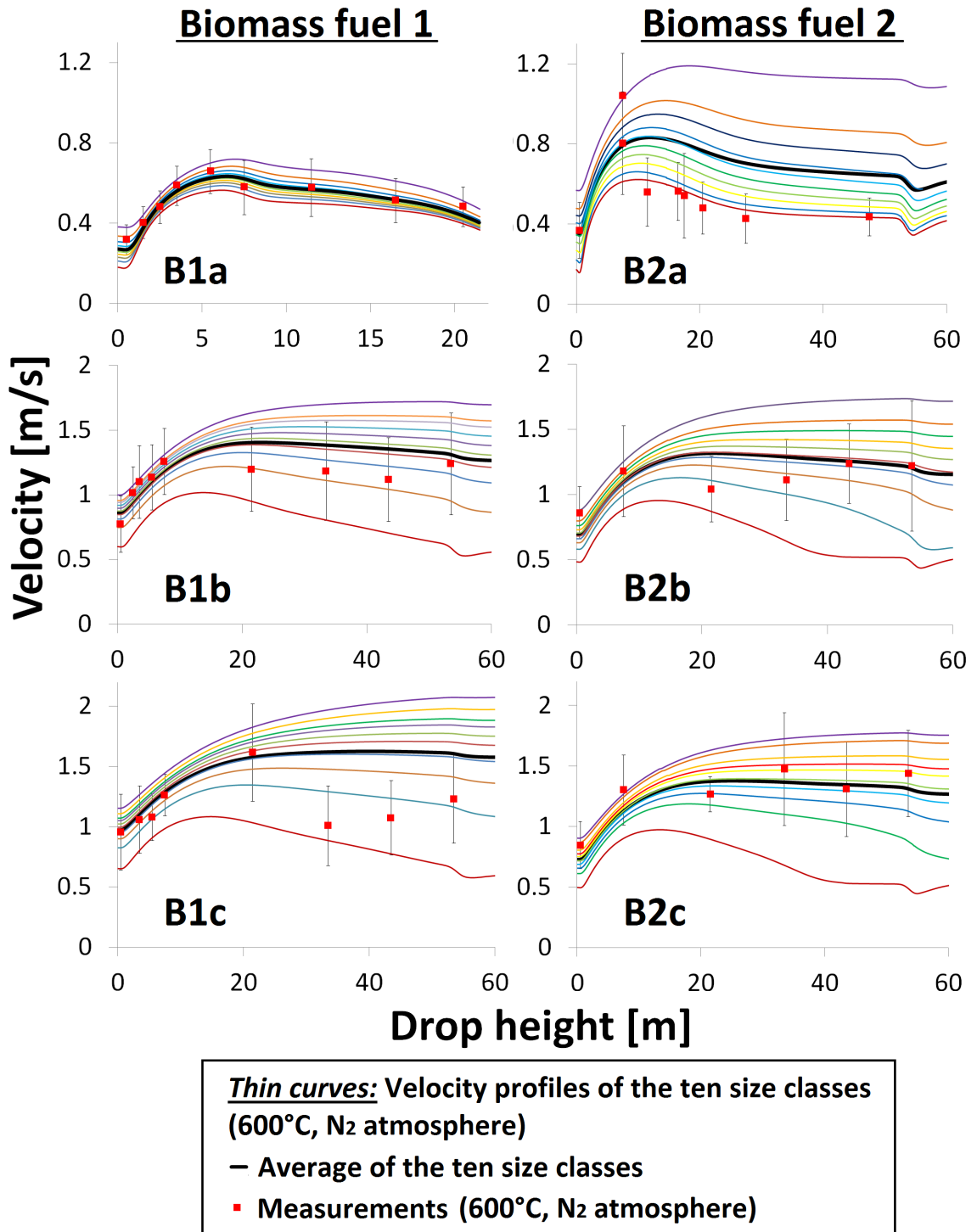
Figure 6.11 *The calculated velocity profiles and measurements for all particle size groups in the 600°C wall temperature and pure N_2 atmosphere. The thin curves present the velocity profiles of the ten size classes of Table 5.1, while the thick curve is their average. The standard deviation of the measurements is presented with the error bars.*

The explanation for the low shape factor values could be that the chosen particle densities were too high, because with a lower density the velocity profiles would go through the measurements using the theoretical value from Eq. (3.17). On the other hand, Eq. (3.17) is probably too simplified to give correct value for the shape factor as it assumes that the particles are smooth cylinders, which is a rough approximation compared to the particles shown in Fig. 4.4. If the shape factor definition, Eq. (3.16) is considered, the surface roughness of the real biomass particles decreases the shape factor compared to a smooth cylinder, which supports the lower values used in the simulations. This indicates that the sphere-equivalent diameters, densities and shape factors are fairly accurately determined. The velocity profiles in Fig. 6.10, especially of the group B1a, indicate that the non-spherical drag law of Haider and Levenspiel [22] can describe the drag force of the biomass particles relatively accurately.

The deviations between the measurements and calculations for the size groups B1b and B1c are mostly affected by inaccurate measurements. Too few particle velocity samples were obtained for the experimental mean velocity calculations. For example, in the last three measurement points of the size group B1c, only 3, 8 and 17 velocity samples were obtained for calculating the experimental mean velocity. For this reason, the experimental data is not statistically representative, which has to be taken into consideration when the simulation results are compared with the measurements. In case of the size group B1a, from hundreds to thousands velocity samples were obtained for each experimental mean velocity point. With this group, the experimental mean velocities can be much better trusted. The shape factor value that was determined for the group B1a was therefore used also for the larger size groups B1b and B1c. This gave a relatively good match with the experimental measurements.

The calculated velocity profiles match very poorly with the measurements for the size group B2a. With this particle size group, there was no shape factor value that portrayed the experimental particle velocities. As discussed in the thesis of Teemu Saarinen, the experimental work with this particle size group was challenging, because the particles tended to form large clusters that were difficult to separate. For this reason, the particle imaging software recognized mainly clusters in the images and the sphere-equivalent particle diameters became too large compared to reality. This is most probably the reason for the difficulties in the velocity calculations, as the sphere-equivalent particles in the CFD model represent more of these clusters than separate particles. In contrast, the velocity data indicates that the particles were dropping as individual particles. For this reason, the modeling of the group B2a is rather unsuccessful.

The ten size classes had remarkably different velocity profiles within all size groups except B1a. In other words, the velocities of the smallest particles were significantly smaller than the velocities of the largest particles, as seen in Fig. 6.10. This is reasonable, because the larger particle size groups had a remarkably wider size distribution. The large velocity deviations were clearly seen in the experimental data as well. The experimental velocities in Fig. 6.10 do not have a large standard deviation in all measurement points, but this is caused by the fact that some measurements had only a few velocity samples in the mean value calculations. Furthermore, it was seen in the experimental velocity data that more velocity samples were obtained from the smallest particles within each size group. The small particles were greater in number and had a lower velocity, and therefore a higher probability to be at the measurement window position to be captured in the figures of the CCD camera. For this reason, the small velocities might be overly represented in the experimental data. When the smallest and largest velocities in the experimental data were compared with the smallest and largest particle velocities of the CFD simulation, the values were well comparable. This further indicates that the shape factor values are accurately determined. All in all, the non-spherical drag law seems to predict the particle velocities with a fairly good accuracy.

In the future, more velocity samples should be obtained for different size groups in order to have a better statistical representation of the particle velocities. A narrower size distribution could also be used in order to prevent too large deviations between the particles of different size, and to prevent small particles being overly represented in the experimental data. These observations can be taken into account in the future work in order to obtain more accurate results for the reactivity parameters and shape factor values.

6.4 Particle Mass Loss Results

The conversion curves presented in this section were calculated with the optimized reactivity parameters of Teemu Saarinen [5], using the CFD models of the DTR introduced in previous sections. The results are compared with the experimental mass loss data obtained from the DTR experiments presented in Section 4.3. Fig. 6.12 presents two possibilities of how the particle conversion curves can be plotted. In the figure above, the particle conversion is presented as a function of path length, in other words as a function the distance the particles have traveled after coming out from the feeding probe, while the figure below presents the mass loss as a function of residence time inside the reactor.
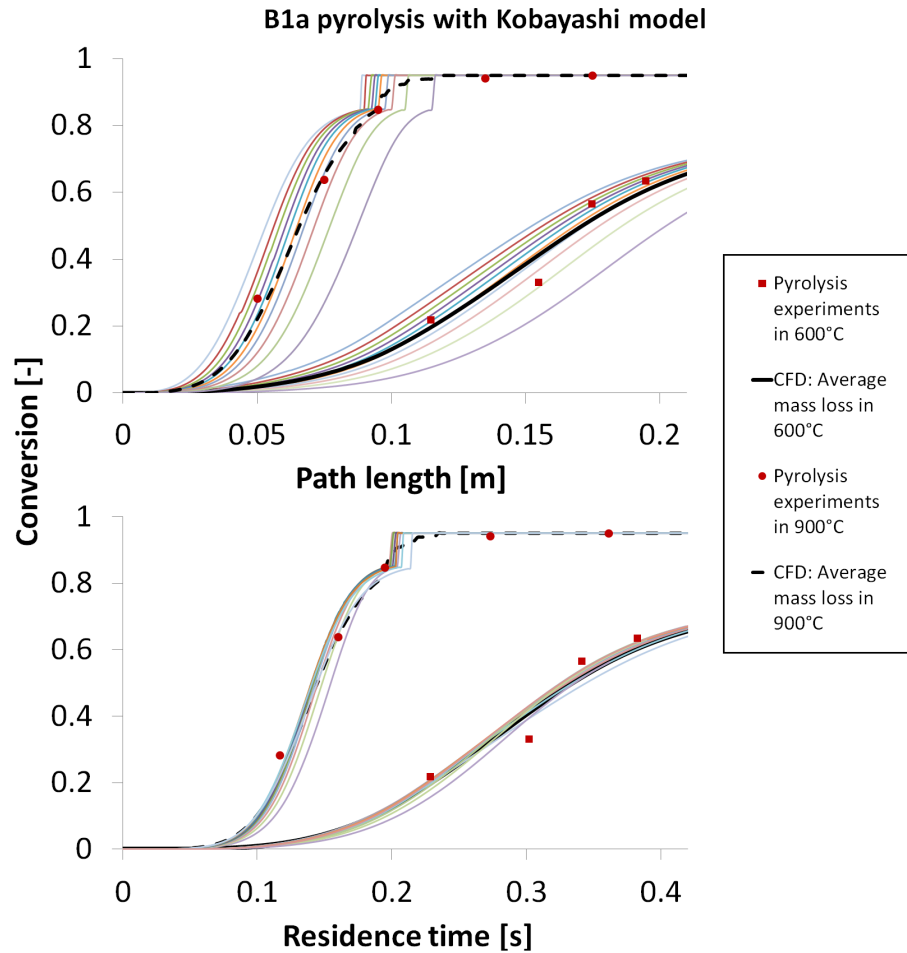
Figure 6.12 *Particle mass loss during devolatilization presented as a function of path length (above) and time (below) for the size group B1a. The thin curves present the mass loss of the ten size classes introduced in Table 5.1, while the thick curves are their average. The devolatilization model in the simulation was the Two-Competing-Rates (Kobayashi) model.*

In Fig. 6.12, the thin curves present the mass loss of the ten particle size classes of the size group B1a introduced in Table 5.1. The thick curves present the average value of these size classes. Because the experimental points represent the average mass loss of all particles belonging in the size group B1a, the thick curves should be compared with the measurements.

The conversion curves of the ten size classes as a function of residence time were directly obtained from the CFD simulation. The average mass loss curve (thick curve) as a function of time was calculated by averaging the residence times and mass losses of the ten size classes, after each of them had traveled the same length inside the reactor. Another option would have been to average the mass loss after each size class had traveled the

same time and different length inside the reactor. The first option, however, represents the real experimental setup, as the drop height was kept constant when one experimental point in Fig. 6.12 was measured. The experimental mass loss points were only obtained as a function of path length, but they were transformed as a function of time by using the mean velocity profiles of the size groups obtained from the CFD simulations.

It must be noted that the conversion curves of the CFD simulation in Fig. 6.12 were obtained from a single model, where the particle drop height was 21.5 cm. In contrast, the experimental points were obtained from multiple drop heights. In reality, the temperature and flow fields inside the reactor change slightly between different particle drop heights due to different reactor wall temperature profiles. Therefore, direct comparison between the experiments and simulations could only be made if the simulations were conducted separately for the same drop heights that were used in the experiments. However, the changes in the particle temperature histories are small between the different particle drop heights, and the simulated conversion curves from a single drop height can be relatively safely compared with the measurements.

In the following sections, the mass loss results will be presented as a function of residence time, because that gives more information on the fuel reactivity than the results presented as a function of path length. The conversion curves of the ten size classes will not be presented and only the average conversion curves will be shown.

6.4.1 Biomass Fuel 1

Devolatilization of Biomass Fuel 1

The conversion curves during devolatilization in nitrogen atmosphere in both temperature levels are presented in Fig. 6.13. The figure shows the average conversion curves for the three size groups calculated with the Single-Rate and the Kobayashi devolatilization models. The conversion curves for the size group B1a were calculated with a DTR model, where the particle drop height was 21.5 cm. For the smallest particles, this drop height was enough for obtaining full volatile yield in 900°C. As the experimental points indicate, the volatile yield in the 900°C temperature level was as high as 95% (dry) for the size group B1a. In the simulations, this was set as the predetermined amount of volatiles for these particles.
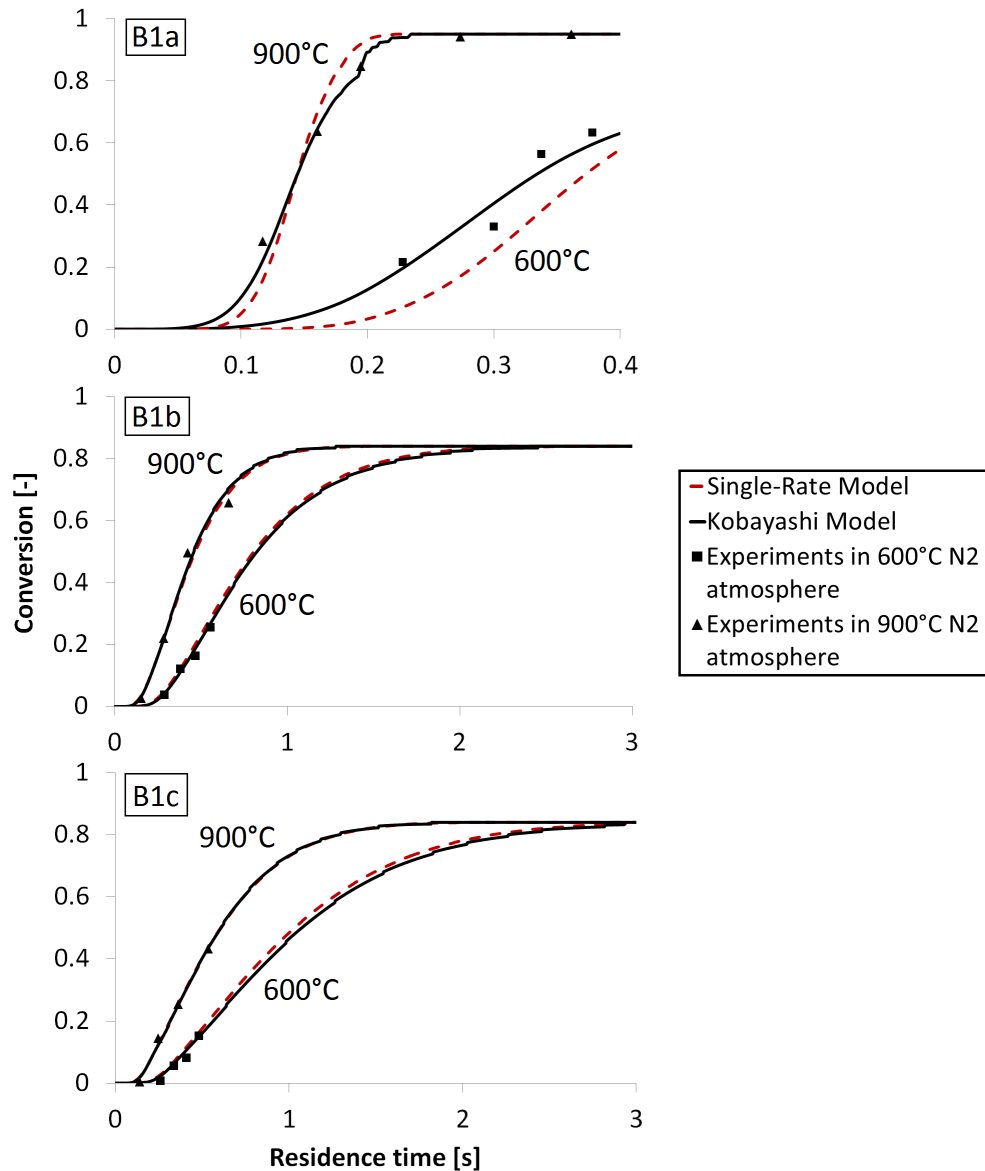
Figure 6.13 *The mean conversion curves during devolatilization in nitrogen atmosphere for the three size groups of biomass fuel 1. The conversion curves are compared with the measurements in 600°C and 900°C temperature levels, using both Single-Rate and Kobayashi devolatilization models. The curves are presented for dry particles with predetermined volatile yields of 95% for B1a and 84% for B1b and B1c.*

As seen in Fig. 6.13, the last experimental measurements for the size groups B1b and B1c were obtained at the middle of the pyrolysis process. The maximum drop height of the DTR was 67.5 cm and this was not sufficient to give information on the final volatile yield. However, the DTR length was extended up to 3 m in the CFD model, and this way the full conversion curves for these size groups could be calculated.

Fig. 6.13 shows that both devolatilization models can predict the average conversion of the three size groups with a good accuracy. In case of size group B1a, the Single-Rate model gives a slightly worse respond compared to the Kobayashi model. The reason can possibly be in the optimization settings and it has to be further analyzed. Therefore, no conclusions on the superiority of the Kobayashi model can be made.

In case of the size groups B1b and B1c, both devolatilization models give a similar respond and no notable differences can be pointed out. The conversion curves go very well through the experimental points in both temperature levels, and finally reach the predetermined volatile yield of 84% (dry). The maximum volatile yield for these size groups was taken from the proximate analysis, as the DTR length was not sufficient to reach full conversion for the larger particles. One target for the future development would be to modify the DTR so that the high heating rate volatile yield could be measured for also the larger particle size groups.

An additional observation, that cannot be seen in Fig. 6.13, was made during the experiments. The final volatile yield for the size group B1a in the 600°C level (71% of dry weight) was lower compared to the 900°C one (95%). This is well in line with the literature, as the lower heating rate results in lower volatile yield and higher char yield after devolatilization. Different volatile yields in different temperatures cannot be taken into account with the existing models, as the final yield is a predetermined constant. Therefore the conversion curves have to reach the same limit in both temperature levels, as seen in the figures of the size groups B1b and B1c, but the final volatile yield in reality would probably be lower in the 600°C temperature level. However, this is not a significant factor considering combustion simulations, because the particles will always experience rather high heating rates and reach the volatile yields similar to the 900°C temperature level. However, as the idea behind the Kobayashi model is to predict the different volatile yields for different heating rates, the full potential of the model could be better exploited if the final volatile yield would be a variable.

The reactivity parameters were optimized separately for the three size groups. However, the conversion curves for the size groups B1b and B1c were calculated with the same parameters, those of the size group B1b. The reactivity parameters of the smallest size group (B1a) could not describe the experimental mass loss of the larger groups. The reason for this behavior is most probably the different particle heat transfer inside the reactor, as the different particle size and Biot number result in a different respond to the high heating rates. The observation that the same reactivity parameters work for both

of the larger size groups suggests that they have a similar temperature respond, non-isothermal in reality, which can be described by the same apparent reactivity parameters.

An important notion concerning the current modeling strategy relates to the temperature histories of the particles. In reality, the biomass particles are not spherical nor isothermal and the temperature histories are not realistically calculated in the simulation. The apparent reactivity parameters, however, can accurately describe the mass loss of the particles using the simplified spherical and isothermal approach. Most importantly, if the spherical and isothermal heat transfer together with the optimized parameters describes the mass loss of the real particles in a wide range of flow and temperature conditions, then the conversion of the particles can be correctly calculated in combustion simulations regardless of the non-realistic temperature histories. To test this assumption, the modeling approach is further examined in turbulent conditions in the 50kW reactor simulation described in Section 7.2.2.

The results indicate, that the mass loss during devolatilization can be modeled with a detailed accuracy if the particle residence times and temperature histories are correctly determined in the parameter optimization. The accuracy of the reactivity parameters strongly depends on the accuracy of determining the particle velocities, and therefore CFD modeling validated by experimental data can provide the most accurate information needed for the reactivity parameter optimization. In the parameter optimization of Teemu Saarinen [5], the particle residence times were obtained using both velocity measurements and CFD modeling. In case of B1a, the mean velocity profile in the optimization was obtained by a direct fit to the experimental data. For B1b and B1c, the mean velocity profiles were taken from the CFD model, presented in Fig. 6.10, as the experimental velocity measurements suffered from statistical uncertainties. If the velocity measurements of B1b and B1c were directly used in the optimization, the reactivity parameters would not have worked in the CFD model as well as presented in this section.

Combined Devolatilization and Char Burnout of Biomass Fuel 1

Fig. 6.14 presents the conversion curves in combined devolatilization and char burnout. As discussed earlier, the experimental mass loss measurements were conducted in two different atmospheres containing 3 vol-% and 21 vol-% oxygen and the rest nitrogen, in a temperature level of 900°C. Raw biomass particles were used, because the char particles from the devolatilization experiments were too fragile to be used in further experiments.
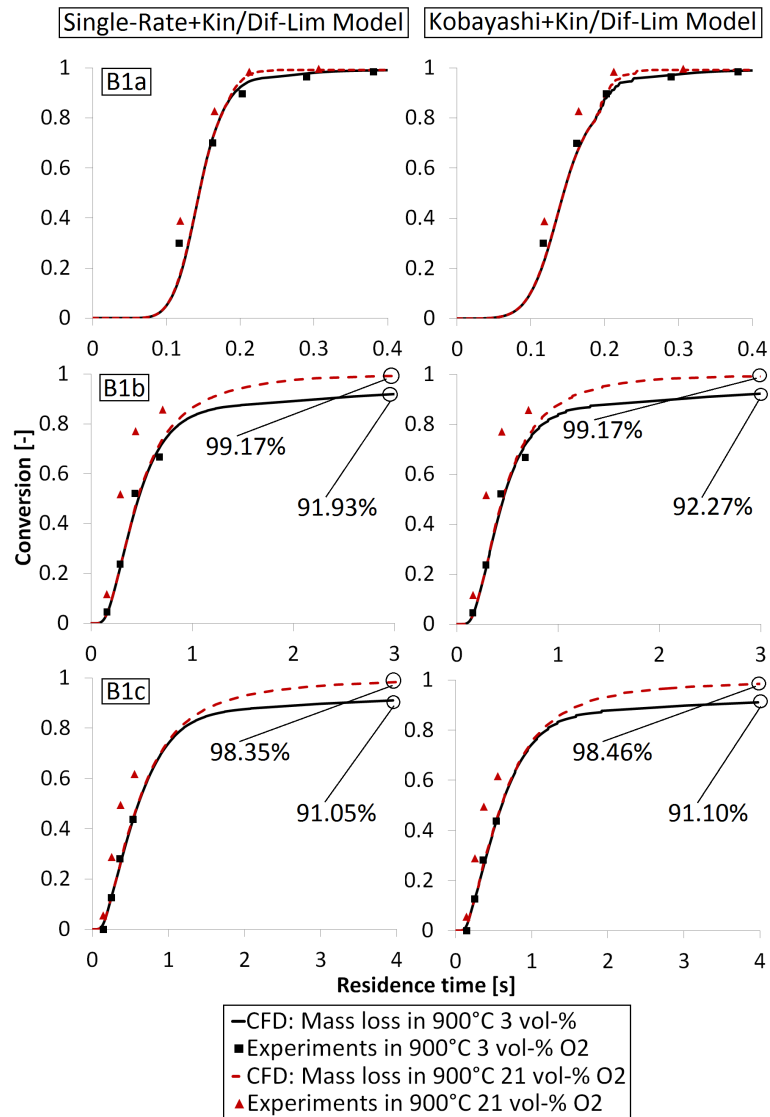
Figure 6.14 *The mean conversion curves during combined devolatilization and char burnout for the three size groups of biomass fuel 1. The conversion curves are compared with the measurements in 3 vol-% and 21 vol-% oxygen levels, using Single-Rate or Kobayashi models for devolatilization and Kinetics/Diffusion Limited model for char burnout. The curves are presented for dry particles.*

In the CFD modeling, the devolatilization and char burnout could only occur consecutively. During devolatilization, the conversion depends on the particle temperature and therefore only slightly depends on the oxygen content in the atmosphere. For this reason, the conversion curves during devolatilization stage are similar in all 900°C simulations independently of the gas atmosphere. During the char burnout stage, however, the mass loss rate depends strongly on the oxygen level. As a result, the conversion curves in the CFD model can only deviate from one another after the char burnout stage begins.

In 3 vol-% of oxygen, the experimental measurements for all size groups show an identical mass loss with the devolatilization experiments in 900°C nitrogen atmosphere. Therefore, the devolatilization model can predict the conversion curves in accordance with the measurements in this lower oxygen level. However, the experimental mass loss rate becomes greater with all size groups right from the beginning of the conversion curves, when the oxygen concentration increases to 21 vol-%.

The greater mass loss rate in high oxygen level indicates that in reality the devolatilization and char burnout stages occur simultaneously in these conditions. This effect cannot be taken into consideration with the existing model coupling. Therefore, in the future the modeling could be improved by allowing simultaneous combustion stages to occur. In addition, in the future experiments the DTR test facility should be reconstructed so that the mass loss behavior of the larger particles could be measured as a whole. All in all, the reactivity parameters are expected to work reasonably well, if the oxygen level surrounding the particles is not too much over 3 vol-% of oxygen.

6.4.2 Biomass Fuel 2

Devolatilization of Biomass Fuel 2

Biomass fuel 2 consisted of two visually different materials. The smallest fraction was very fine, but the particles tended to stick together and form clusters that were difficult to handle in the experimental measurements. The densities of these two materials were also different, as was discussed in Section 4.3. The final volatile yield of B2a was set to 68% of the dry weight (based on experiments) and 77.2% for the groups B2b and B2c (based on proximate analysis). The conversion curves of B1a were calculated with a CFD model of the DTR, where the particle drop height was 67.5 cm. The curves of B2b and B2c were calculated with the extended model of the reactor, having a length of 3 m. Fig. 6.15 presents the conversion curves for all size groups.

The mass loss rate of B2a is slightly too low in both temperature levels. The reactivity parameters were optimized using a mean velocity profile that was directly fitted to the experimental velocity data. However, as seen in Fig. 6.11, the velocity of B2a in the CFD model deviates remarkably from the measurements. This explains the deviation between the experimental data and modeled conversion curves for this size group.

Figure 6.15 *The mean conversion curves during devolatilization in nitrogen atmosphere for the three size groups of biomass fuel 2. The conversion curves are compared with the measurements in 600°C and 900°C temperature levels, using both Single-Rate and Kobayashi devolatilization models. The curves are presented for dry particles with the maximum volatile yields of 68% for B2a and 77.2% for B1b and B1c.*

The higher particle velocities of B2a in the CFD model compared to measurements were mainly caused by too large sphere-equivalent diameters. The particle imaging software constructed non-realistic particle diameters, because the small particles were identified as clusters in the images. Because the particles were too large in the CFD model and

in the reactivity parameter optimization, the results for the group B1a are unsuccessful in some extent. In order to model the devolatilization of this group accurately, the sphere-equivalent diameters should be measured with a better accuracy. After that, the particle velocities could be better captured in the CFD model and the reactivity parameters could be optimized for the correct particle size classes. Considering larger scale combustion simulations, the reactivity parameters, particle trajectory calculations, and sphere-equivalent diameters together determine the accuracy of the particle combustion modeling. These factors determine in which position and how much volatile gases are released in simulations.

The conversion curves of the size groups B2b and B2c were calculated again with the same reactivity parameters, those of B2b. Because the particle size distributions of these groups were relatively similar, it was expected that the groups have the same apparent reactivities similarly with the larger groups of biomass fuel 1. As seen in Fig. 6.13, the conversion curve of B2c in the 900°C temperature goes slightly under the experimental measurements. If the separately optimized reactivity parameter were used for B2c, the mean conversion curve would go better through the measurements. This indicates that the apparent reactivity of the larger groups can be slightly different in the higher temperature level, for example due to increasing aspect ratio of the larger particles which results in different heat transfer. However, the difference in the reactivities can also be caused by small inaccuracies in the measurements.

Combined Devolatilization and Char Burnout of Biomass Fuel 2

The conversion curves for biomass fuel 2 are presented in Fig. 6.14. Again, no differences between the models can be observed. In case of B2a, the earlier discussed reasons cause the inaccurate modeling of this size group. For the larger groups, the B2b devolatilization parameters were again used. The char burnout parameters were taken from B2a optimization, as no other parameters were available.

As seen in Fig. 6.14, the oxygen level has even larger effect on the experimental particle conversion than with biomass fuel 1. The conversion curves in 3 vol-% oxygen can be reasonably well modeled with the size groups B2b and B2c. The increasing mass loss rate in the high oxygen level cannot be modeled due to consecutive devolatilization and char burnout stages and the conversion curves in 21 vol-% oxygen are poorly predicted. Similarly with the biomass fuel 1, no experimental data was obtained after a certain resi-

dence time and no data from the end of the conversion curves was obtained. All in all, the reactivity parameters are expected to work in low oxygen levels for the larger groups, but accurate modeling in higher oxygen levels would require modifying the model coupling.
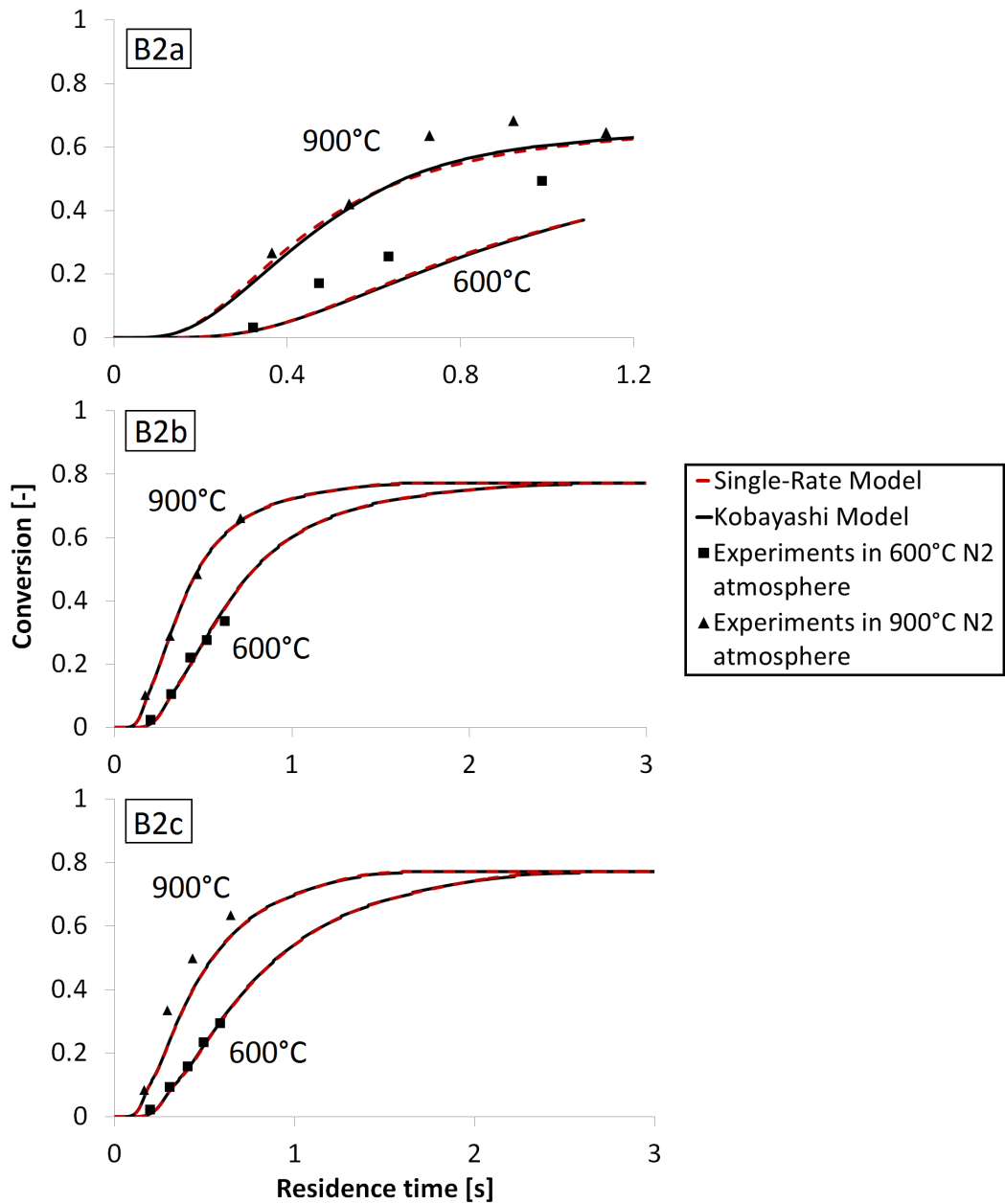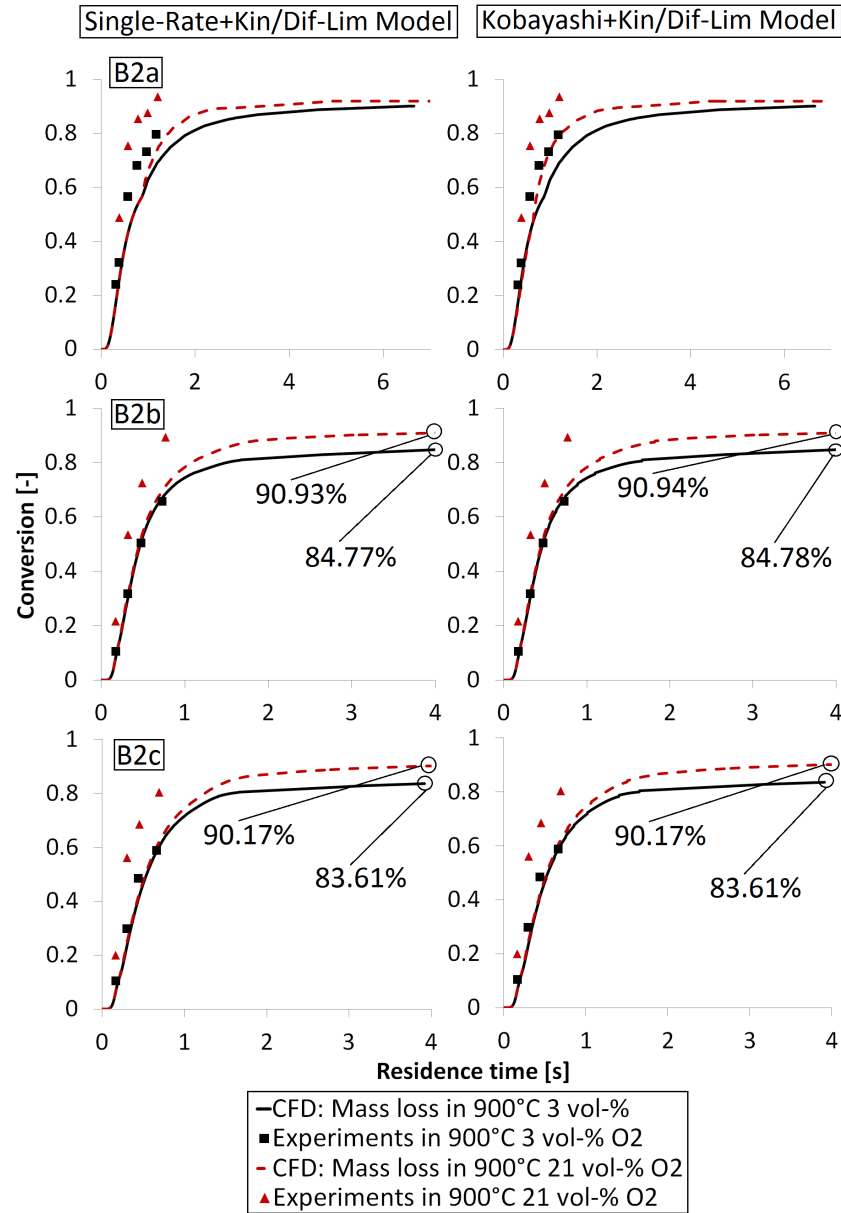

Figure 6.16 The mean conversion curves during combined devolatilization and char burnout for the three size groups of biomass fuel 2. The conversion curves are compared with the measurements in 3 vol-% and 21 vol-% oxygen levels, using Single-Rate or Kobayashi models for devolatilization and Kinetics/Diffusion Limited model for char burnout. The curves are presented for dry particles.

6.5 Mesh Independence

The mesh independence of the calculation results was studied by comparing the flow and temperature fields of the DTR with three different computational meshes. The gas velocity at the center line of the reactor for the three meshes is presented in Fig. 6.17. The simulations were conducted for the 600°C wall temperature and pure N_2 atmosphere. The particle feeding probe outlet was at position x = 48 cm below the reactor top and the gas velocity is shown from that point onwards. The window pipes shown in Fig. 6.8 were excluded from these simulations.
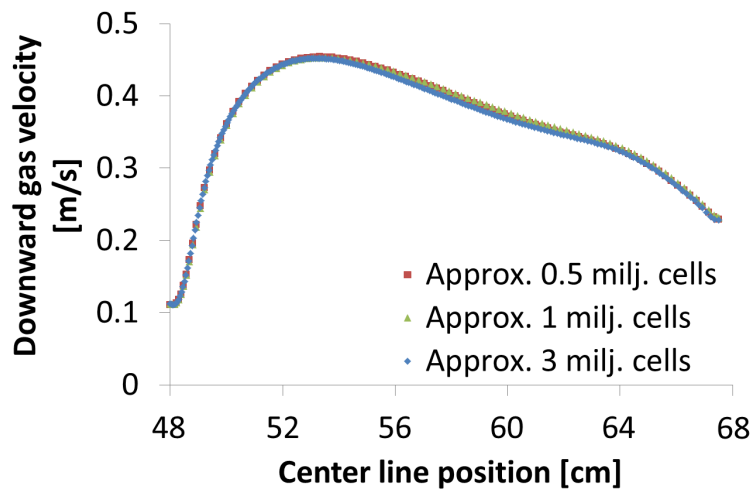
Figure 6.17 *The gas velocity at the center line of the reactor for three computational meshes.*

Fig. 6.17 shows that the gas velocity does not change significantly when the mesh is refined. Other flow variables behaved the same manner and the results were concluded to be mesh independent. Similar cell density than in the mesh containing half a million cells was used in the thermocouple, flow field and particle mass loss simulations.

7. CFD MODEL OF THE 50 KW TEST REACTOR

The model of the 50 kW test reactor was used for testing the optimized devolatilization (Single-Rate model) and char combustion (Kinetics/Diffusion Limited model) reactivity parameters of biomass fuel 1. No biomass combustion tests could be conducted in the reactor during the time of writing the thesis. For this reason, the simulation results could not be compared with experimental data and no quantitative data on the functioning of the reactivity parameters was obtained. However, the CFD model of the 50 kW reactor was validated by simulating lignite combustion which had previous experimental data to be compared. Details about the lignite combustion tests can be found in reference [33], where the conventional air combustion case presents the simulation setup used in this thesis. After lignite combustion simulation, the same mesh and calculation setup was used in biomass fuel 1 simulation, in order to obtain qualitative data on the functioning of the reactivity parameters. Details about the 50 kW reactor can be found on Table 7.1.

Table 7.1 *Details about the 50kW pulverized fuel test facility at Dresden University of Technology.*

Nominal Heat Input	50-60 kW_{th}
Burner	Swirl burner at roof
Cooling	Air-cooled walls
Combustion Chamber	Cylindrical - Inner diameter 0.29m - Height 2.50m

This chapter consists of three sections. Section 7.1 presents the calculation methods that were used in both modeling cases. The results of lignite combustion simulation are presented in Section 7.2.1, where the computational results and measurements are compared. Finally, Section 7.2.2 presents the results of biomass fuel 1 simulation, following by discussion about the reactivity parameter functioning.

7.1 Calculation Methods

7.1.1 Description of the Models

The modeling was conducted with the commercial CFD software ANSYS Fluent 16.1. The geometry and computational mesh were created with ANSYS DesignModeler and ICEM CFD 16.1, respectively. The computational mesh was three dimensional and contained 2.2 million hexahedral cells. The surface mesh of the burner and of a part of the combustion chamber are presented in Fig. 7.1.

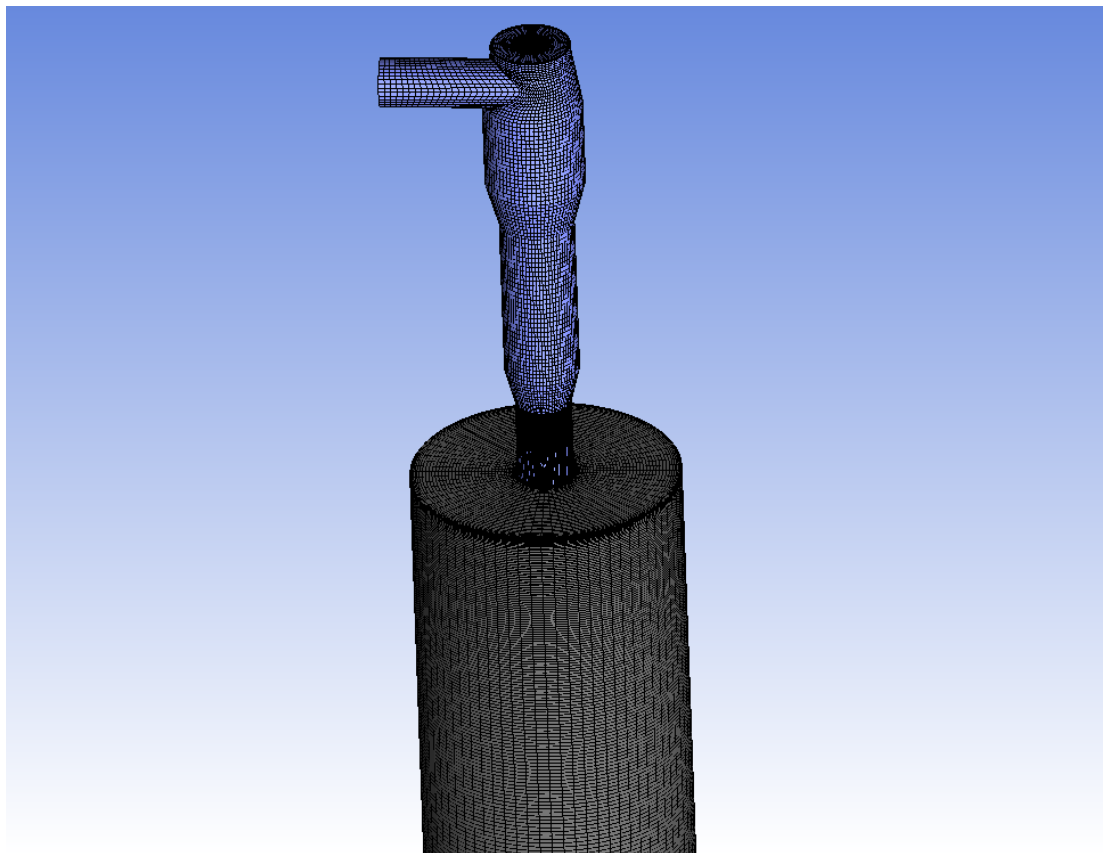***Figure 7.1*** *The surface mesh of the burner and of a part of the combustion chamber of the 50kW test reactor.*

As discussed before, two different simulation cases were studied: the first for lignite and the second for biomass fuel 1 combustion. The fuel properties of lignite are presented in Table 7.2, while the properties of biomass fuel 1 were already presented in Chapter 4 in Table 4.2.

The models that were used in both simulation cases are presented in Table 7.3. The turbulence was modeled with the Reynolds Stress Model (RSM). As discussed in the theory section, the RSM is better suitable for highly swirling flows than the traditional k-ε models, because it does not assume isotropic turbulence. The wall boundary layers were resolved with the enhanced wall treatment in order to achieve better accuracy compared to the standard wall functions. The radiation was modeled with the Discrete Ordinates (DO) model using the Weighted-Sum-of-Grey-Gases method (WSGGM) for the mixture radiative properties.

Table 7.2 *The ultimate and proximate analyzes for lignite [33]. The analyzes were needed in various stages of setting up the simulation, for example in calculating the volatile species properties.*

Proximate analysis		Ultimate analysis, DAF	
Moisture [w-%]	10.8	Carbon [w-%]	67.2
Ash [w-%]	4.8	Hydrogen [w-%]	5.2
Volatile matter [w-%]	47.4	Oxygen [w-%]	26.5
Fixed carbon [w-%]	37	Nitrogen [w-%]	0.7
Lower heating value (LHV) [MJ/kg]	21.3	Sulphur [w-%]	0.4

The turbulence-chemistry interaction was modeled with the Finite-Rate/Eddy-Dissipation Model. The model is not recommended for multi-step reaction mechanisms [6] and therefore a rather simple chemical mechanism was used in the simulations, as seen in Table 7.3.

Table 7.3 *Simulation details and submodels for the 50kW test reactor simulations.*

Computational Mesh	2.2 million cells
Solver	ANSYS Fluent -Pressure-Based Steady solver
Turbulence Model	Reynolds Stress Model (RSM) with Enhanced Wall Treatment
Combustion Model	Finite-Rate/Eddy-Dissipation Model
Chemical Mechanism	Three global reactions: 1) Volatiles $+ O_2 \rightarrow CO + H_2O + N_2$ 2) Char $+ \frac{1}{2}O_2 \rightarrow CO$ 3) $CO + \frac{1}{2}O_2 \rightarrow CO_2$
Particle Model	Discrete Phase Model (DPM)
Devolatilization Model	Single-Rate model
Char Burnout Model	Kinetics/Diffusion-Limited model
Radiation Model	Discrete Ordinates (DO) with WSGGM for mixture radiative properties

The first reaction in Table 7.3 represents the combustion of a pseudo-volatile species that is released from the particles in the devolatilization stage. The pseudo-volatile species is a simplification in the numerical modeling as it accounts all the chemical species that are released from the particles during devolatilization. The composition of the pseudo-volatile species was calculated based on the ultimate and proximate analysis, so that the chemical species were in balance in the combustion process. The reactions for lignite and biomass fuel 1 are presented in Eq. (7.1) and Eq. (7.2), respectively. For simplification, the sulphur in the fuels was included as nitrogen and all nitrogen was released during devolatilization. The reaction rates for Eq. (7.1) and (7.2) were calculated with the default parameters available for coal volatiles in Fluent database.

$$C_{0.290}H_{0.531}O_{0.171}N_{0.0081} + 0.192O_2 \rightarrow 0.290CO + 0.266H_2O + 0.0041N_2 \qquad (7.1)$$

$$C_{0.275}H_{0.502}O_{0.220}N_{0.0027} + 0.153O_2 \rightarrow 0.275CO + 0.251H_2O + 0.0014N_2 \qquad (7.2)$$
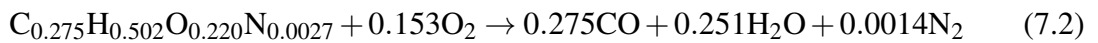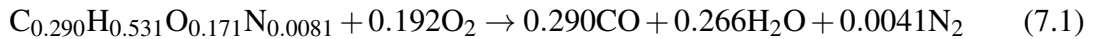
The second reaction in the simulations was the char burnout reaction (see Table 7.3). It was assumed that the char consists of solid carbon and reacts to only carbon monoxide. The reaction heat from char burnout was completely absorbed by the particles, as recommended in Fluent theory guide [6]. The third and final reaction in Table 7.3 accounted for the oxidation of carbon monoxide to carbon dioxide.

The fuel particles were modeled with the Discrete Phase Model (DPM) (see Section 3.5). The drag force on the particles was calculated using the spherical drag law for lignite and the non-spherical drag law for biomass fuel 1. The shape factor determined from the DTR simulations was used in the non-spherical drag law for biomass fuel 1. The turbulence interaction on the particle movements was taken into consideration with the Discrete Random Walk model (DRW) using 10 number of tries for the particle trajectories. The moisture content of the particles was modeled using the wet combustion option available in DPM.

The devolatilization and char combustion stages were modeled using the Single Reaction Rate model and the Kinetics/Diffusion-Limited Rate model, respectively. The reactivity parameters for both fuels are shown in Table 7.4. The parameters for lignite were the default parameters for coal available in Fluent database, while the biomass fuel 1 parameters were the optimized parameters of Teemu Saarinen [5].

In biomass fuel 1 devolatilization, different reactivity parameters and volatile contents were used for different particle size ranges, as seen in Table 7.4. The reactivity parameters of the smallest size fraction (B1a, 112-125 μm of sieving size) were used for all particles

having a sphere-equivalent diameter less than 400 μm. For these particles, the volatile content was set to 95% of the dry weight as measured in the DTR tests. The reactivity parameters of the medium size fraction (B1b, 500-600 μm of sieving size) were used for the rest of the particles ($\geq$ 400 μm) together with a volatile content of 84% of the dry weight. All particles had the char burnout reactivity parameters of B1a.

Table 7.4 *The reactivity parameters and particle properties for both fuels in the 50kW reactor simulations. The parameters used for lignite are the default parameters for coal available in Fluent database, while the biomass fuel 1 parameters are those optimized by Teemu Saarinen [5].*

	Lignite	**BIOMASS 1**	
Devolatilization: Single-Rate reaction model	A = 3.82e+05 [1/s] E = 7.40e+07 [J/kmol]	$d_p < 400$μm	A_1 = 2.99e+06 [1/s] E_1 = 8.89e+07 [J/kmol]
		$d_p \geq 400$μm	A_2 = 1.10e+02 [1/s] E_2 = 2.42e+07 [J/kmol]
Char Burnout: Kinetics/Diffusion-Limited reaction rate model	C = 5.00e-12 [-] A = 2.00e-03 [1/s] E = 7.90e+07 [J/kmol]	C = 5.00e-12 [-] A = 2.81e-03 [1/s] E = 6.29e+07 [J/kmol]	
Volatile content, dry [w-%]	63	$d_p < 400$μm	95
		$d_p \geq 400$μm	84
Char content, dry [w-%]	31.6	$d_p < 400$μm	4.17
		$d_p \geq 400$μm	15.17
Density, dry [kg/m³]	700	700	
Specific heat, dry [J/kg K]	1680	1500	
Swelling Coefficient [-]	1.4	0.9	
Reaction heat absorbed by solid [%]	100	100	

In case of lignite, same reactivity parameters and volatile content were used for all particles. The volatile content was set to 63% of the dry weight, which was slightly higher than the value determined in the proximate analysis. Higher value was used because the higher heating rate the particles experience in combustion probably results in a higher volatile yield compared to the thermogravimetric analyzer typically used in proximate analysis.

7.1.2 Boundary Conditions

Both fuels were introduced into the computational domain through surface injections from the primary air inlet boundary. A surface injection introduces one particle stream into the computational domain from every computational cell face of the surface. The size distributions of the fuels are shown in Fig. 7.2. A Rosin-Rammler fit was calculated for both fuels using the sieve analysis results. For biomass fuel 1, the sphere-equivalent diameters were used instead of the true sieving size in order to account for the non-spherical shape of the particles. The lignite particles were approximated as spheres and the sieving size was directly used to construct the Rosin-Rammler fit. After that, the size distributions were discretized into 30-35 different particle diameters and the mass fraction of each diameter was calculated using the Rosin-Rammler equation. Finally, the mass flow rate for each particle injection was obtained by multiplying the mass fraction of the discrete particle size with the total fuel mass flow rate. This resulted in 30-35 particle surface injections each containing a different particle diameter. The total number of tracked particles were 357 000 and 316 200 for lignite and biomass fuel 1, respectively.
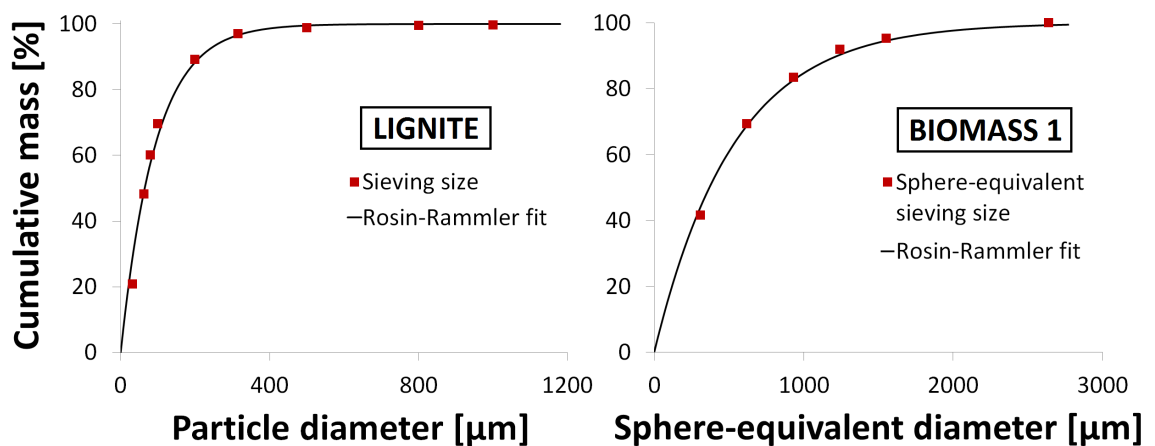
Figure 7.2 *The particle size distributions used in the 50kW reactor simulations.*

A schematic figure of a cross section of the computational domain is presented in Fig. 7.3. Two burner inlets were used: the primary air inlet for the recirculated flue gas and fuel particles, and the secondary air inlet for the combustion air. All walls in the computational domain were modeled as thin walls. The outlet boundary was set at the lower end of the combustion chamber, 2.5 m below the burner outlet.
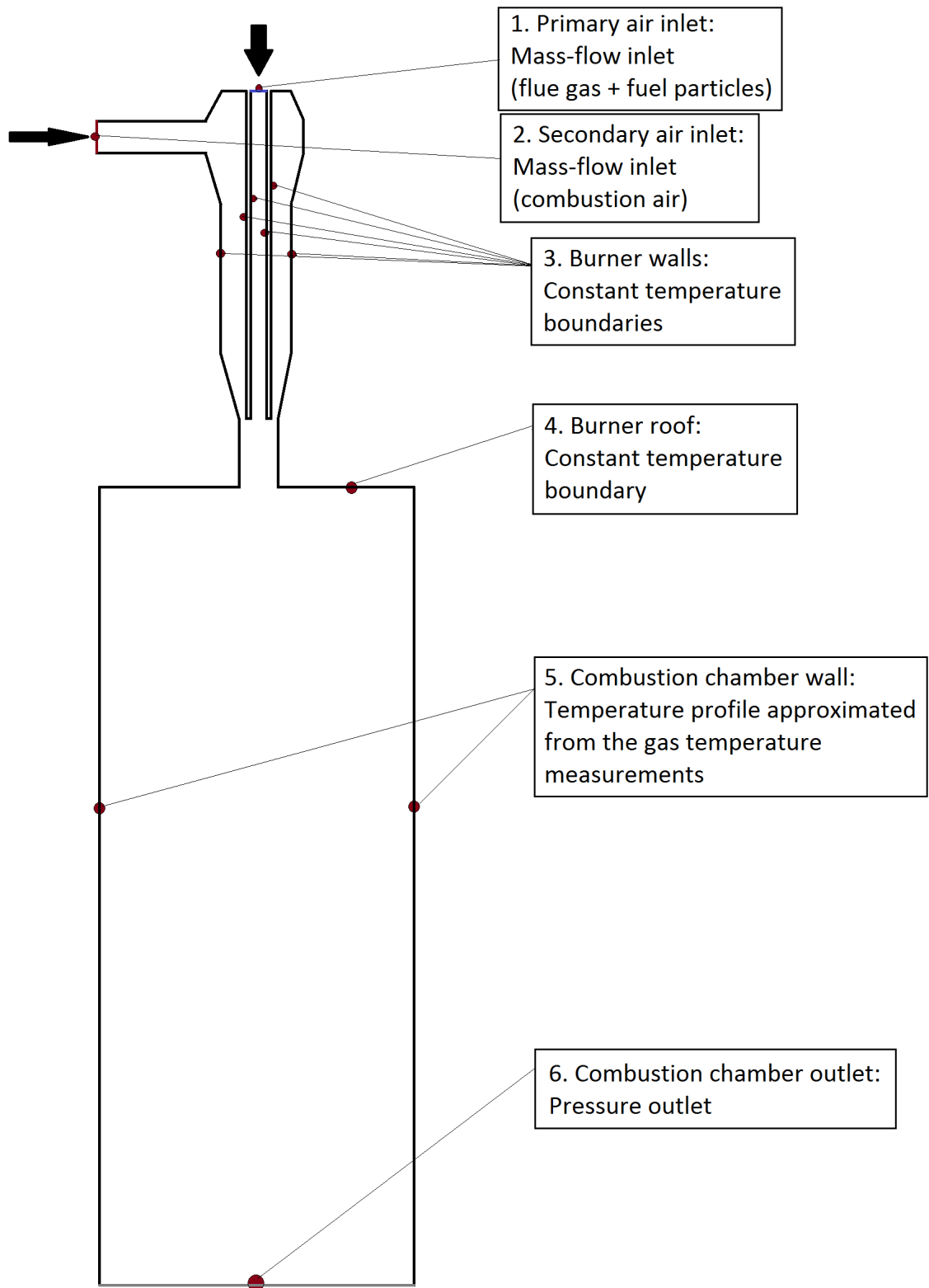
Figure 7.3 *A schematic figure of a cross section of the computational domain of the 50 kW test reactor. Not in scale.*

The boundary conditions in the lignite simulation were based on information available from the combustion tests in reference [33]. Similar conditions were used in biomass fuel 1 simulation, so that the results could be easily compared. The boundary conditions in the primary and secondary air inlets are presented in Table 7.5. At the primary air inlet, flue gas was used as a carrier gas for the fuel particles. The composition of the carrier gas was calculated so that it had the same composition that would result from the perfect combustion of fuel and combustion air, but it was assumed that the excess oxygen had further reacted to CO_2. This was justified by looking at the experimental measurements from the lignite combustion tests. In the experiments, the volume fraction of oxygen close to the reactor outlet was so low that it could have not been achieved if oxygen was present in the carrier gas. In addition, without this assumption the CO_2 levels would have been too low in the simulations compared to the measurements. The assumption of zero oxygen in the carrier gas seems reasonable, as the oxygen left in the flue gas may have been consumed already in the flue gas filtering system and pipe network before the burner. Another reason for the lower oxygen levels in the measurements could be that the mass flow rate of the combustion air had been slightly lower, or the mass flow rate of the fuel slightly higher in the combustion tests, than the rounded values taken from the experimental report.

Table 7.5 *The boundary conditions used in the primary (flue gas + fuel particles) and secondary air (combustion air) inlets.*

	Lignite	**Biomass fuel 1**
Fuel feed rate	10 kg/h	12.8 kg/h
Air feed rate	89 kg/h - Pre-heated to 300˚C	87.7 kg/h - Pre-heated to 300˚C
Flue gas recirculation	25 kg/h - Carrier gas for the particles (190 ˚C)	25 kg/h - Carrier gas for the particles (190 ˚C)
Air-Fuel equivalence ratio	1.26	1.26
Heat input	59 kW$_{th}$	59 kW$_{th}$

The mass flow rate and the temperature of the flue gas were 25 kg/h and 190 °C, respectively. The particles entered into the domain with a slightly smaller velocity than the gas. In reality, the particles had probably lost some of the moisture already in the pipe network. Nevertheless, in the simulation the particles entered the burner with full moisture content and therefore their temperature was set to 100°C to begin the boiling law of the DPM model (see Section 3.5.2) immediately at the inlet boundary. At the secondary air inlet, the combustion air entered at the domain preheated to 300°C. The mass flow rate of

the combustion air was based on an air-fuel equivalence ratio of 1.26 in both simulation cases. The fuel heat input was fixed at 59 kW for both fuels.

The temperature boundary conditions at the burner walls were chosen so that the walls had the same temperature as the gas that was in contact with the wall. For example, the burner walls that were in touch with the combustion air were set to 300 °C. Furthermore, the combustion chamber wall had a temperature profile based on the gas temperature measurements of the lignite combustion tests, and it is presented in Fig. 7.4. The chamber wall temperature was adjusted in a slightly lower temperature than measured for the gas in the close vicinity of the wall. Modeling the air-cooling of the combustion chamber wall would have been too time consuming and therefore this simplified approach was used. The same temperature profile was used in the biomass fuel 1 simulation, as no experimental data was available. The combustion chamber roof was kept at a constant temperature of 1000 °C, and the combustion chamber outlet had a pressure outlet boundary condition.
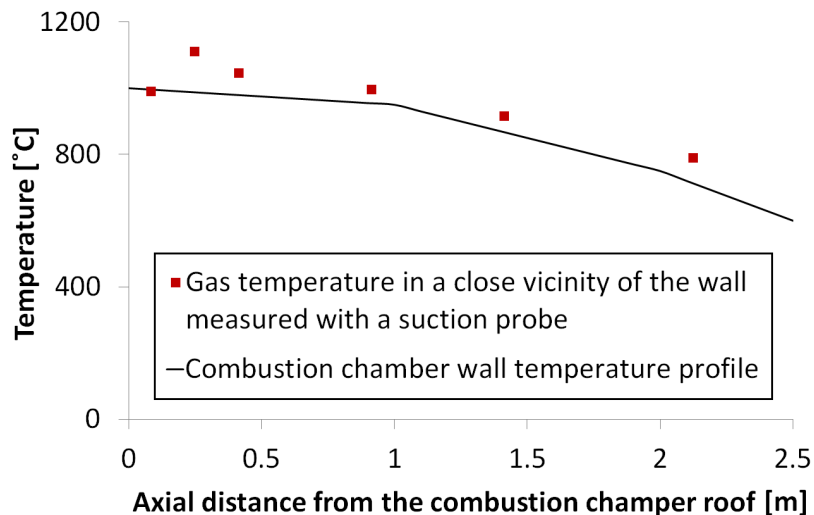
Figure 7.4 *The wall temperature profile used in both simulations. The profile is based on the gas temperature measurements of lignite combustion tests.*

The transport properties of the gaseous species were calculated using temperature dependent polynomial fits available in Fluent database. For CO and CO_2, no polynomial fits were available for thermal conductivity and viscosity, and the kinetic theory was used. The specific heats for all gaseous species were calculated using temperature dependent polynomial fits available in Fluent database. The density of the gas mixture was obtained from the incompressible-ideal-gas equation, and the specific heat capacity with the mixing-law approach.

The calculations were conducted with the Pressure-Based Steady solver of ANSYS Fluent. The pressure and velocity were coupled with the SIMPLE algorithm, and the pressure was discretized with the PRESTO! scheme. The energy, species and DO equations were discretized with the Second Order Upwind scheme. Momentum and turbulence equations were discretized with the First Order Upwind scheme, as the Second Order Upwind scheme had convergence problems probably due to a small number of highly skewed cells close to the swirl wings of the burner. The convergence of the solutions was judged by monitoring the temperature, and mole fractions of oxygen and carbon dioxide at the reactor outlet. The calculations were stopped after the monitored values did not change between the iterations and the residuals had fallen below sufficient limits.

7.2 Results

The results for the lignite combustion simulation are presented in Section 7.2.1, where the simulation data is compared with the measurements. The biomass fuel 1 simulation is then analyzed in Section 7.2.2, including discussion on the reactivity parameter functioning and on the differences between the lignite and biomass simulations.

7.2.1 Lignite Combustion

Temperature Field

Fig. 7.5 presents a temperature contour in a cross section of the 50 kW reactor. The figure shows the locations of the six measurement ports that were used in the lignite combustion measurements in [33]. The measurements were conducted using suction pyrometers with a s-type thermocouple for temperature and a MCS 100E multi-component measuring system for the gas species [33]. The temperature and species concentrations were measured continuously, and the values shown in this section present the time-averaged values obtained from the measurements.

Fig. 7.6 presents the temperature profiles from the center line (0 m) to the combustion chamber wall (0.145 m) at the six axial positions. The calculated profiles match very well with the measurements in all six positions. The largest deviations occur at measurement ports 2 and 3, where the calculations go below the measurements for approximately 35°C and 45°C, respectively. As seen in the figure, the temperature profiles become flat after the first two measurement ports because of the effective mixing caused by the high turbulence.
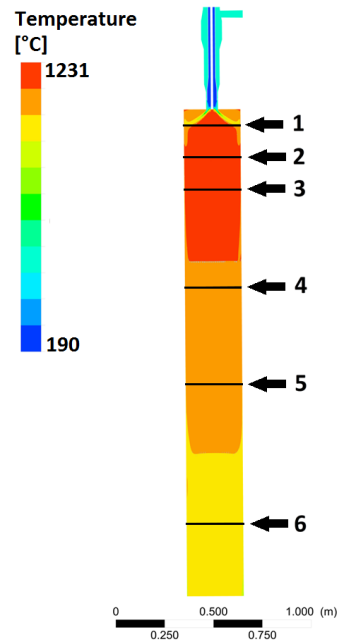
***Figure* 7.5** *Temperature contour of a cross section of the reactor and the locations of the six measurement ports. Distances from the burner: 1) 0.084 m, 2) 0.249 m, 3) 0.414 m, 4) 0.914 m, 5) 1.414 m, 6) 2.124 m.*
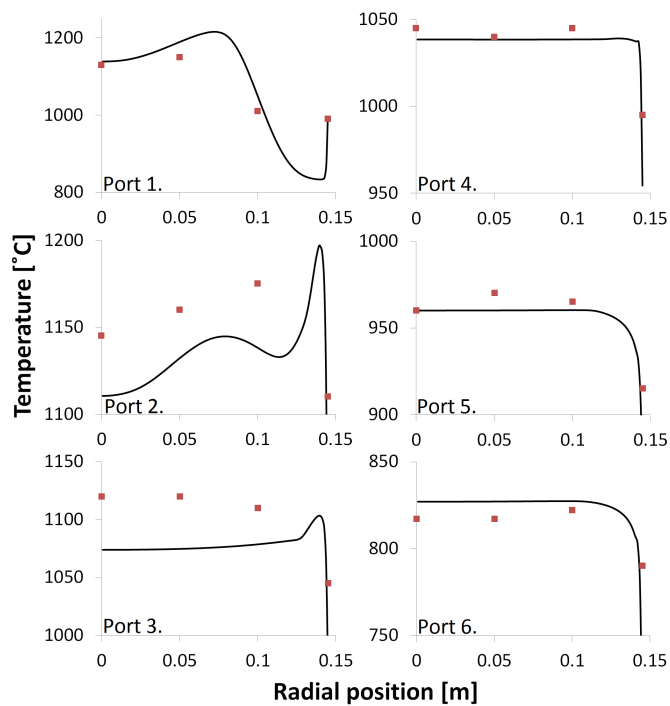
***Figure* 7.6** *Temperature profiles from the center line (0 m) to the combustion chamber wall (0.145 m) at the six axial positions. Measurements from [33].*

Profiles for O$_2$ Volume Fraction

The oxygen profiles and measurements are compared in Fig. 7.7. The values match relatively well, but the oxygen volume fractions in the simulation are slightly higher than the measurements in all locations after Port 1. The largest deviations occurs at Port 2, where the calculations are approximately 3 percentage units above the measurements. This is also the position where the gas temperature showed a slightly too low value. The higher oxygen levels are probably caused by the uncertainties discussed on page 85.

Figure 7.7 *Volume fraction profiles of dry oxygen from the center line (0 m) to the combustion chamber wall (0.145 m) at the six axial positions. Measurements from [33].*

Devolatilization and Char Burnout

Fig. 7.8 presents the contour plots of volatile and oxygen mass fractions, reaction rate for volatile combustion, and char burnout rate. The location of Port 2 is shown in the figure and the red line presents the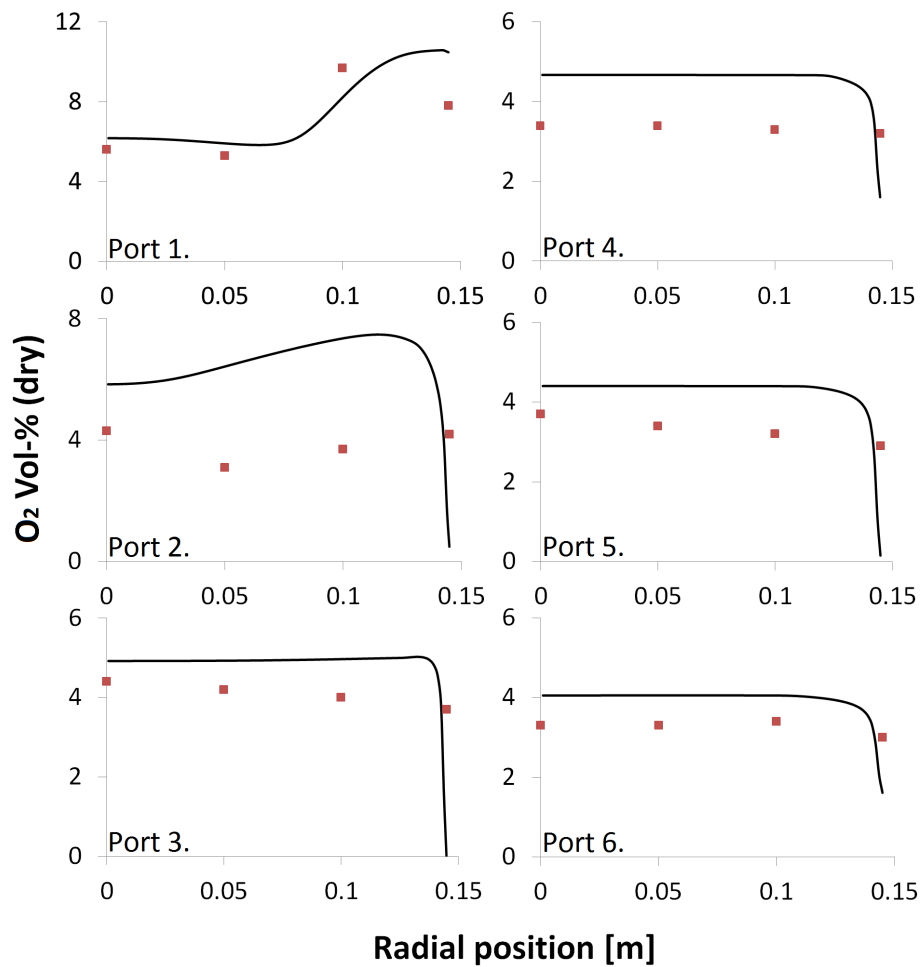 axis where the calculated profiles are compared with the measurements. The flame front of volatile gas combustion can be defined as the thin zone of high reaction rate in the reaction rate contour. The volatile and oxygen mass fractions stay high before the flame front (reactants) and decrease after it (products). Port 2 is located just at the flame front edge, where the oxygen volume fraction is still higher than after the flame front. This indicates that the flame front should locate slightly higher in the reactor, as the oxygen profiles a few centimeters below the measurement port already resemble more of the measured one shown in Fig. 7.7.

The flame front would move upwards in the simulation for example if the volatiles were released earlier. This could be achieved by adjusting the devolatilization reactivity parameters. However, the reason for the high oxygen level at Port 2 could also be that the particles were introduced into the domain with full moisture content, as in reality the particles had already dried for some time at the pipe network before the burner.

A lower oxygen content at Port 2, similar to the measurements, could also be achieved by a higher reaction rate for the char burnout and more evenly distributed particle concentration at the radial direction. The char burnout rate is at the highest level at Port 2 location, as seen in Fig. 7.8, but still not enough oxygen is consumed in comparison to the measurements. The high temperature peak close to the wall in the temperature profile of Port 2 (see Fig. 7.6) is caused by the high char burnout rate.

In reality, the particles probably scatter more effectively in the radial direction and do not concentrate in the close vicinity of the wall as in the simulation. This might be caused by poor wall collision treatment and of neglecting the particle-particle interactions in the CFD model. If the particles were scattered more evenly in the radial direction, the oxygen and temperature profiles would resemble more of the measured ones. However, Fig. 7.8 also indicates that Port 2 is at a very error prone location for experimental measurements. The suction probe can have an effect on the flame and therefore care must be taken when measurements and simulation results are compared at this position.
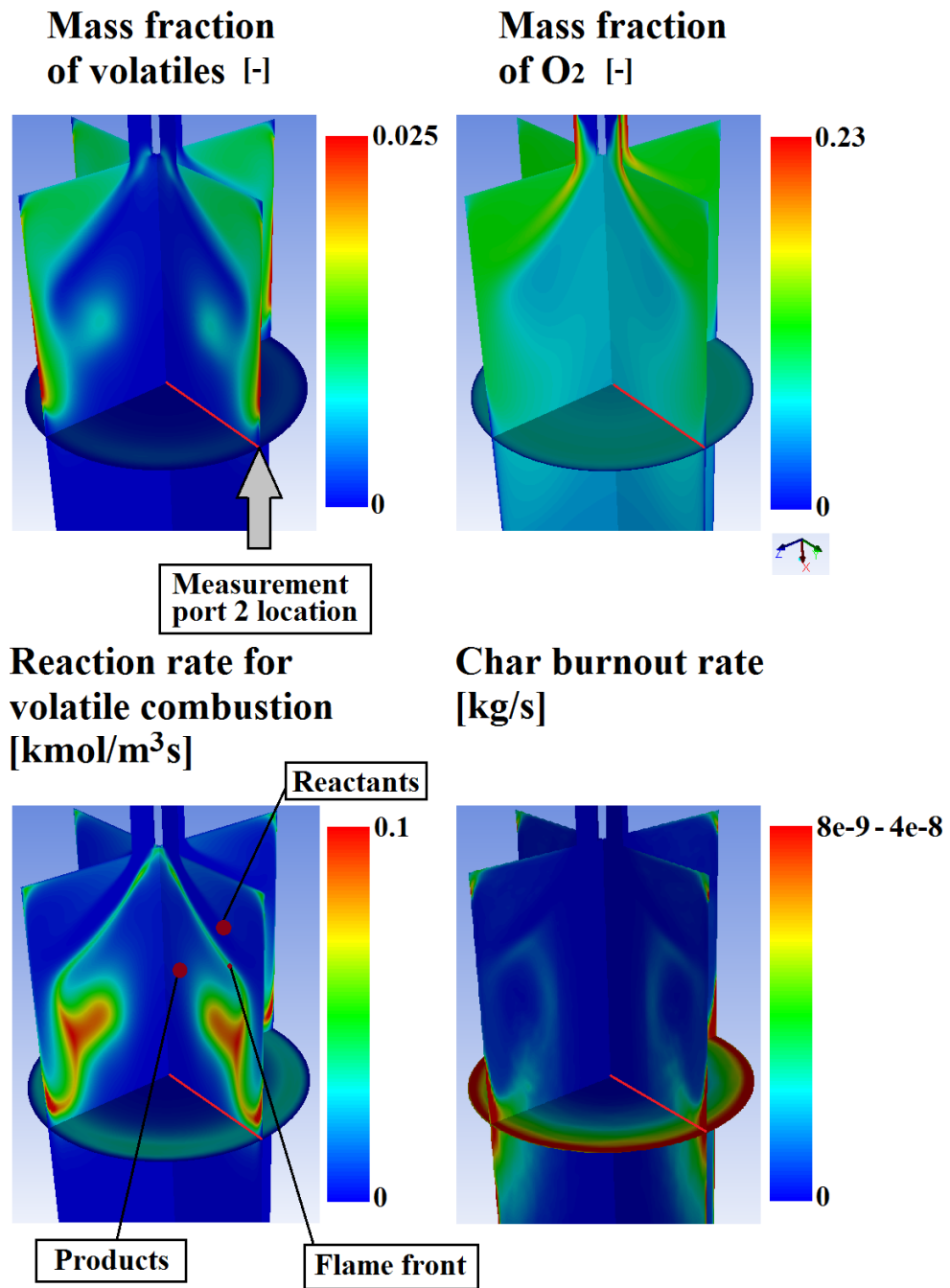
Figure 7.8 *Contour plots of volatile and oxygen mass fractions, reaction rate for volatile combustion and char burnout rate. The location of measurement port 2 is shown in the figure and the red line presents the axis from the combustion chamber wall (0.145 m) to the center line (0 m) where the calculated profiles are compared with the measurements. The scale in the char burnout rate is cut such that the color of the upper limit presents all values between the presented range.*

Profiles for CO_2 Volume Fraction

Fig. 7.9 compares the CO_2 profiles and measurements. The largest deviations can be observed again at the second measurement port. At Port 2, the calculated CO_2 profile goes clearly below the measured values. This is in line with the oxygen profile, as the lower oxygen consumption results in lower CO_2 level at this location. All in all, the calculated profiles follow the measurements relatively well in all measurement ports. Considering the possible measurement errors and inaccuracies in the boundary conditions, the simulation results are in a good agreement with the measurements.

Figure 7.9 *Volume fraction profiles of dry carbon dioxide from the center line (0 m) to the combustion chamber wall (0.145 m) at the six axial positions. Measurements from [33].*

Profiles for H_2O Volume Fraction

Fig. 7.10 presents the volume fraction profiles of H_2O together with the measurements. At Port 4, one measurement point shows a distinct value compared to the other points, which is possibly caused by a measurement error. The calculations the measurements match

relatively well in all measurement ports except at Port 2, where the shape of the calculated profile is clearly different compared to the experimental one. The simulation predicts a flat profile similar to the profiles further away from the burner, while the measurements indicate a profile similar to Port 1.
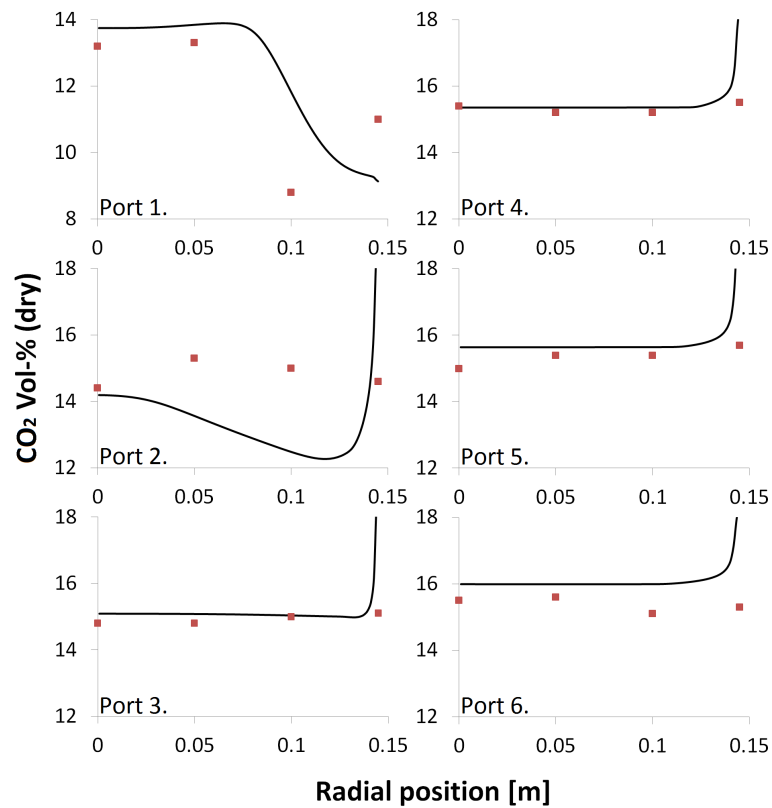

Figure 7.10 *Volume fraction profiles of dry carbon dioxide from the center line (0 m) to the combustion chamber wall (0.145 m) at the six axial positions. Measurements from [33].*

Because the H_2O concentration stays lower close to the wall (reactants) and increases towards the center line (products) at Port 2, this indicates that the flame front would locate further away from the burner than predicted by the simulation (see Fig. 7.8). This, however, is not consistent with the oxygen measurements, which show a relatively flat oxygen profile at Port 2 meaning that the flame front would locate upwards from this position. The reason for the contradiction might be the fact that if the flame front really exists at Port 2 position, the suction probe used in the measurements can affect the flame inside the combustion chamber. Therefore the measurements would show highly fluctuating values for species concentrations, as the probe could be at one instant on the side of the reactant gases (before the flame front) and at another moment on the side of the product gases (after the flame front), depending on the interaction between the probe and

unsteady movement of the flame. This reasoning would explain why the simulation re-
sults consistently deviate from the measurements at Port 2 location, and also indicate that
the flame front position has been relatively well captured in the simulation. To confirm
this deduction, time dependent data on the species concentration measurements should be
observed.

Profiles for CO Concentration

Finally, Fig. 7.11 presents the mass concentration profiles of carbon monoxide together
with the measurements. The calculated profiles and the measurements do not follow the
same trends, but the values are in the same order of magnitude level at most measurement
ports. Considering the highly simplified reaction mechanism in the simulation, the CO
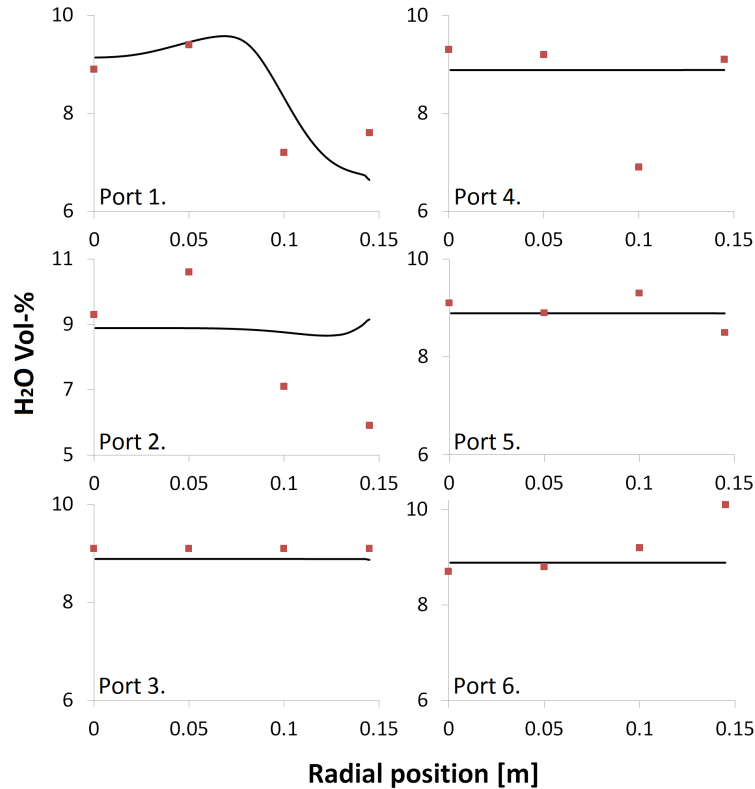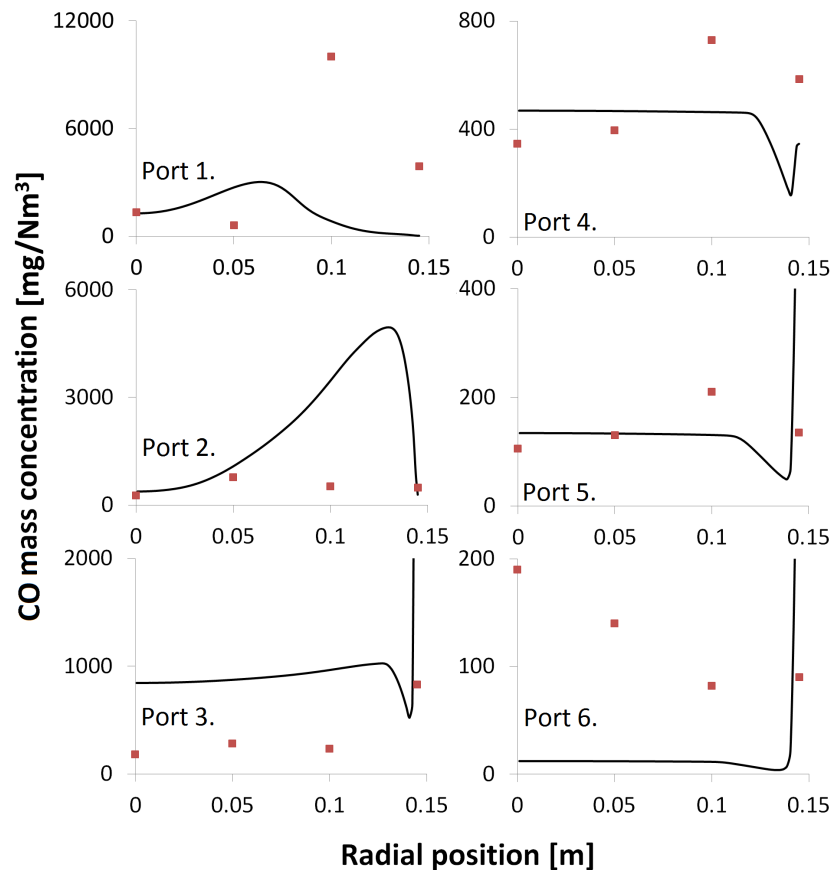profiles are in a reasonable agreement with the measurements.

Figure 7.11 *Volume fraction profiles of dry carbon dioxide from the center line (0 m) to the com-
bustion chamber wall (0.145 m) at the six axial positions. Measurements from [33].*

Summary

As a summary, the model of the 50 kW reactor can predict the temperature field and species concentrations with a relatively good accuracy. The calculated temperatures agreed very well with the measurements as the deviations were smaller than 50°C in all measurement positions. However, the oxygen levels in the simulation were slightly too high compared to the measurements, which could be explained by inaccurate boundary conditions and possibly too low devolatilization or char burnout rates. To calculate all the species concentrations precisely, the boundary conditions should have been set in a detailed accuracy. Furthermore, the particles were introduced into the domain with full moisture content, which can also affect the oxygen levels right after the burner. Neglecting the particle-particle interactions in the high particle concentration areas, and the poor wall collision treatment can also affect the solution accuracy. However, the goal of the lignite simulation was to validate the CFD model of the 50 kW reactor, and therefore it was not meaningful to recalculate the results with revised boundary conditions and modified model settings, as the results were already in a good agreement with the experiments.

The largest deviations in the calculated profiles and measurements were systematically at Port 2, which was partly caused by the error prone position of the port for experimental measurements. The reason might also be in the computational mesh or in the models used in the simulation. To rule out the error produced by the computational mesh, a mesh independence study should be conducted. In addition, another simulation could be conducted using for example a more detailed chemical mechanism and Eddy Dissipation Concept (EDC) for turbulence-chemistry interaction, or different reactivity parameters for devolatilization and char combustion submodels. This way the effect of models and mesh could be analyzed. Due to the scheduling reasons, these procedures have to left in the future. As a conclusion, the model of the 50 kW reactor produces meaningful results and it can be used for further investigations on the functioning of biomass fuel 1 reactivity parameters.

7.2.2   Biomass Fuel 1 Combustion

The simulation for biomass fuel 1 was conducted with the same boundary conditions and models as the lignite simulation. The only difference between the two simulations was the fuel and its properties. Biomass fuel 1 had a remarkably larger particle size, as seen in Fig. 7.2. The devolatilization and char combustion models were the same in both

simulations, but lignite had the default reactivity parameters for coal available in Fluent database, while biomass fuel 1 had the reactivity parameters optimized by Teemu Saarinen [5]. The drag force on the particles was calculated with the spherical drag law for lignite and the non-spherical drag law for biomass fuel 1. The aim of the simulations was to compare how the combustion in the 50 kW reactor changes when the fuel is changed, and to identify how the particle size distribution and reactivity parameters affect the solution. Furthermore, the aim of the biomass fuel 1 simulation was to test how the optimized reactivity parameters work in the turbulent combustion regime.

Temperature Field Comparison

Fig. 7.12 presents the temperature contours in a cross section of the combustion chamber for lignite and biomass fuel 1. The first noticeable difference in the temperature fields is that the biomass fuel 1 maximum temperature is approximately 120°C lower than the maximum temperature for lignite. This seems reasonable, because the smaller particle size of lignite causes more intense flame right after the burner, as the rapid devolatilization occurs. Another notion is that the biomass fuel 1 flame is longer compared to lignite, as the temperature for biomass fuel 1 stays higher further downstream from the burner. This can be also explained by the different particle sizes. The smaller lignite particles burn quickly after entering the combustion chamber and the flue gas has time to cool down during its travel to the combustion chamber outlet. The larger biomass particles, on the other hand, lose their mass in devolatilization and char burnout for a longer distance after entering the chamber, which results in a longer but less intense flame.

The temperature profiles from the combustion chamber wall to the reactor center line at the six measurement port locations (see Fig. 7.5) are presented in Fig. 7.13. The profiles demonstrate how the temperature field changes inside the combustion chamber when the fuel is changed. As seen in the figure, the temperature in biomass fuel 1 combustion stays lower compared to lignite at the three first measurement ports, because the smaller lignite particles burn effectively after entering the combustion chamber. However, the temperature in biomass fuel 1 combustion rises above the lignite temperature at the last three measurement locations, as the larger biomass particles burn longer after the burner.
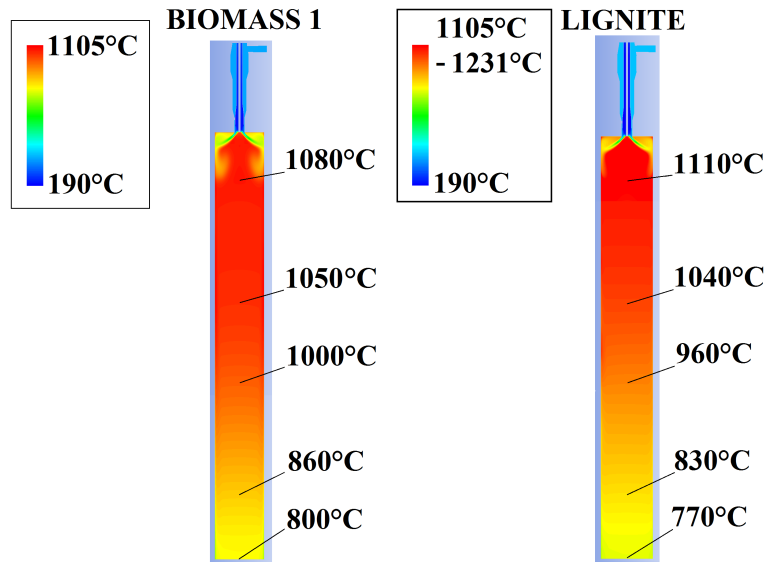
Figure 7.12 *Temperature contours in a cross section of the combustion chamber for biomass fuel 1 (left) and lignite (right). The scale in the contour of lignite is cut such that the color of the upper limit presents all values between the presented range.*
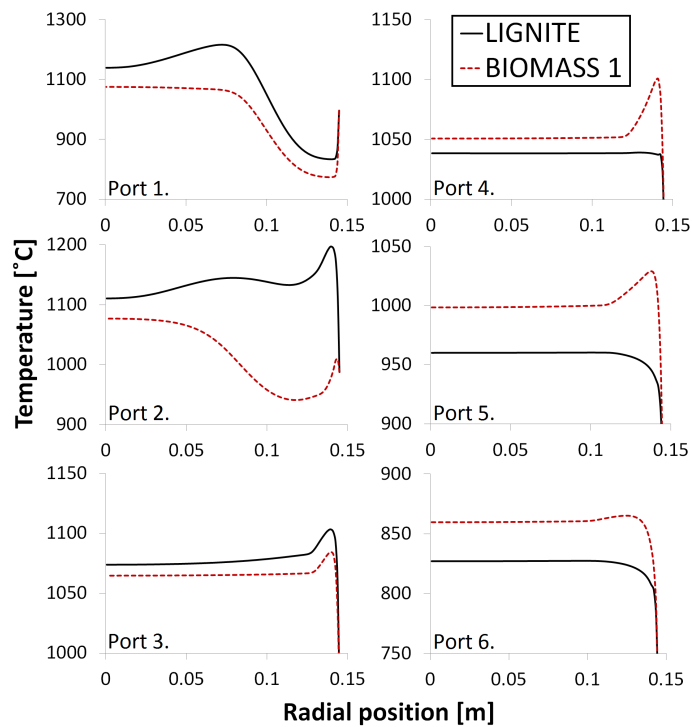
Figure 7.13 *Temperature profiles for lignite and biomass fuel 1 from the combustion chamber wall (0.145 m) to the reactor center line (0 m) at the six measurement port locations. The wall had the same temperature profile as a boundary condition in both simulations.*

Devolatilization and Flame Development

Fig. 7.14 presents the contour plots of temperature, devolatilization rate, and reaction rate for volatile combustion. The biomass particles lose their mass in devolatilization significantly later than the lignite particles. The flame front of the volatile gas combustion, identified by the high reaction rate zone, has a narrower shape compared to lignite, which indicates that in some cases the flame could lift off from the burner in biomass combustion. In case of lignite, the devolatilization occurs rapidly at a relatively localized position, resulting in a high reaction rate zone and intense flame right after the burner. The biomass devolatilization occurs in a wider area which results in a lower maximum reaction rate and causes the different flame shape right after the burner. These properties can affect the ignition and flame stability in biomass fuel 1 combustion.

Figure 7.14 *Contour plots of temperature, devolatilization rate, and reaction rate for volatile combustion. The left column presents results for lignite and the right column for biomass fuel 1. The scale in the contours of lignite is cut such that the color of the upper limit presents all values between the presented range.*
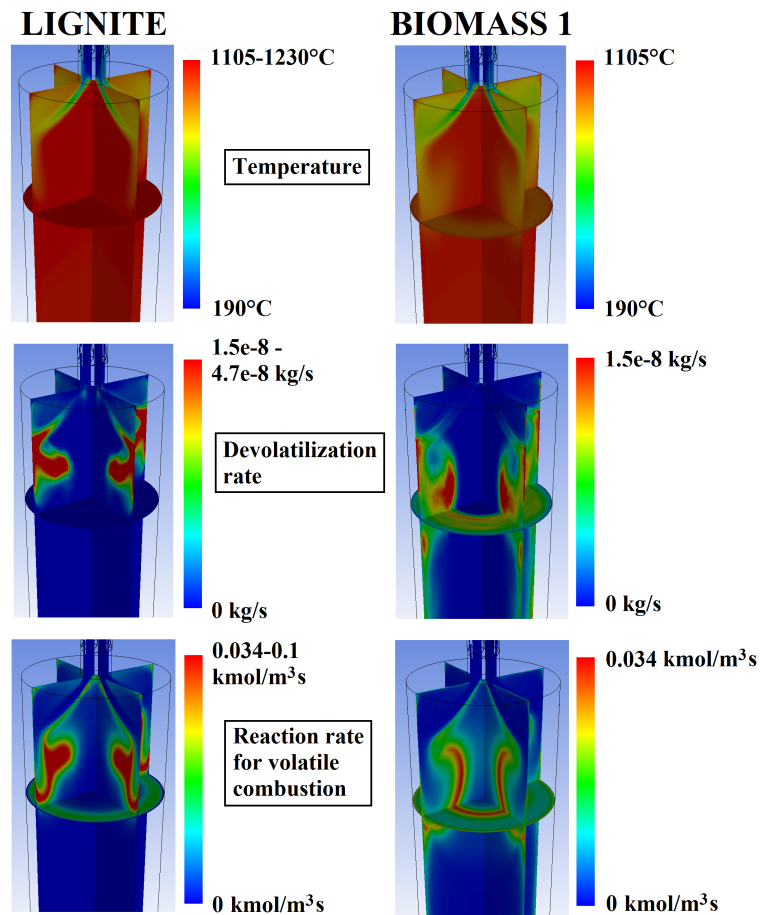
Effect of the Reactivity Parameters

The differences in lignite and biomass fuel 1 simulations have been reasonable this far and the biomass fuel 1 simulation has captured realistic phenomena related to the fuel change. However, the differences have been mostly related to the different particle sizes. In order to analyze the effect of the devolatilization and char burnout reactivity parameters, Fig. 7.15 presents the mass loss curves for three particles of different size in the biomass fuel 1 simulation. The curves have been produced by injecting particles into the converged flow field solution, first with the optimized reactivity parameters and then with the parameters that were used for lignite.
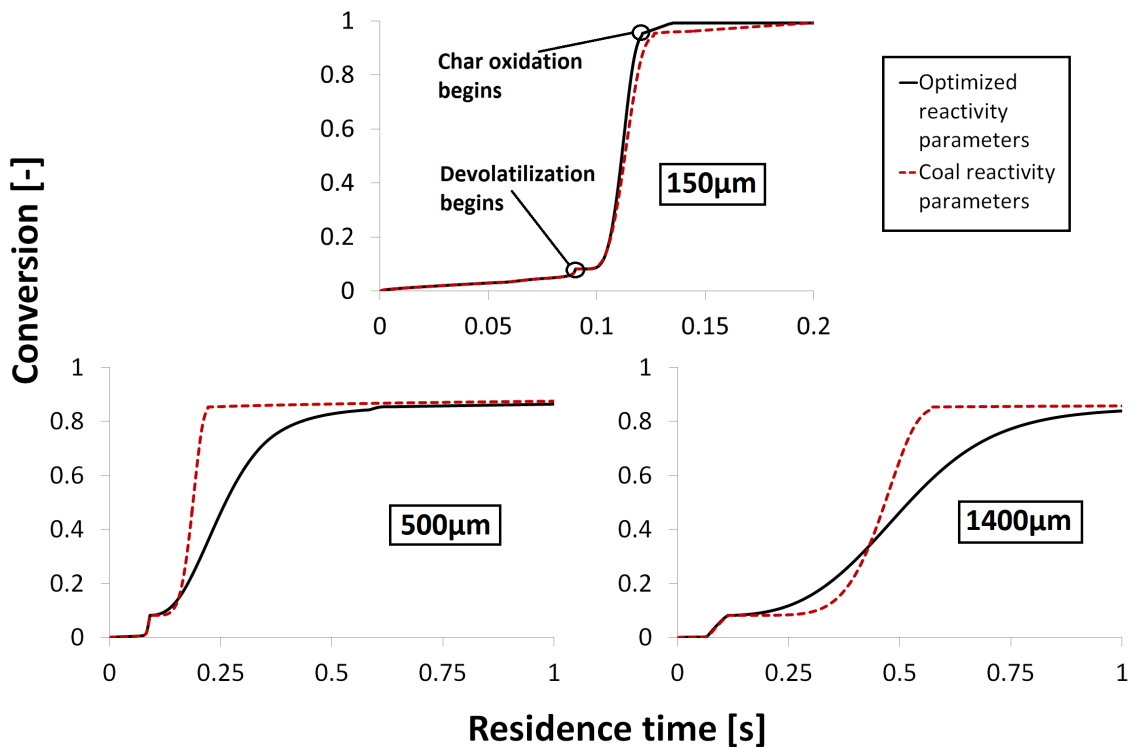
Figure 7.15 Mass loss curves for three particles of different size in the flow field of biomass fuel 1 simulation. The optimized reactivity parameters predict a much slower conversion for the larger particles than the reactivity parameters of coal.

The difference between the smallest particles (150 μm) is rather insignificant in the devolatilization stage. However, the optimized reactivity parameters predict a significantly faster combustion in the char burnout stage. Furthermore, the differences in the conversion curves of the larger particles (500 and 1400 μm) are substantial also in the devolatilization stage, as the reactivity parameters of coal predict a much faster conversion

than the optimized parameters. The particles with the 500 μm diameter have already de-volatilized after 0.23 s with the coal parameters, while the process takes 0.6 s with the optimized parameters. This is a significant difference, because a particle of this size may travel over 0.5 m distance during 0.4 s. This indicates that the biomass fuel 1 simulation would result in a remarkably different solution with the reactivity parameters of coal. The difference between the char burnout reactivity parameters for the larger particles cannot be seen in Fig. 7.15, but the behavior is similar than with the smaller particles. The re-activity parameters of coal predict a significantly slower char burnout compared to the optimized parameters.

Particle Temperature Histories

Fig. 7.16 presents the temperature histories of 500 μm and 1000 μm particles in the 50 kW reactor and in the Drop-Tube Reactor. The devolatilization rate depends strongly on the particle temperature, and the DTR simulations have already shown that the particle mass loss can be relatively well modeled with a similar temperature profile as the particles experience inside the DTR. Fig. 7.16 shows that the particle temperature histories are fairly similar both in the turbulent combustion inside the 50 kW reactor and in the laminar DTR. This indicates that the particle conversion curves in the 50 kW reactor can be rather realistic.
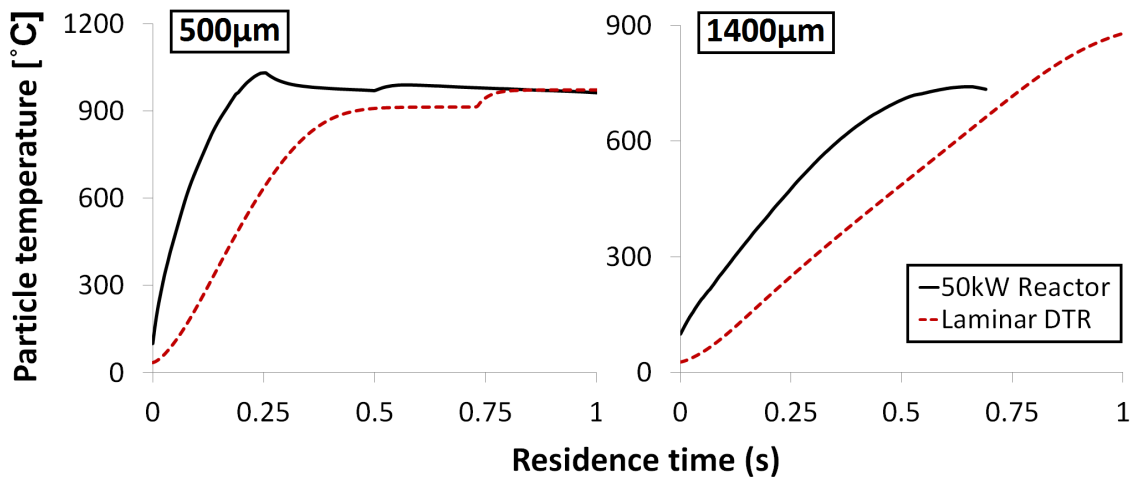

Figure 7.16 *Particle temperature histories in the 50 kW reactor, and in the laminar Drop-Tube Reactor having wall temperature of 900°C. For DTR, the time begins as the particle comes out from the feeding probe. For 50 kW reactor, the time begins when the particle enters the combustion chamber.*

Oxygen Concentration in Particle Surroundings

The DTR experiments indicated that the surrounding oxygen concentration affects the particle mass loss. This could not be taken into consideration using the basic models, because the devolatilization and char burnout could only happen consecutively. Fig. 7.17 presents the oxygen volume fraction surrounding a 500 µm particle during devolatilization. The largest volume fraction the particle experiences is close to 14 vol-%, but the particle spends most of the time below 9 vol-% oxygen. The DTR measurements showed an identical mass loss in pure nitrogen and 3 vol-% oxygen atmospheres during devolatilization. However, the mass loss rate was greater in 21 vol-% oxygen, which indicated simultaneous devolatilization and char burnout. Therefore, the high oxygen concentrations the particles experience in the simulation may in reality increase the particle mass loss rates. This cannot be taken into consideration with the assumption of consecutive combustion stages and the mass loss rates in the simulation may be slightly too low.
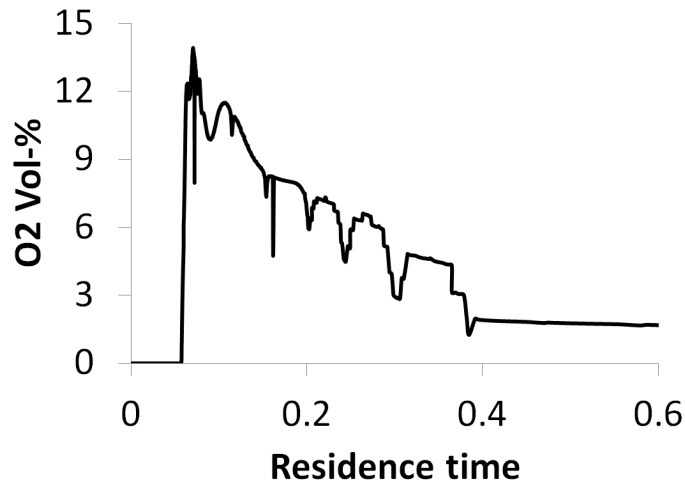
Figure 7.17 *The surrounding oxygen concentration for a 500 µm particle during devolatilization.*

Effect of the Drag Law

The influence of the drag law on the particle trajectories was shortly examined by comparing the movement of biomass fuel 1 particles either with the non-spherical drag law or with the spherical one in the converged flow field solution. When the trajectories of particles having the same size but different drag model were compared, it was noticed that the particles with the non-spherical drag law followed the fluid flow much more effectively

than the particles with the spherical drag law. The effect was emphasized when the particle size increased, such that the residence times of the larger particles were roughly two times longer inside the reactor when the non-spherical drag law was applied. The large differences in the residence times indicate that the drag law has a large effect on the final solution of the combustion simulation. In the future, full simulation results with both drag law models should be compared to better examine the effect of the drag law.

Burnout Efficiency

As a final comparison between the two simulations, the burnout efficiency for both fuels was examined. Here the burnout efficiency is defined as the ratio of combusted dry ash-free matter and the total dry ash-free matter contained in the fuels. In case of lignite, a burnout efficiency of 98.5% was achieved at the outlet boundary of the combustion chamber. In biomass fuel 1 simulation, the efficiency was 93.1%. This result is rather realistic, because the burner is not designed for biomass combustion, and the air divisions and other variables were not adjusted to achieve the best possible burnout. This result indicates that the optimized reactivity parameters work fairly well.

Summary

As a conclusion, the biomass fuel 1 simulation produced meaningful results. The simulation indicated a lower peak temperature and a longer but less intense flame compared to lignite. The biomass particles devolatilized for a longer distance after the burner and ignited later compared to the lignite particles. With the non-spherical drag law, the biomass particles followed the gas movements more effectively compared to the spherical one, and had therefore longer residence times inside the vertically operated reactor. Most differences in the biomass fuel 1 and lignite simulations were explained by the larger size of the biomass particles. The comparison of particle conversion curves with the coal and optimized reactivity parameters indicated that the simulation would change towards a less realistic result if the coal parameters were used. Furthermore, the temperature history comparison for particles inside the DTR and the 50 kW reactor showed that the temperature histories in both simulations were fairly similar, which in turn suggests that the optimized reactivity parameters should work reasonably well in the 50 kW reactor simulation.

The possible error caused by the high oxygen concentrations was examined by plotting a typical oxygen concentration surrounding the particles during devolatilization. The high oxygen levels indicated that there might be an error in the particle conversion curves, because of too low mass loss rate caused by the assumption of consecutive combustion stages. Finally, the comparison of burnout efficiencies showed a lower value for biomass fuel 1, which was a realistic result taking into consideration the combustion set up. All in all, the results suggest that the biomass fuel 1 simulation was successful and the optimized reactivity parameters work in a realistic manner.

It must be noted that experimental combustion tests with biomass fuel 1 should be conducted in order to obtain quantitative data on the functioning of the reactivity parameters and other model variables. Experimental data would be needed to point out the sources of error in the existing devolatilization and char burnout models, and their reactivity parameters. Only after this the most important targets for model development could be identified. The future work should therefore include a comparison between experimental and simulation data, but also sensitivity analysis for the different model parameters. CFD simulations include a large number of submodels and each of them contains assumptions that may cause error in the results. The sensitivity analysis would point out how important the accurate reactivity parameter determination is for different fuels and show a path for the future research in this field.

8.   DISCUSSION AND CONCLUSIONS

In this thesis work, the combustion process of two biomass fuels was modeled with the commercial Computational Fluid Dynamics (CFD) program ANSYS Fluent, using specifically optimized reactivity parameters. The thesis included two CFD modeling cases: a laminar Drop-Tube Reactor (DTR) and a 50 kW pulverized fuel test reactor. The aim of the DTR simulations was to verify the functioning of the apparent reactivity parameters optimized by Teemu Saarinen in his M.Sc. thesis work [5] and to examine how the current modeling approach functions in the CFD environment. After this, the verified parameters were used in biomass combustion modeling in the larger scale 50 kW reactor, to examine how they function in turbulent flow regime combustion.

Reactivity Parameter Optimization and DTR simulations

The reactivity parameters for the two biomass fuels were optimized with the MATLAB R2015a software mainly using information from the experimental studies. In addition to verifying the functioning of the parameters, the laminar DTR simulations of this work were used for analyzing the current modeling approach of using spherical and isothermal particles. The main conclusions that were drawn from the DTR simulations were:

1. For accurate mass loss calculations, the apparent reactivity parameters, the shape and size, the residence times, and the interaction with the environment have to be considered in great detail for the biomass particles.
2. The assumption of consecutive devolatilization and char burnout stages does not hold for the biomass particles in high oxygen concentrations.
3. The Single Kinetic Rate model and the Two Competing Rates (Kobayashi) model produce similar conversion curves during devolatilization and no notable differences could be observed.

Conclusion 1

In general, the idea of the apparent reactivity parameters was to describe the mass loss of the particles in certain external conditions, i.e. at similar high heating rates that prevail in the final application, using the spherical modeling approach. Even though the particle temperature histories were not realistically calculated, the reactivity parameters ensured that the mass loss in these conditions was still correctly calculated. Therefore, it is expected that if the external conditions in the final CFD application are similar to the conditions that were used in the experiments and parameter optimization, the mass loss in the final application can be correctly calculated.

The DTR simulations indicated that it is important that all factors that affect the particle conversion are determined as a combination. The shape and size, the residence times, and the interaction with the environment had to be considered in great detail, if the mass loss was to be accurately modeled. Fig. 8.1 summarizes the current modeling approach and how the different parameters affect the modeling accuracy.
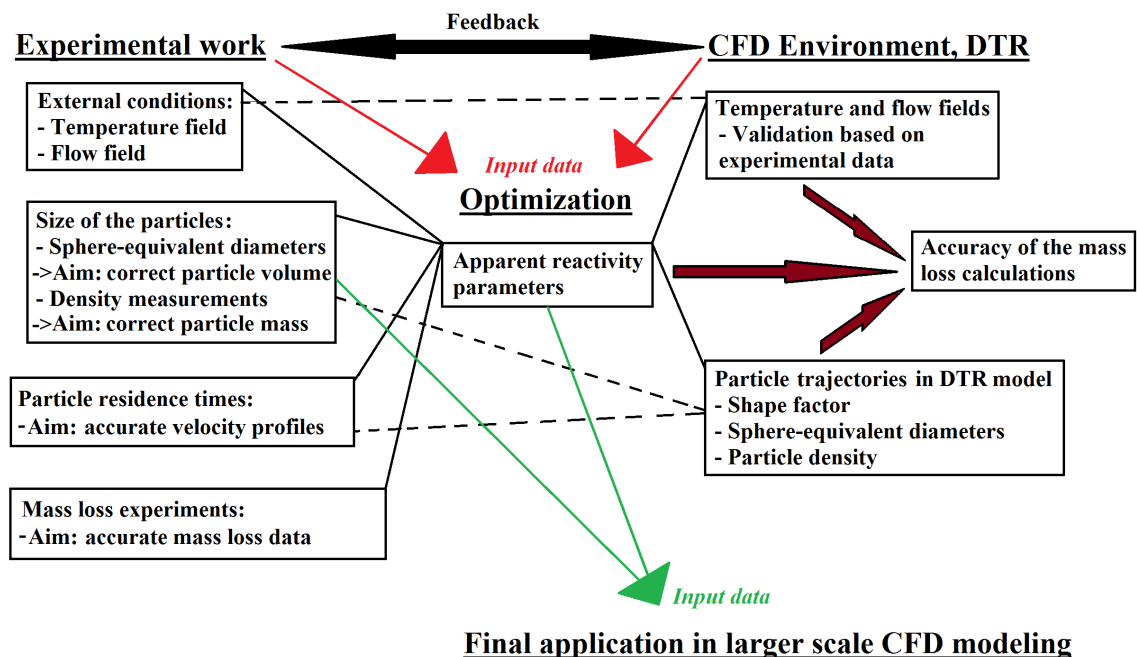
Figure 8.1 *A summary of the current modeling approach and how the different parameters relate to each other. The experimental part in the figure presents the measurements that were conducted for the two biomass fuels. The information from the experiments was used as an input data for the parameter optimization and for obtaining the particle properties in the CFD modeling.*

The DTR simulations demonstrated that CFD modeling can predict the external conditions for the fuel particles with good accuracy. When these conditions were correctly

captured in the model, the accuracy of the mass loss predictions depended mainly on two factors: 1) *the particle trajectories inside the reactor*, and 2) *the reactivity parameters* (see Fig. 8.1).

The accuracy of the particle trajectory calculations, which determined the particle residence times inside the reactor, was mainly affected by 1) *the drag law model*, 2) *the sphere-equivalent diameters* and 3) *the particle densities*. The simulations indicated that the drag law correlation of Haider and Levenspiel [22] can accurately model the particle velocity profiles inside the DTR, when the shape factor in the model was appropriately determined. Other methods, such as the spherical drag law, could not portray the experimental particle velocities.

The value of the shape factor depended on the sphere-equivalent diameters and the chosen particle densities. When the sphere-equivalent diameters, densities and shape factors were determined as a combination for all particle size groups, the velocity profiles and resulting residence times could be accurately modeled. The results for the size group B2a demonstrated the importance of these measurements, as the inaccurate diameters resulted in particle velocity profiles that could not go through the measurements and further resulted in inaccurate mass loss calculations. Therefore, when new fuels are examined, the accurate CFD modeling requires that the three variables (diameters, densities and shape factor) are accurately determined and they function properly as a combination.

The DTR simulations indicated, that the particle residence times used in the reactivity parameter optimization had a strong influence on how well the parameters worked in the CFD environment. In the future, CFD modeling could be therefore more strongly coupled with the parameter optimization procedure to ensure that they function as well as possible. This is related to Fig. 8.1, as the feedback between the experimental and CFD environments was found essential for the reactivity parameters to work accurately in the CFD modeling.

It must be emphasized that the apparent reactivity parameters are always coupled with the parameters that were used in the optimization and it is therefore crucial that the same parameters are also exported to the CFD environment. The feedback between the experimental and CFD work can ensure that the reactivity parameters and particle properties are correctly determined. To summarize the first conclusion, the accurate modeling requires that the same particle properties that were used in the optimization, i.e. the sphere-equivalent diameters, specific heat capacities, densities etc., are used in the final modeling application and the accuracy of these parameters is verified by the feedback between the

two environments. In addition, the DTR simulations indicated that the particle trajectories play an important role in the mass loss calculations and therefore the functioning of the shape factor has to be appropriately evaluated.

Conclusion 2

The experimental data indicated that the mass loss of all particle size groups was identical in pure nitrogen and in 3 vol-% of oxygen atmospheres. This means that the devolatilization, which only depends on the particle temperature history, could be modeled as a separate stage in the particle conversion curves. Therefore, the assumption of consecutive combustion stages worked for the biomass fuels in low oxygen levels. However, in 21 vol-% of oxygen the conversion of all particle size groups became faster in comparison to the 3 vol-% of oxygen level. This could not be modeled with the assumption of consecutive combustion stages, because the oxygen concentration only affects when the char burnout model is activated. The experimental conversion behavior in high oxygen levels could be better captured if the devolatilization and char burnout stages were allowed to happen simultaneously.

Conclusion 3

There were no notable differences between the Single Kinetic Rate and the Kobayashi devolatilization models after the reactivity parameters were optimized. Both models produced very similar conversion curves in the DTR simulations and both models will likely produce similar results also in larger scale modeling. The full potential of the Kobayashi model could be better exploited if the final volatile yield of the fuel particles was a variable instead of a predetermined constant. However, considering combustion simulations the constant volatile yield is probably not a significant drawback, as the particles will always experience rather high heating rates which result in approximately constant volatile yield for all particles. Furthermore, it is still possible to give different volatile yields for the different particle sizes and this is probably sufficient for combustion simulations.

Larger Scale CFD Modeling

The results of the 50 kW reactor indicated that biomass combustion can be successfully modeled with the spherical and isothermal assumptions if the apparent reactivity parameters are accurately determined. However, quantitative validation is still required.

In general, the results of the 50 kW reactor were realistic and captured multiple phenomena that would be expected if biomass was combusted in the reactor, such as the lower burnout efficiency compared to lignite. This indicates that the apparent reactivity parameters can describe the biomass mass loss in pulverized biomass combustion, even with the sphere-equivalent diameters and isothermal particles. The external conditions in the 50 kW reactor were rather similar to the laminar DTR, as the particles experienced similar high heating rates after entering the combustion chamber in the 50 kW reactor or the heated reactor part in the DTR. This is an essential part of the current modeling approach, as it is expected that the apparent reactivity parameters only work in similar external conditions that were used in the experiments and further in optimization.

The 50 kW reactor simulation indicated that the same factors that in the DTR, i.e. the accuracy of the external conditions, particle trajectories and reactivity parameters, determine the outcome of the final results. It is expected that these factors determine together in which position and how much gaseous species are released from the particles and how the flame in the CFD model further develops.

In larger scale applications, the external conditions for the fuel particles are mainly determined by interaction of the particle modeling and the other submodels of the simulation. These submodels include the models for turbulence, radiation and turbulence-chemistry interaction. Naturally, the most suitable models for the problem in question have to be chosen in order to obtain accurate combustion results.

The particle trajectories and the reactivity parameters were the main parameters analyzed in this work. The non-spherical drag law produced different particle trajectories for the biomass particles, than were observed with the spherical drag law in the converged flow field solution. The residence times of the larger particles inside the reactor were roughly two times longer with the non-spherical drag law than with the spherical one. This indicates that the drag law has a large effect on the particle conversion history and final solution, also in turbulent flows similarly with the DTR simulations. The 50 kW simulation indicated that the non-spherical drag law is better suitable for biomass particles, which is reasonable when the irregular particle shapes are considered. According to the results, it is recommended that the non-spherical drag law is used in biomass modeling. However, in the future the functioning of the non-spherical drag law correlation has to be thoroughly examined for turbulent flow regime.

The simulation results showed that the reactivity parameters worked relatively well also in the 50 kW simulation. When the particle conversion curves were compared with the ones

produced by the coal parameters, the optimized parameters gave a remarkably slower mass loss rate for the larger biomass particles. The optimized parameters expectedly produce more realistic results, as was concluded from the realistic burnout efficiency. This indicates that the reactivity parameters are important to accurately predict the biomass combustion process.

As the DTR conclusions stated, the reactivity parameters are coupled with the particle properties that were used in the reactivity parameter optimization. The comparison with the lignite simulation indicated that the size of particles had a large effect on the final solution. Therefore, it is expected that an accurate sphere-equivalent particle size distribution is required, together with the optimized reactivity parameters, to capture the flame characteristics and especially the amount of unburned fuel in the CFD models. A sensitivity analysis should be conducted to point out the factors that have the greatest effect on the final simulation results.

These results indicate, that if the sphere-equivalent diameters, the drag law model and the reactivity parameters are jointly determined, then the turbulent combustion process can be modeled with the spherical and isothermal assumptions. This means that the parameters from the current modeling approach could be used in design and optimization purposes, for example in minimizing the amount of unburned fuel in real scale boilers. The most important part in the future work would be to validate the modeling approach by comparing experimental and CFD results in a larger scale application.

9. FUTURE WORK

The following list summarizes the main aspects of the future work that were identified during this thesis.

1. Improving the procedure for determining the apparent reactivity parameters.
2. Improving the coupling between the devolatilization and char burnout models.
3. Validating the larger scale results with experimental measurements.
4. Studying the functioning of the non-spherical drag law in turbulent flow regime.
5. Conducting a sensitivity analysis for the reactivity parameters and other model variables.

The first goal in the future research includes improving the current modeling approach. Many targets for future development were found during the research, the most important ones being the more accurate particle velocity measurements, a higher DTR to better study the larger biomass particles and the char combustion stage, and improving the accuracy of the sphere-equivalent diameters and densities to produce mass-equivalent particles.

The second goal of the future work is to modify the coupling between the devolatilization and char burnout models. If the two models were allowed to occur simultaneously, the effect of increasing mass loss rate in high oxygen levels could be included in the modeling. This way the mass loss of the biomass particles could be better predicted when the particle trajectories go through high oxygen level locations.

The most important goal for the future development includes model validation through comparison between simulation results and experiments. This would ensure that the current modeling approach works in real biomass combustion applications and the parameters could be used in the industry with better confidence on the results. Furthermore, the comparison would help in identifying the main drawbacks of the modeling approach and to better find the targets for future development.

In the current work, the functioning of the non-spherical drag law was verified only for the laminar flow regime in the DTR simulations. However, in the future work the drag law functioning in the turbulent flow regime should be ensured, because it has a strong influence on the particle trajectory calculations and the final solution in larger scale CFD modeling. The particle residence times inside the 50 kW reactor and the DTR were remarkably different depending on the chosen drag law model and therefore its role should be further examined.

Finally, a sensitivity analysis for the reactivity parameters should be conducted in relation to the final simulation results. The CFD simulations always include many submodels in addition to the particle modeling, such as the turbulence model, the radiation model and the turbulence-chemistry interaction model. The sensitivity analysis would point out the importance of accurate reactivity parameters. If the final simulation results would not significantly change if the reactivity parameters were changed for example by $\pm 20\%$, then the detailed reactivity parameters were of no use. In addition, the sensitivity analysis should be conducted for different parameters in the modeling chain, such as for the sphere-equivalent particle size distribution or particle density measurements, in order to see which parameters have the greatest effect on the final simulation results. This would provide further information on which parameters are the most important to be accurately measured for CFD modeling applications.

REFERENCES

[1] P. Basu, *Biomass Gasification, Pyrolysis and Torrefaction*, Elsevier Inc., 2nd ed., San Diego, USA, 2013, 530 p.

[2] European Environment Agency, *How much bioenergy can Europe produce without harming the environment?*, EEA Report, No. 7, 2006

[3] D.P. Vuuren, E. Stehfest, M.G.J. Elzen, T. Kram, J. Vliet, S. Deetman, M. Isaac, K. Klein Goldewijk, A. Hof, A. Mendoza Beltran, R. Oostenrijk, B. Ruijven, *RCP2.6: Exploring the Possibility to Keep Global Mean Temperature Increase Below 2°C*, Climatic Change, Vol. 109, No. 1, 2011, pp. 95–116.

[4] The MathWorks Inc., *MATLAB Release 2015a*, Natick, Massachusetts, United States, http://se.mathworks.com/.

[5] T. Saarinen, *Determining Reactivity Parameters for Two Biomass Fuels*, Master of Science Thesis, Tampere University of Technology, In Press, 2016.

[6] ANSYS Inc., *Fluent 15.0 Theory Guide (2013)*, Cecil Township, Pennsylvania, United States, http://fluent.com/.

[7] European Parliament and Council of the European Union, *Directive 2009/28/EC of the European Parliament and of the Council*, Official Journal of the European Union L140/16, 2009, 47 p.

[8] ISO 17225 Standard Series, *Solid Biofuels – Fuel Specifications and Classes*, The International Organization for Standardization, 2014.

[9] S. Döring, *Power from Pellets: Technology and Applications*, Springer-Verlag, 1st ed., Berlin, Heidelberg, Germany, 2013, 223 p.

[10] H. Schobert, *Chemistry of Fossil Fuels and Biofuels*, Cambridge University Press, 1st ed., New York, USA, 2013, 480 p.

[11] J.M. Jones, M. Nawaz, L.I. Darvell, A.B. Ross, M. Pourkashanian, A. Williams, *Towards Biomass Classification for Energy Applications*, In: Bridgwater, A.V., Boocock, D.G.B. (Eds.), Science in Thermal and Chemical Biomass Conversion, CPL Press, 2006, pp. 331–339.

[12] P. Grammelis, *Solid Biofuels for Energy: A Lower Greenhouse Gas Alternative*, Springer-Verlag, 1st ed., London, UK, 2011, 242 p.

[13] R. Zanzi, K. Sjöström, E. Björnbom, *Rapid High temperature Pyrolysis of Biomass in a Free-Fall Reactor*, Fuel, Vol. 75, No. 5, 1996, pp. 545–550.

[14] T. Nussbaumer, *Combustion and Co-combustion of Biomass: Fundamentals, Technologies, and Primary Measures for Emission Reduction*, Energy & Fuels, Vol. 17, No. 6, 2003, pp. 1510–1521.

[15] Y. Yang, V.N. Sharifi, J. Swithenbank, L. Ma, L.I. Darvell, J.M. Jones, M. Pourkashanian, A. Williams, *Combustion of a Single Particle of Biomass*, Energy & Fuels, Vol. 22, No. 1, 2008, pp. 306–316.

[16] R. Mehrabian, S. Zahirovic, R. Scharler, I. Obernberger, S. Kleditzsch, S. Wirtz, V. Scherer, H. Lu, L. Baxter, *A CFD Model for Thermal Conversion of Thermally Thick Biomass Particles*, Fuel Processing Technology, Vol. 95, 2012, pp. 96–108.

[17] H. Lu, E. Ip, J. Scott, P. Foster, M. Vickers, L. Baxter, *Effects of Particle Shape and Size on Devolatilization of Biomass Particle*, Fuel, Vol. 89, No. 5, 2010, pp. 1156–1168.

[18] United Nations Environment Program, *Technical Study Report: Biomass Fired Fluidized Bed Combustion Boiler Technology for Cogeneration*, Available: unep.org/climatechange/mitigation/Portals/93/documents/EnergyEfficiency/FBC_30_sep_2007.pdf (March 21, 2016).

[19] T. Poinsot, D. Veynante, *Theoretical and Numerical Combustion*, R.T. Edwards Inc., 2nd ed., Philadelphia, USA, 2005, 522 p.

[20] H.K. Versteeg, W. Malalasekera, *An Introduction to Computational Fluid Dynamics: The Finite-Volume Method*, Pearson Education Ltd, 2nd ed., Edinburgh Gate, Harlow, England, 2007, 503 p.

[21] C. Cortes, A. Gil, *Modeling the Gas and and Particle Flow Inside Cyclone Separators*, Progress in Energy and Combustion Science, Vol. 33, No. 5, 2007, pp.409–452

[22] A. Haider, O. Levenspiel, *Drag Coefficient and Terminal Velocity of Spherical and Nonspherical Particles*, Powder Technology,Vol. 58, No. 1, 1989, pp. 63–70.

[23] W. E. Ranz, W. R. Marshall Jr., *Vaporation from Drops, Part I*, Chem. Eng. Prog., Vol. 48, No. 3, 1952, pp. 141–146.

[24] W. E. Ranz, W. R. Marshall Jr., *Vaporation from Drops, Part I and Part II*, Chem. Eng. Prog., Vol. 48, No. 4, 1952, pp. 173–180.

[25] R.P. Chhabra, L. Agarwal, N.K. Sinha, *Drag on Non-spherical Particles: An Evaluation of Available Methods*, Powder Technology, Vol. 101, No. 3, 1999, pp. 288–295.

[26] M.M. Baum, P.J. Street, *Predicting the Combustion Behavior of Coal Particles*, Combustion Science and Technology, Vol. 3, No. 5., 1971, pp. 231–243.

[27] M.A. Field, *Rate of Combustion of Size-Graded Fractions of Char from a Low Rank Coal between 1200 K–2000 K*, Combustion and Flame, Vol. 13, 1969, pp. 237–252.

[28] H. Tolvanen, L. Kokko, R. Raiko, *Fast Pyrolysis of Coal, Peat, and Torrefied Wood: Mass Loss Study with a Drop-Tube Reactor, Particle Geometry Analysis, and Kinetics Modeling*, Fuel, Vol. 111, 2013, pp. 148–156.

[29] H. Tolvanen, R. Raiko, *An Experimental Study and Numerical Modeling of Combusting Two Coal Chars in a Drop-Tube Reactor: A Comparison Between N2/O2, CO2/O2 and N2/CO2/O2 Atmospheres*, Fuel, Vol. 124, 2014, pp. 190–201.

[30] H. Tolvanen, T. Keipi, R. Raiko, *A Study on Raw, Torrefied, and Steam-Exploded Wood: Fine Grinding, Drop-Tube Reactor Combustion Tests in N2/O2 and CO2/O2 Atmospheres, Particle Geometry Analysis, and Numerical Kinetics Modeling*, Fuel, In Press, Uncorrected Proof, 2016.

[31] H. Tolvanen, *Advanced Solid Fuel Characterization for Reactivity and Physical Property Comparison*, Dissertation, Tampere University of Technology, Puplication 1359, 66 p., Available: http://URN.fi/URN:ISBN:978-952-15-3674-8

[32] A.F. Mills, *Basic Heat and Mass Transfer*, Prentice-Hall Inc., 2nd ed., New Jersey, USA, 1999, 1000 p.

[33] R. Wilhelm, *Bildung und Reduktion von Stickoxiden bei Braunkohlefeuerungen im Luft- und Oxyfuel-Betrieb*, Dissertation, Technical University of Dresden, 2010.